Development of Materials for Extreme Environment Applications by Laser Powder Bed Fusion

By

Alexander D. O'Brien

B.S. Chemical Engineering and B.S. Physics
University of Arkansas, 2019

Submitted to the Department of Nuclear Science and Engineering
in partial fulfillment of the requirements for the degree of

DOCTOR OF PHILOSOPHY IN
NUCLEAR SCIENCE AND ENGINEERING

at the

MASSACHUSETTS INSTITUTE OF TECHNOLOGY

June 2023

Authored By:	Alexander D. O'Brien Department of Nuclear Science and Engineering May 15, 2023
Certified by:	Ju Li Battelle Energy Alliance Professor of Nuclear Science and Engineering, Thesis Supervisor
Accepted by:	Ju Li Department of Nuclear Science and Engineering Chair, Department Committee on Graduate Students

Development of Materials for Extreme Environment Applications by Laser Powder Bed Fusion

by

Alexander D. O'Brien

Submitted to the Department of Nuclear Science and Engineering
on May 15, 2023, in partial fulfillment of the requirements for the degree of
Doctor of Philosophy in Nuclear Science and Engineering

Abstract

As the desire for greener, more efficient energy production creates an urgent push for advances in reactor and turbine designs, rapid innovation must be achieved in the field of extreme environment materials. Recent technological progress in metal additive manufacturing has enabled new techniques in materials design that might prove essential in closing current gaps. In this study, I identify two critical advanced energy systems that may be improved with materials produced by metal additive technology, fusion reactor vacuum vessels and jet engine turbine blades, and explore the practical usage of laser powder bed fusion to improve production of relevant materials.

First, material enhancements are considered in the context of increasing survivability for full-power operation of the ARC tokamak fusion reactor. Based on evaluation of relevant properties for four candidate vacuum vessel materials, Inconel 718 is identified as the most likely selection for construction of an initial ARC pilot plant in the short-term. Maximizing the lifetime of such a vessel will require tailoring properties to increase resistance to neutron effects and, especially, to enhance mechanical properties in the range of 800°C. Both targets are expected to be addressable by the formation of a 718-based metal matrix composite, which is enabled by additive manufacturing. Based on rapid evaluation of various ceramics in Al-based composites, SiC is selected as a promising candidate, so an Inconel 718 composite reinforced with 2 vol% SiC is produced by laser powder bed fusion. Microstructural analysis reveals breakdown of SiC and in-situ formation of silicides and carbides, which result in decreased porosity and grain size. Room temperature mechanical tests show good strengthening over base Inconel 718 with low loss in ductility. Improvement in high temperature ductility is achieved over the unreinforced material, but the effects appear inadequate to merit use over a wrought Inconel. An additional composite is then developed using 2 vol% ZrB_2 as the reinforcing material. Microstructural results for this composite follow a similar trend to SiC and verify the capability for reducing porosity. Room temperature mechanical testing shows higher strength and lower ductility than the SiC. However, elongation at failure is found to increase drastically around 800°C, reaching more than 8x that of printed unreinforced Inconel. These results suggest high potential for ARC implementation.

Second, the use of functionally graded printing is discussed as a potential method of establishing improved oxidation resistance for the use of niobium for turbine blade

applications. To enable future studies of this, a process flow is developed to establish niobium printability. The viability of high-throughput single-layer testing with fixed-depth wells is first assessed for rapid, material-efficient parameterization. Promising conditions are then transferred to multi-layer printing, and further iteration is conducted to minimize surface agglomeration and allow continuous build-up. Finally, a Gaussian regression code is applied to recommend optimum conditions. The resulting print quality is found to achieve the first scalable printing of niobium powder in a commercial powder bed fusion system, which is necessary to enable the exploration of techniques such as functional grading.

Thesis Supervisor: Ju Li

Title: Battelle Energy Alliance Professor of Nuclear Science and Engineering

Acknowledgments

I would like to thank Prof. Mike Short for serving on my thesis committee and Prof. Zach Hartwig for serving as the chair of my defense committee. Throughout my PhD program, Prof. Short has been an invaluable help in guiding my exploration and probing me to better understand the role of materials, and collaboration with his group members has been a great boon to supporting my progress. Prof. Hartwig has been a source of encouragement since even before my time at MIT began, and I am extremely grateful for his willingness to lend his own lab's time and resources towards my efforts as well.

I am also incredibly thankful to the Nuclear Science and Engineering Department as a whole for taking a chance on accepting a young chemical engineering convert from Arkansas in a year of record low acceptance. I have loved the unique environment for learning that MIT creates, and the NSE department provides a particularly special community of collaboration and excitement that has been a joy to be a part of.

I gratefully acknowledge the National Science Foundation for their support of my research through the Graduate Research Fellowship Program, which has offered me the freedom to explore new and exciting fields based on my own interest. I would also like to acknowledge the ARPA-E program and Eni S.p.A. for funding the specific projects to which I have dedicated the majority of my efforts.

Thank you to Dr. Kang Pyo So, my friend and mentor who initiated the work on metal matrix composites and trained me to take up the torch once he left MIT. Thank you to Dr. Emre Tekoğlu, who worked alongside me as an irreplaceable partner over the last two years. Thank you to the many collaborators who helped to develop this work to a level of success, including Prof. Wen Chen, Jian Liu, and the team at the ADDFab at UMass Amherst, as well as the team under Prof. Gi-Dong Sim at the Korea Advanced Institute of Science and Technology.

I of course must thank my advisors, without whom none of my achievements would be possible. Thank you to Prof. John Hart, who stepped in as a co-advisor and mentor and welcomed me into his group to guide me in learning about the world of 3D printing. And a major thank you to my primary advisor, Prof. Ju Li, whose wisdom, guidance, and friendship over the last four years have allowed me to grow as a researcher and a person.

I also must thank my good friends and wonderful family. Payton, Kyle, and Harrison refused to lose touch despite the distance between us and were a consistent source of encouragement and fun. My parents, Dave and Nancy, and my brother, Ben, supported and celebrated with me every step of the way, and I thank them for building my sense of confidence and intrigue and reinforcing my character throughout my life. Above all, thank you to my wonderful wife and best friend, Kaitlyn, who has stood beside me on every step of this journey.

Lastly, I give thanks to God for the many blessings in my life which have brought me to this point and which will continue to manifest in the future.

Table of Contents

List of Figures

List of Tables

Chapter 1

Introduction

1.1 Motivation

Throughout the last several decades, advancements in materials science could be stated to have undergone a shift of scale. The development of high-performance computing brought with it both enhanced atomistic-to-macroscale thermodynamic modeling and machine-learning-based decision making, which have promoted the rapid exploration of phase changes achievable with miniscule compositional shifts in systems too complex for experimental trial and error. Meanwhile, improvements in nano-fabrication have enabled the development of advanced metamaterials, featuring properties fundamentally different from those observed when prepared in bulk. Research activities in these areas have made astonishing leaps and bounds in progressing our understanding of the full capabilities of materials engineering. However, this recent focus on the power of the small has been predictably contained to the production of small components. In the rare cases that nano-scale material engineering is accomplished at scales large enough for structural, and specifically load-bearing, applications, it is typically done at great cost and effort that places severe limits on utilization.

With recent advancements in additive manufacturing technology, the materials landscape appears to be undergoing a paradigm shift. For the first time for many material

designs, additive manufacturing techniques introduce a level of precision and compartmentalization to the fabrication process that allows for the implementation of nanostructures and micron-scale design changes in a manner that is fully scalable. Suddenly, complex materials that have been restricted to powder sintering of cm-scale discs for years can be constructed, not only at any size scale, but also at near-net shape with almost any level of geometrical complexity desired.

While additive manufacturing processes have in no way been perfected, the technology has reached a point where its implications towards structural applications can and should be examined. This becomes especially apparent when one considers the pressing need for rapid improvements in the energy industry, where advancements in efficiency are frequently restricted by operational limits that might be feasibly increased if the types of nano-enhanced materials being developed at small-scale can be practically applied.

In this thesis, my primary focus will be on exploring the capabilities of current additive manufacturing technology towards fabricating materials more suitable for applications in extreme environments, with the overall motivation of supporting the development of more efficient energy production for a cleaner future.

1.2 Problem Statement

The work and discussion presented here will be an investigation of novel materials systems that are either 1) previously unexplored and enabled by additive manufacturing technology or 2) not well investigated for additive manufacturing but predicted to see practical improvements in applicability if the technology can be implemented. The work conducted is primarily experimental, involving real application of laser powder bed fusion to demonstrate the current state of the materials and assess both their feasibility for immediate implementation and the key areas which should be the focus of future studies to further their development.

The remainder of this section will detail the organization of this thesis, with a focus on the problem addressed and work performed in each chapter. Chapters 2-6 will consider materials primarily through the lens of an exemplar extreme environment for the field of nuclear energy, the under-development ARC tokamak, while Chapter 7 will then take a

step back and consider work on a non-nuclear-focused material to provide a broader viewpoint. In Chapter 2, I will start with a discussion of the present state of materials and their compatibility for the current design specifications of ARC. Nickel superalloys, ferritic/martensitic steels, vanadium alloys, and SiC ceramic composites will be reviewed and evaluated on the basis of their mechanical properties, high-temperature capabilities, corrosion and radiation resistance, and practical capability for implementation. I will then seek to identify the materials most likely to be implemented in the near term and to recommend the key shortcomings that should be the primary focus of improvement in upcoming research. In Chapter 3, I will introduce the concept of metal matrix composites. I will describe how the benefits of this class of materials might address the key issues identified for the ARC vacuum vessel, and I will explain how additive manufacturing has enhanced the feasibility of this technology and expanded the potential metal-ceramic combinations to be explored. Chapter 4 will focus on the beginning of my experimental work to identify the compatibility of various ceramics with a model FCC system, AlSi10Mg. I will detail the workflow utilized for rapid production and evaluation, as well as the criteria used to identify potentially high merit reinforcing ceramics. Chapters 5 and 6 will focus on my production of new Ni-based MMC materials, In718+SiC and In718+ZrB_2, respectively. I will detail fabrication methods and confirm compatibility of these material systems for laser powder bed fusion. I will then describe the microstructural analysis conducted and examine the behavior and effects of implanted ceramic nanomaterials on the material microstructure. Finally, I will share the results of mechanical testing of these materials compared to base Inconel 718 at both room and elevated temperatures, and I will conclude focus on the ARC vacuum vessel by discussing the implications of the high temperature performance of these composite materials towards the goal of improving survivability under full-power operation of ARC. In Chapter 7 I will then shift focus towards Nb. Here, I will detail the process I undertook to develop printing parameters and enable bulk-scale printability of a particularly difficult to print refractory metal that had not yet been well-explored, and I will explain the progression from single-layer exploration to multi-layer verification to machine-learning-based optimization. Lastly, Chapter 8 will provide a summary of the work and major accomplishments presented in this thesis and reiterate areas where further research will be especially

beneficial, which I hope will help to guide the work of future researchers and help support the overall goal of rapidly developing materials that will enable a clean energy future.

Chapter 2

Status of Materials for ARC Vacuum Vessel

Among the many challenges being faced by the modern materials research community in the midst of a rapidly changing energy production landscape, the design of structural components for power generation by nuclear fusion stands out as both one of the most difficult and one of the most time sensitive. Current designs for fusion reactors, and particularly magnetic confinement tokamaks, present harsh temperatures, high thermomechanical stresses, and aggressive chemical environments on par with or exceeding traditional power reactors with the added complication of neutron irradiation at energies and fluxes far greater than current fission technology. Though research on such reactors has been the subject of decades of work, dating back to the onset of nuclear power as a general concept, considerable work remains in materials design and verification as improvements in understanding of plasma physics and radiation effects continue to push design parameters to new extremes. In order to be meaningful towards the adoption of a cleaner, greener society and the fight against climate change, this work also needs to bear fruit rapidly, as full-scale fusion pilot plants will almost certainly need to be operational and producing net power with reasonable economic efficiency within the next two decades at minimum in order to expand to commercial utilization and compete with other renewable sources seeking to dominate the market by 2050.

Of the tokamak designs currently being planned or under construction, the ARC reactor put forth as part of a collaboration between MIT and Commonwealth Fusion Systems presents an especially difficult environment for structural materials. Plans for this system call for the implementation of large-volume, high-field superconducting magnets to operate with a magnetic field of 9.2 Tesla and produce fusion power equivalent to that planned for ITER in a space of about half the linear dimension.[1] Based on design plans described by Sorbom et al in 2015 [2], successful operation of such a device will require the use of a double-walled vacuum vessel that is compatible with a FLiBe molten salt (utilized as both coolant and tritium breeder) and that can operate under nuclear heating up to 26 MW and neutron irradiation up to 44 dpa per full-power year. Assuming the use of a planned 1 cm thick tungsten first wall for plasma containment and tritium breeding, the expected uniform radiative heat flux at the inner wall of the vacuum vessel is 0.2 MW/m^2, which will translate to a peak vacuum vessel temperature of approximately 760˚C. These conditions already far exceed plans for ITER [3], which call for materials to operate in conditions up to 200˚C and less than 1 dpa, as well as plans for DEMO [4], which reach up to nearly 550˚C and 5 dpa per year, with water-cooling applied for both. As such, the harsh conditions utilized as criteria for material selection in these reactors have already become insufficient, and a thorough reexamination of currently available materials must be conducted with a specific focus on ARC conditions to establish the proper path forward in material selection and to identify the most high-value research priorities for the short term. In the present chapter of this thesis, I seek to make such recommendations by examining key properties of four material classes currently considered among the most promising for fusion structural applications: nickel superalloys, reduced activation ferritic/martensitic steels, vanadium alloys, and SiC-based ceramic composites.

2.1 Nickel Superalloys

Nickel superalloys are a class of nickel-chromium materials, often featuring high quantities of iron or cobalt and a wide variety of alloying elements, which are highly favored in the power and aviation industries for their superior high-temperature performance. These materials stand out due to their unique combination of an FCC γ solid-solution matrix with

coherent strengthening γ' (Ni_3X, with X as Al, Ti, or Mo) and/or γ" (Ni_3Nb) precipitate phases, which enable extraordinary retention of mechanical properties, especially creep and fatigue resistance, up to temperatures surpassing $0.6T_m$ (melting temperature) [5]. The improved high-temperature longevity afforded by these microstructural features have made nickel superalloys a staple material for structural components in a wide variety of gas turbine designs for both jet propulsion and electricity generation [6–8], as well as for various miscellaneous components (plates, bolts, springs, etc.) in tokamak designs, including ITER [3], and MIT's now-decommissioned Alcator C-Mod [9]. In this section, we discuss properties of nickel superalloys relevant to utilization as a vacuum vessel structural material in the ARC tokamak, specifically focusing on Inconel 718, which offers among the best combinations of strength, ductility, and fabricability [10].

2.1.1 Unirradiated Mechanical Properties

Due to their complex multi-phase microstructures, properties such as strength and mechanical robustness of nickel superalloys are highly affected by the state of three generalized features: 1) solid solution hardening based on the concentrations of elements in the γ FCC phase, 2) precipitate hardening associated with the coherent formation of γ' and γ" phases, 3) and precipitate hardening associated with the incoherent formation of carbide and boride phases from trace impurities or purposeful additions [11]. The interplay of these combined effects causes a high dependence of the capabilities of superalloys on the specific heat-treatment and aging process followed, which introduces a level of tunability over the strength/ductility trade off that could be considered advantageous. This also lowers stability of the microstructure once an upper limit temperature has been surpassed, but a large part of the attractiveness of these alloys is that this upper limit is at a much higher homologous temperature than is typical for competing traditional metals. At room-temperature, as-produced, untreated Inconel 718 may feature room temperature yield strength 500 MPa, ultimate strength around 900 MPa, and be capable of approximately 45% elongation before failure, but the correct treatment process may raise yield strength over 1200 MPa and ultimate strength over 1400 MPa or higher, while maintaining elongation above 17% [10].

When operating at high temperatures, nickel superalloys have been demonstrated to receive great benefit from the presence of the coherent γ' strengthening phase specifically, which has been demonstrated to impart an increased strengthening effect with rising temperature up to and beyond 800˚C, competing with and in many cases overcoming the softening of the γ phase [12]. Ugolotti et al [13] reported maintaining yield strength above 800 MPa to 650˚C, above 500 MPa to 760˚C, and an upper limit of usability of 815˚C, at which temperature the yield strength was listed as 330 MPa, all for a 3D printed Inconel 718 material. Wrought Inconel 718 bars have also been reported to reach even higher values, as a report from the Nickel Institute [14] lists yield strengths up to 965 MPa at 650˚C and up to 800 MPa at 760˚C, though neither of these publications described the applied heat treatment utilized to reach these properties.

To provide a point of comparison specifically relating to ARC, we can consider these high temperature mechanical properties in the context of the specific temperature and stresses that are expected to be applied to the vacuum vessel. As discussed previously, the peak temperature expected at the inner wall of the vacuum vessel will be approximately 760˚C. Sorbom et al's report on the design of ARC [2] suggested that an inner wall thickness of approximately 1.5 cm would be necessary for Inconel 718 to reach a factor-of-safety (FOS) of 1, where the peak stress expected from a worst-case scenario unmitigated, asymmetric plasma disruption would match the yield stress of the material. This value was calculated based upon an Inconel 718 yield strength of 940 MPa at 760˚C, citing a Special Metals report from 2007, SMC-045 [15]. In reviewing this report however, I found that the data may have been misinterpreted when used in the ARC calculations and that the yield strength at 760˚C is only listed as reaching 800 MPa, in line with the data published by the Nickel Institute [14]. Using this 800 MPa therefore and assuming inverse proportionality between FOS and wall thickness, I assign Inconel 718 a required wall thickness of 1.75 cm to reach FOS = 1.

Although these Inconel 718 materials achieve seemingly excellent high-temperature yield strength, the goal temperature of 760˚C exceeds the upper temperature limit of the materials, which is typically stated to be around 650˚C. Beyond this temperature, toughness of the material is found to rapidly decline due to loss of ductility, which in turn results in a significant degradation of creep resistance. Wrought Inconel 718 bars are reported to

achieve a 1000h stress rupture strength of 595 MPa at 650˚C, but this value drops to less than 200 MPa by 760˚C [16], about 25% of the total yield strength. Although stresses associated with the worst-case disruptions have been discussed, these are expected to be rare occasions that would ideally be preventable. The largest contributor to steady state force on the vacuum vessel should be buoyancy from the molten salt coolant [2]. These forces may be unlikely to reach 200 MPa in the designed system, but the low creep strength to yield strength ratio still presents a significant limitation on the expected lifetime of the vacuum vessel, which is sure to be exacerbated by the effects of neutron irradiation and transmutation. While alternative nickel superalloys are available that have been designed for higher temperature operation (e.g., Astroloy or Inconel 939), these feature high cobalt content that would increase activation and/or are less readily available and machinable, decreasing their attractiveness as candidate materials. 718 therefore currently remains the most highly considered nickel superalloy option.

2.1.2 Irradiated Mechanical Properties

Of particular concern for lifetime decreasing effects of neutron irradiation for nickel-based alloys is the potential for embrittlement from transmutant helium production. At high neutron energies such as those at play in fusion environments, several pathways to helium production become activated for the elemental components of nickel superalloys, including an indirect pathway for the most abundant nickel isotope, ^{58}Ni, which can undergo (n,γ) reaction to produce ^{59}Ni and gain a relatively high neutron capture cross section for a (n,α) reaction [17]. Furthermore, helium migration becomes especially problematic when particles are allowed to agglomerate into bubbles and stabilize large voids in the material microstructure, and this problem is exacerbated in nickel, which has relatively poor He-vacancy binding and high vacancy formation energy [18]. Changes in the capability for generated helium particles to migrate can have a significant effect on the level of degradation, however. In a study by Sencer et al [19] high-energy protons and spallation neutrons were utilized to achieve 1830 appm He at low temperatures less than 60˚C, and no cavities were observed to form, likely due to the insufficient mobility of the He atoms. The cavity formation effects of He are well understood to ramp up at higher temperatures, but effects are also known to decrease again upon reaching a saturation temperature where

vacancy ejection from voids begins to match diffusion into the voids [20]. It is possible that this will actually be the case for the ARC reactor and that void formation from He may actually be decreased compared to previous fusion reactor designs due to the increased operating temperature, though this seems unlikely when considering the relatively high production rate expected and that lower temperature irradiation conditions will not be completely avoidable. Regardless, experiments have not yet been performed which could approximate the true helium production rate under full-power operation, and more data is certainly needed here to determine the extent of property degradation. Assuming that the rate of vacancy ejection does not overcome He accumulation at the production rate of ARC (currently approximated at 280ppm per full-power year [2]), the embrittlement effect and its associated degradation of creep properties could be expected to be the limiting factor in the vacuum vessel lifetime for Inconel 718; restricting helium accumulation and improving creep resistance should be the primary focus of research to improve the usability of 718 for near term usage.

Another key concern with the introduction of high neutron flux is the potential for dissolution of precipitates. At temperatures below 60˚C, Sencer et al [19] reported complete disappearance of both γ’ and γ" precipitates at doses less than 1 dpa, and at temperatures below 250˚C, Carsughi et al [21] reported the same occurrence at approximately 10 dpa from 800 MeV protons. Studies on Inconel X-750 by Zhang et al [22] found that recombination reaches a high enough rate to maintain a stable γ’ phase above 500˚C, so this again may not be as significant of an effect under ARC conditions, but, again, studies under full-power conditions with fusion-level neutron irradiations will be necessary to fully verify.

2.1.3 Molten Salt Compatibility

Due to the rarity of facilities well-equipped for experiments involving molten salts, few studies have been conducted to observe the corrosion effects of FLiBe, and no studies were found which included alloy 718. As such, prediction of compatibility in this section is primarily based on the results of two studies which observed the effects of FLiBe on comparable nickel superalloys. First, a 1977 report by J.R. Keiser out of Oak Ridge National Lab [23] detailed the corrosion of Hastelloy N (with variations in Cr and Nb

concentration) as well as Inconel 601 in fuel for the Molten-Salt Breeder Reactor with formula LiF-BeF_2-ThF_4-UF_4. Results of this study found that the primary source of corrosion was oxidation of Cr by reaction with impurities in the salt. Namely, small quantities of HF and FeF_2 that formed in the molten salt were found to react to form CrF_2. Notably, results indicated that the reaction limiting step was the diffusion of Cr through materials and that addition of Cr to Hastelloy N resulted in proportional increases in weight loss, though Nb addition did not appear to have an effect. In a more recent study in 2009 by Kondo et al in association with the National Institute for Fusion Science in Japan [24], a similar experiment was conducted to observe the corrosion effects of FLiBe on Hastelloy C-276, Inconel 600, and Inconel 625. Results were similar to those achieved previously by Oak Ridge, and corrosion rates were estimated for Hastelloy C-276, Inconel 600, and Inconel 625 in static FLiBe at 600˚C as 3.4μm/yr, 2.8μm/yr, and 1.1μm/yr, respectively. These values could be an acceptable level of loss for a wall of 1 cm minimum thickness that is designed to be replaceable, and the expected fluid flow velocity in ARC of 2 m/s [2] would not be expected to raise these values to a level of concern. Of the materials tested, Inconel 625 achieved the lowest corrosion rates and could be considered the most chemically similar to 718, but 718 contains even lower quantities of Cr. Inconel 718 is therefore considered to be a good fit for the proposed FLiBe coolant in ARC.

2.1.4 Neutron-Induced Activation

Inconel 718 is known to be a particularly high-risk material with regards to fusion neutron activation due to the high quantities of nickel, molybdenum, and niobium, all of which are high activation elements. While elemental substitution and/or isotopic redesign are considered in some cases to decrease activation, these elements play too substantial of a role in Inconel 718 for any significant improvements to be feasible in this way [25]. Using traditional compositions therefore, a calculation of predicted activation levels has been conducted for Inconel 718 (alongside other candidate materials) in previous work reported by Bocci et al [26]. Following two full-power years in the ARC reactor and 100 years of cooling time, an Inconel 718 vacuum vessel is predicted to maintain an activity of nearly 1011 Bq/kg and a dose rate exceeding 1 Sv/h, which would prohibit recycling or shallow land burial and imply the need for remote maintenance and operation procedures for ARC

over long periods of time. This is a serious point against the recommendation of nickel superalloys for vacuum vessel candidacy, and one for which there are no apparent paths for improvement.

2.1.5 Manufacturability and Repairability

Nickel superalloys have a long history of usage, and though difficult to machine, production and standardization of quality have become quite well-established. Inconel 718 in particular has been in the market for 60 years and is used thoroughly in power generation and extreme environment applications, currently accounting for about 30% of the mass of a modern airplane engine [27]. 718 is also a fairly weldable material and has good resistance to heat-affected-zone and strain age cracking behavior [28]. As such, it is expected that welding repairs could be made to a 718 reactor system with little degradation of mechanical capabilities without post-weld heat treatments, which is a desirable quality for a vacuum vessel. Furthermore, 718 has been well studied for additive manufacturing processes, especially powder bed fusion processes, and is printable with excellent quality [29–31]. This may be a valuable trait in the production of reactor prototype components, or even the eventual manufacturing of the final vacuum vessel, as it introduces new capabilities for advanced geometry designs and may enable construction of the vessel as a single component as the technology improves, decreasing weak points from welding.

2.2 RAFM Steels

Steels have been an integral part of nuclear reactor design from inception to the modern day. Low carbon/low alloy steels and 300-series austenitic stainless steels are the dominant materials for core structures and pressure boundary components in essentially every class of commercial fission power reactors [32–34]. Austenitic steels have also historically been the materials of choice for vacuum vessels in early-stage fusion prototype reactors. MIT's previous tokamak reactor, Alcator C-Mod, utilized a vessel primarily made up of 304L stainless [35], and current designs for the under-construction ITER vessel also consist primarily of 316L(N)-IG38, though it could be said that these design choices were made primarily based upon cost and ease of manufacturing, as the prototype reactors were not

intended for continuous or extremely high-temperature operations. Though austenitic steels have found widespread usage with great success in a variety of nuclear applications, concerns with susceptibility to irradiation-induced void swelling have led to an increased focus on ferritic/martensitic steels for harsher environment applications, and these are considered to have much higher promise in terms of applicability to eventual full-power fusion [36]. With inherently high resistance to void swelling under irradiation in addition to their strong mechanical properties, these BCC steels have undergone considerable studies for application in more extreme radiation environments [37]. 7-9 wt% Cr alloys have shown particularly promising results, owing to their combination of excellent radiation resistance and considerable corrosion and oxidation resistance [38]. Furthermore, specific consideration of advanced fusion reactor needs has led to the development of reduced activation ferritic/martensitic (RAFM) steels, 7-9Cr tempered martensitic steels that have purposefully been designed with substitutes for elements that may produce long-lived radioactive isotopes, namely Cu, Mo, Ni, Nb, and N. These reduced activation materials have been well studied and have demonstrated no significant loss of desirable properties compared to their high-activation counterparts, and so discussion in this section will focus on the advantages of these RAFM steels along with the challenges for their utilization in an ARC-like reactor.

2.2.1 Unirradiated Mechanical Properties

RAFM steels, despite being referred to as ferritic/martensitic, essentially all derive their strength from the formation of martensitic laths among equiaxed austenitic grains. For a typical 7-9Cr material, the microstructure is established via a two-step final heat treatment involving a normalization step at about 1000˚C for half an hour followed by tempering at about 750˚C for an hour [37]. This process develops the desired martensites, and the material is further strengthened by the formation of $M_{23}C_6$ metal carbides at the grain boundaries and high quantities of nitride and carbide secondary hardening precipitates dispersed throughout the matrix. Following processing steps like the generalized treatment described, the most well-studied RAFM materials, including NS1, EUROFER97, CLAM, and F82H, have achieved consistent mechanical properties [39–41]. At room temperature, typical yield strengths are slightly above 500 MPa, ultimate tensile strengths reach to

around 650 MPa, and elongation can exceed 20%. These properties are also well maintained to moderately low and high temperatures, with typical DBTTs at -60˚C or lower and good retention of strength and ductility up to 400-500˚C. Beyond this upper temperature range however, softening rates have been demonstrated to sharply increase, causing rapid degradation of strength with increasing temperature [41], which can likely be largely attributed to instability of the metastable martensites. In short-term mechanical tests, yield strengths of RAFM steels were typically found to degrade to around 300 MPa by 600˚C [39,40], while long-term testing demonstrated the formation of laves phases and M_6C-type carbides in this temperature regime, which resulted in further loss of toughness and considerable increase in DBTT [42].

Few studies have been conducted with RAFM steels up to the ARC-relevant temperature of 760˚C, but yield-stress of F82H RAFM steel has been demonstrated to closely resemble values for the conventional Cr-Mo steel MANET-II at elevated temperatures, which achieved yield strength just below 100 MPa at 760˚C [41,43]. Achieving FOS=1 with a yield strength of 100 MPa is predicted to require an inner vacuum vessel thickness of 14 cm, already about an order of magnitude more than the nickel superalloys, which would result in significant increase in vacuum vessel weight and cost. Furthermore, extrapolation of creep data for F82H and EUROFER97 [44] would suggest that creep rates may exceed even 1%/h at less than 100 MPa of consistent applied stress at 760˚C. Even before degradation related to irradiation, use of this material seems impractical at the goal temperature, and it seems likely that usage should be limited to applications with maximum operating temperatures of 550˚C or less. If feasible, research aimed at raising the high temperature operability limits will be the most essential for integration of RAFM steels in ARC-like systems.

2.2.2 Irradiated Mechanical Properties

Radiation effects on mechanical properties in RAFM steels have been found to be highly temperature dependent. Of particular interest, several reports on neutron irradiation experiments conducted on EUROFER97 in preparation for the DEMO reactor have found that, although low temperature irradiation results in significant hardening and embrittlement, irradiation above about 400˚C appears to have little to no effect on

mechanical properties [45–47]. Furthermore, low temperature irradiation effects have been found to be recoverable via annealing around 550˚C, and helium effects were expected to be tolerable up to at least 400appm He for helium to dpa ratios of less than 10appm He/dpa [48]. Finally, effects of irradiation on DBTT were found to follow a similar trend, increasing to over 100˚C for high dose neutron irradiation conducted at mid-range temperatures around 300˚C before dropping again to below freezing levels at irradiation temperatures over 400˚C [45,46]. The culmination of these results suggests excellent compatibility of RAFM steels with high-dose neutron irradiation environments like ARC if the operating temperature can be set around 550˚C. As is the case with all discussed materials, however, further study under full-power fusion relevant conditions will be required to verify this compatibility.

2.2.3 Molten Salt Compatibility

When considering compatibility of a FLiBe molten salt with RAFM steels, temperature is once again the primary point of concern. Based on the upper limit temperature established for RAFM steels and the lower limit temperature established by the solidification point of FLiBe [49], the molten salt channel will be limited to a narrow operational window of 460-550˚C, though this window would practically be narrowed further to avoid temperatures extremely near solidification. It must also be considered that the operational temperature of the FLiBe represents the lower operational temperature of the inner vacuum vessel. In this case, the 550˚C limit must be imposed on the plasma-facing side of the vacuum vessel, and the temperature on the coolant-facing side of the vessel could be much lower based on the required thickness of the wall unless additional external heating were applied. While operating within these tight restrictions may be possible, the difficulties they present alone may be enough to consider RAFM steels incompatible with FLiBe. If a RAFM vacuum vessel is determined to be the best course of action, other molten salts such as liquid lithium or lithium-lead may offer wider operational windows, but the loss of beryllium would have a large impact on tritium breeding.

In terms of corrosion, several experiments with JLF-1 RAFM steel and FLiBe have been conducted without suggesting serious weight loss [50,51]. Muroga et al [50] reported a FLiBe/JLF-1 corrosion rate of approximately 1 μm/yr at 550˚C. This study also suggested

that exposure to FLiBe may result in the dissolution of martensites and the formation of ferritic phases instead, but that this reaction is driven by the concentration of N in the steel, which may be feasible to limit if this reaction is deemed detrimental.

2.2.4 Neutron-Induced Activation

RAFM steels have been compositionally tailored with the specific goal of lowering activation in high-energy neutron environments through the replacement of Cu, Mo, Ni, Nb, and N with low-activity substitutes. Based on the simulations performed by Bocci et al [52], an ideal EUROFER97-class RAFM steel after 2 full-power years and 100 years cooling would be expected to reach specific activity on the order of 108 Bq/kg and a dose rate on the order of 10^{-5} Sv/h, qualifying the material for in-plant recycling. These values are made based on the assumption that impurities can be avoided in vessel production, however, which does not seem to be a realistic expectation based on current manufacturing capabilities. Accounting for the typically observed EUROFER97 impurity concentrations, which includes trace amounts of Ni, Mo, Nb, and other high-activity producing elements [53], expected dose rate is found to increase about two orders of magnitude to the order of 10^{-4} Sv/h, preventing recycling [52]. It should also be considered that the expected increased thickness required for a RAFM vacuum vessel compared to a nickel superalloy would result in a larger tonnage of activated waste. However, the 1000x decrease in activity of RAFM compared to nickel superalloys could be stated to be a much more crucial factor.

2.2.5 Manufacturability and Repairability

RAFM steels have been under development since the 1980s and have been highly studied for nuclear applications, both fission and fusion [54]. Manufacturability of these materials is not expected to be extraordinarily difficult, but current utilization will be limited by a lack of supply chain maturity and excessive cost of production from rare substitutional elements (e.g., Ta) and requirements for restricting impurities [55]. Welding of RAFM steels is expected to require post-weld heat treatments to redevelop martensite structures and maintain sufficient mechanical properties [54], which will increase the difficulty of maintenance and repairs in-operation.

2.3 Vanadium Alloys

Compared to the nickel and steel alloys previously discussed, vanadium-based alloys could still be considered a rather new and developing class of material. Usage of vanadium as the elemental base of structural materials has been historically extremely limited, with most interest in vanadium restricted to utilization as an additive in steels for improving strength or corrosion resistance. However, recent decades have seen a marked increase in the development of nonferrous vanadium materials, especially with intentions for fusion applications due to their unique combination of high-temperature applicability and low neutron activation properties. V-Cr-Ti alloys particularly have risen in prominence, with small additions of chromium offering improved solid solution strengthening at elevated temperatures and titanium aiding in the removal of interstitial impurities to improve ductility [56]. Of the V-Cr-Ti iterations that have been considered to this point, V4Cr4Ti has achieved among the best combinations of overall mechanical properties and manufacturability and is nearly universally considered to be the leading vanadium option for a fusion vacuum vessel [57–61]. In this section, we discuss the potential benefits and remaining work for application of vanadium alloys towards an ARC-like fusion system, with a primary focus on the V4Cr4Ti class of materials.

2.3.1 Unirradiated Mechanical Properties

Due to the low usage of vanadium-based alloys outside of growing fusion-focused research, standardization of processing and consistency of properties is still being established, and slight improvements in performance may still be forthcoming. At present, most heat-treatment processes involve simple annealing for some period around 1000˚C under vacuum, presenting a mostly solid-solution microstructure with some strengthening resulting from the formation of Ti-based precipitates with C, N, and O impurities. Room temperature tensile testing of V4Cr4Ti has typically demonstrated yield strengths exceeding 300 MPa, ultimate tensile strengths of approximately 400 MPa, and total elongations near 30% [62,63]. In the unirradiated state, V4Cr4Ti achieves a very reasonable lower operating temperature range, with a DBTT less than -200˚C [59,64]. As

a refractory alloy, vanadium is especially well suited for higher temperature operation. Melting temperature for V4Cr4Ti has been reported as approximately 1900˚C [65], and an operability limit has been suggested as $0.49T_M$ [57], indicating potential usability up to more than 900˚C. Across this spectrum, the alloy demonstrates excellent retention of both strength and ductility, and depending on batch and impurity levels, high-temperature tensile testing has demonstrated yield strengths above 200 MPa, ultimate tensile strengths above 350 MPa, and total elongations above 15% to 700-800˚C or higher [62,63,66]. Within the intermediate elevated temperature regime of about 300−700˚C, dislocation glide remains the primary deformation mechanism and dynamic strain aging is observed in stress-strain curves, likely due to the interactions of the dislocations with interstitial impurities. Significant softening is not apparent until beyond approximately 850˚C [66].

Operation at the planned ARC temperature of 760˚C appears to fall well within the acceptable limits for V4Cr4Ti. At this temperature, top performing heats of the material have demonstrated yield strengths near 230 MPa [62]. Due to the low strength of the vanadium alloys compared to nickel superalloys, utilization in ARC will require increased thickness, with a recommended inner vacuum vessel thickness of approximately 6 cm required to achieve FOS=1. However, the ratio of creep strength to yield strength is much more favorable in V4Cr4Ti, with biaxial creep tests in liquid lithium at 800˚C resulting in a 1000h stress rupture strength of approximately 100 MPa [67], 43% of the 760˚C yield strength. If production of a 6 cm thick vessel is found to be reasonable, then this result suggests much improved longevity over the nickel alloys in terms of creep. Additionally, if further improvement in creep strength is deemed necessary, then other variations in composition such as V5Cr3Ti and V7Cr5Ti are available that may meet this need, though at the expense of some ductility and manufacturability [68].

2.3.2 Irradiated Mechanical Properties

Primary concerns for the effects of neutron irradiation in a BCC system such as vanadium will be increase in DBTT, embrittlement effects of helium implantation, and loss of high-temperature creep properties diminishing the operating temperature window. V4Cr4Ti is particularly favored among vanadium vacuum vessel candidates in part due to its excellent retention of DBTT. For irradiations up to 34 dpa in the temperature range 427−599˚C,

V4Cr4Ti was found to maintain DBTT less than −200˚C with reasonable room temperature ductility (>8%) and low volume changes due to irradiation-induced swelling (<0.3%) [59]. The most severe hardening and embrittlement effects from neutron irradiation in vanadium alloys have been observed to occur at an intermediate irradiation temperature below 400˚C [60,69,70]. This regime is characterized by the formation of a high number density of dislocation loops and flow localization manifesting in dislocation channeling [71], and high-dpa mechanical property testing demonstrated 2- to 3-fold increases in yield strength with accompanying severe embrittlement [72]. However, these hardening effects are significantly diminished in higher temperature regimes above 400˚C, and annealing processes above 600˚C have achieved excellent recovery of ductility [69], which may make the higher operational temperature of the ARC design advantageous for vanadium structural materials over traditional tokamak designs. For scenarios in which <400˚C irradiation conditions cannot be avoided, detrimental embrittlement effects have been strongly linked to dislocation interactions with interstitial impurities within the system, and the addition of small quantities of Al, Si, and Y, which promote formation of Ti-precipitates with O, N, and C, has been demonstrated to improve retention of uniform elongation [73].

Although neutron damage resistance is minimized in the high-temperature regime, currently available data suggests that helium embrittlement will become more severe, resulting in significant loss of ductility for systems with >25 appm He at temperatures >650˚C [74]. This effect will impose an upper limit on operating temperature for the vanadium systems. Data remains limited however, especially for reasonable reproductions of fusion environmental conditions, which makes prediction of this upper limit difficult without more in-depth testing. Data for irradiation effects on creep in V-Cr-Ti alloys is found to be even more scarce, and this will also require further exploration before the material can be reasonably selected as a primary candidate. As these properties become better understood, they will likely become the primary targets of improvement (along with tritium resistance) for the advancement of vanadium alloys in the coming years.

2.3.3 Molten Salt Compatibility

Vanadium-based alloys are well understood to have a high affinity for gaseous elements, making them particularly susceptible to corrosion and oxidation when exposed to the environment, such as in the case of a vacuum-leak [75]. This is an issue which may require serious consideration for the application of a vanadium vacuum vessel. However, in an ideal-use situation without failures or breach of vacuum, compatibility of vanadium-based alloys with the FLiBe molten salt can be the primary focus. Although quantitative measurements of actual weight loss in a V4Cr4Ti/FLiBe system are difficult to come across, consensus seems to be that this corrosion is expected to be low and not present much issue [72,76,77].

Of greater concern is the issue of tritium accumulation in the vanadium structure, owing to its high tritium solubility compared to FLiBe [58,71]. Such accumulation in the vacuum vessel structure would cause significant embrittlement and disrupt the necessary tritium recycling process. A 2004 study by Chen et al [78] found that V4Cr4Ti experiences a total loss in ductility at 310 wppm hydrogen in the alloy. Additionally, a 2014 report from Muroga et al [58] revealed that, at 1000K (730˚C), a reasonable range of tritium level in FLiBe (0.01 appm) would equate to approximately 100 kg of tritium in the V4Cr4Ti structural materials of an FFHR reactor. This presents a significant issue for the functionality of vanadium in a fusion system. One solution under consideration is to dissolve fluoride materials such as WF_6 or MoF_6 into the FLiBe, which will promote the reaction from insoluble T_2 to highly soluble TF [71,79]. This solution may be expected to reduce tritium mobility and permeation enough to make vanadium a feasible material, but further testing will be required to fully verify the concept.

2.3.4 Neutron-Induced Activation

As discussed with nickel superalloys and RAFM steels, activation analysis for a vanadium-based vacuum vessel in a theoretical full power operation ARC system has been directly considered in the 2020 report by Bocci et al [52], though findings in this study were for a V15Cr5Ti alloy rather than the V4Cr4Ti that has been the primary focus of discussion. Findings for an ideal V15Cr5Ti with no impurities after 2 full-power years and 100 years

cooling were a specific activity of approximately 107 Bq/kg, which is more than an order of magnitude lower than even the RAFM steels, and a dose rate very similar to the RAFM steel on the order of 10^{-4}-10^{-5} Sv/h. Accounting for realistic impurities (including oxygen, nitrogen, carbon, silicon, and some iron based on compositions reported by Loomis et al [59]) results in very little change in these activity and dose rate values during the first hundred years, and, even with impurities, V15Cr5Ti reaches recycling limits and requirements for shallow land burial in just over a century [52]. These results could be expected to be similar for the V4Cr4Ti, which does not include any further elemental additions that might increase activation.

2.3.5 Manufacturability and Repairability

Strict requirements in vanadium material preparation, especially with regards to carefully controlling impurity levels to maintain properties and low activation requirements, make fabrication a complicated process. To meet the necessary specifications, use of electron beam melting for refinement and high vacuum conditions during fabrication has become the norm [72]. Use of this method has resulted in V4Cr4Ti products out of the US [80], Japan [81], France [82], and China [83] with comparable properties, indicating that fabrication is becoming more standardized. Good weldability has been achieved, especially in high-purity samples, by Gas Tungsten Arc or laser welding [71]. Retention of strength in weld joints is adequate, but dissolution of Ti-precipitates during welding has been shown to increase sensitivity to neutron irradiation, making high-temperature post-weld heat treatments necessary to maintain the DBTT [58]. This may prove to be a considerable challenge for practical utilization of the alloy.

2.4 SiC Ceramic Composites

With excellent high-temperature capabilities, general resistance to corrosion and oxidation, and high strength-to-weight ratios, ceramic materials present an interesting alternative for extreme environment applications. SiC in particular is considered extremely attractive for fusion power systems due to its stability in aggressive environments and low-activation composition, but extreme brittleness makes fabrication of structural components with pure

SiC practically impossible. To enhance utility for possible load-bearing applications, composite materials were engineered featuring SiC fibers interspersed in a SiC matrix with thin coating layers in between. These composites, commonly referred to as SiC/SiC, are designed to deform with pseudo-ductility by isolating stresses in individual fibers which fracture without propagation of the cracks [84]. The result is a predictable delay in failure that increases capability for structural usage of a material that would typically be prohibitively brittle. Considerable work remains before implementation of SiC/SiC in any large-scale structural component will be feasible. However, the unique potential for extreme temperatures >1000˚C with a low activation material merits a push for rapid development. In this section, we will discuss the present compatibility of SiC/SiC for ARC, specifically focusing on near-stoichiometric, high-crystalline SiC/SiC produced by chemical vapor infiltration (e.g., Hi-Nicalon Type S fibers with pyrolytic SiC matrix), which is currently considered the "nuclear grade" material [85].

2.4.1 Unirradiated Mechanical Properties

Room temperature properties for SiC/SiC increase almost an order of magnitude over those of a standard non-composite SiC. Tensile strength is on the order of 300 MPa for chemical vapor infiltrated composites but can reach over 500 MPa depending on fabrication methods, while fracture toughness is on the order of 16 $MPa/m^{1/2}$ [86]. Although the pseudo-plastic deformation resulting from fiber bridging and sliding enhances usability, the materials remain extremely brittle with total elongations <1%, which may still be prohibitive for vessel fabrication. The fiber reinforcement structure of the composite can also introduce a level of anisotropy, as strength can be dependent upon stress-direction versus fiber orientation.

In a non-nuclear environment, the upper limit usability temperature of SiC/SiC will depend on oxidation resistance, which is found to diminish at approximately 1700˚C [87]. Load-displacement data indicates that strength and fracture mechanisms remain consistent from room temperature up to approximately 1200˚C [88], far exceeding the allowable temperature limits of the metal structures and introducing new options for even further increased thermal efficiency in a fusion reactor. Considering the current specifications for ARC, we can assume that unirradiated SiC/SiC will operate with strength of close to 300

MPa at the target temperature of 760˚C, which would require an approximately 4.5 cm thick wall to meet FOS=1. Creep is also not expected to be an issue at this temperature in the unirradiated state, as third generation SiC/SiC materials have demonstrated good creep rates for loads above 300 MPa up to much higher temperatures (1200˚C) [89]. The excellent creep behavior can be partially attributed to the stress-sharing capabilities associated with the fiber/matrix structure, which enables creep rate to be determined by the best performing material within the composite.

2.4.2 Irradiated Mechanical Properties

Neutron irradiation effects on the mechanical properties of SiC/SiC composites have been found to be highly dependent upon selected structure and fabrication methods, which has allowed for significant fusion-focused structure tailoring to be performed over the years to help minimize degradation. Studies conducted in the ’90s on first-generation composites found unacceptably large losses in strength after minimal neutron exposure, resulting in low feasibility for high-flux fusion utilization [90]. However, studies conducted just a few years later in 2002 demonstrated dramatic increases in radiation resistance for third-generation composites, especially those fabricated with Hi-Nicalon Type-S or Tyranno SA3 fibers [91]. These improved SiC/SiC composites were found to display no loss in flexure strength for neutron irradiation to 7.7 dpa at 800˚C and were also found to have good retention of fiber/matrix density ratios, which was a considerable problem for previous iterations due to mismatched swelling/shrinking. In more recent studies, SiC/SiC materials consisting of Hi-Nicalon Type S fibers in a CVI SiC matrix with PyC/SiC multilayered interphases were tested to >70 dpa in HFIR, and saturation of changes in swelling, thermal conductivity, and Young’s modulus were observed at less than 2 dpa [92]. At these extreme dpa levels, some decrease in flexural strength was found to occur. This effect was most significant at intermediate temperatures around 300 ˚C and fairly moderate for irradiation at the target ARC operating temperature around 800˚C, but the degradation was associated with damage to the fiber/matrix interface [85], which, unlike degradation in metals, would not experience any annealing self-repair once temperatures are raised. Neutron irradiation has also been shown to destabilize pyrolytic carbon interfaces and result in decreased interfacial debond shear strength and interfacial friction

stress [93]. However, this effect was most notable for irradiation temperatures >1000˚C, and the composites suffer few practical consequences from this degradation at lower temperatures [94] .

One remaining critical unknown which must be further studied for SiC/SiC is the effect of transmutations. SiC is expected to undergo a much higher level of transmutations than the discussed metal alloys in the fusion neutron regime, with studies suggesting that production rates could reach 50-180 appm/dpa for helium and 20-70 appm/dpa for hydrogen [95]. In light of the already extreme brittleness of these materials, further embrittlement from gas accumulation may not be the primary concern, but enhanced swelling would certainly be problematic, in terms of both loss of mechanical properties and further reduction of the already low thermal conductivity [96]. The effects of these gaseous transmutations, as well as the accompanying solid ones, will require further study under reactor-relevant conditions to determine the overall level of concern for properties and component lifetime.

2.4.3 Molten Salt Compatibility

SiC materials are known for their stability in aggressive chemical environments. Although data specifically relating to interactions with FLiBe are limited, Lee et al [97] have published an extensive review of the data currently available for SiC/SiC in FLiBe and FLiNaK molten salts from the perspective of implementation in a molten salt fission reactor, and their findings would appear to suggest good compatibility for an environment such as ARC. In 400h corrosion testing using FLiNaK, loss of thickness in SiC was found to be limited to about 2.5μm [98]. This corrosion was found to be significantly increased up to 12μm with the introduction of Cr impurities from container vessels, but this may impact the design of molten salt fission reactors more so than ARC. In terms of tritium permeation, SiC has demonstrated low permeability and solubility at elevated temperatures [99], which would be expected to minimize uptake and associated further embrittlement, although further study in needed to fully understand the effects of irradiation damage on this solubility. Carbon interfaces between the SiC fibers and matrix may also present increased trapping sites for tritium due to strong bonding and low diffusion, but this effect is expected to be significantly reduced for operating temperatures above 600˚C [100].

Based on these results, SiC/SiC composites are expected to perform well in contact with FLiBe coolant under ARC-like conditions, though more focused studies on the exact planned conditions are, of course, highly recommended.

2.4.4 Neutron-Induced Activation

Although SiC/SiC materials were not included in the direct activation comparison study conducted by Bocci et al [52], studies conducted for generalized fusion reactors are available that allow for adequate comparison to the other material classes discussed. Muroga [101] presents a comparison of contact dose rate for pure SiC/SiC, F82H RAFM steel, and NIFS-HEAT-2 V4Cr4Ti alloy after use in a general fusion commercial reactor first wall. This data suggests that SiC/SiC will feature the lowest contact dose rate of the considered materials for the first several decades and will reach limits for remote recycling within approximately 30 years. However, the RAFM steel and V4Cr4Ti will stabilize at a dose rate approximately an order of magnitude lower than SiC/SiC by the 100-year mark. Inclusion of impurities in the calculations might be expected to slightly increase these dose rate results, but this change should be small. SiC/SiC can therefore generally be considered an attractive material from the point of view of minimizing waste activation.

2.4.5 Manufacturability and Repairability

SiC/SiC composites have undergone significant improvements in fabrication quality and consistency in the relatively brief time period since the development of the first-generation materials in the ’90s. However, capability for complex manufacturing remains one of the largest hurdles towards vacuum vessel application of this technology. The highest performing materials currently available are typically produced via chemical vapor infiltration or a similar method. While this technique has achieved good reproducibility, it is currently hampered by long processing times, high production costs, and lack of scalability and geometric flexibility. As a result, bulk-scale part production utilizing SiC/SiC remains highly dependent upon the reliability of joining technologies. Several efforts have been made to develop these techniques with a focus on minimizing irradiation weakness of fabricated joints, and thus far decent results with low degradation have been

observed for titanium diffusion bonding, calcia-alumina glass-ceramic joining, and SiC-Al2O3-Y2O3 joining techniques up to a few dpa, but fusion-relevant testing remains necessary [102]. Even in a best-case scenario where a vacuum vessel geometry can be reasonably produced with minimal loss of properties at joints and isotropic strength throughout, the extreme inherent brittleness presents practical difficulties for implementation into the system without cracking. Furthermore, the pseudo-plastic deformation mechanism achieved by the matrix/fiber composite hinges on extending life through isolation of cracks and fiber fractures, but this process still produces permanent component defects that may compromise functionality, especially when aggravated by the effects of constant neutron bombardment [84]. Repair of damaged SiC/SiC is not currently feasible, and so any abnormal stresses may require replacement of the entire structure. For this class of material to be considered, significant improvement will be necessary in fabrication and joining processes to develop large-scale components that maintain mechanical properties throughout, repair techniques for inevitable localized fractures will need to be developed, and the long-term survivability of such a brittle structure will need to be extensively demonstrated.

2.5 Practical Implications for ARC

A qualitative visual comparison of the four material classes is presented as Figure 1 at the end of this chapter. Although no material appears to readily meet all the desired requirements, nickel superalloys and vanadium alloys would appear to have the most attainable paths to success for an ARC reactor as currently designed. RAFM steels are detrimentally restricted by their temperature operability windows, while the techniques necessary to implement and maintain the extremely brittle SiC/SiC composites may feasibly take decades more to develop. With its low activation and excellent high-temperature properties, V-Cr-Ti will be a high value candidate, achieving goals for longevity and limitations on waste. At present though, immediate implementation is prevented by the lack of reliable and scalable fabrication and the need to overcome high tritium uptake with FLiBe. Nickel superalloys appear to lie on the opposite end of the spectrum, with good compatibility with FLiBe and very achievable manufacturability but

poor outlook for longevity due to helium embrittlement and lack of creep resistance. Irredeemably high activation will also almost certainly prevent nickel from being the long-term material of choice. However, if time is a critical factor, as it appears to be for ARC, then capability for rapid construction of a pilot plant may need to be given the highest priority. Nickel superalloys are conceivably the only material available that could be constructed into a vacuum vessel and allow full-power operation for any length of time if construction were to begin today. For this reason, improving the high-temperature performance and helium resistance of these materials should be a primary focus of present fusion materials research, with the goal of extending potential vacuum vessel lifetime and maximizing the impact of a near-term ARC pilot plant. In the upcoming chapters of this thesis, I will discuss my work aimed at improving these properties through the formation of metal matrix composites.

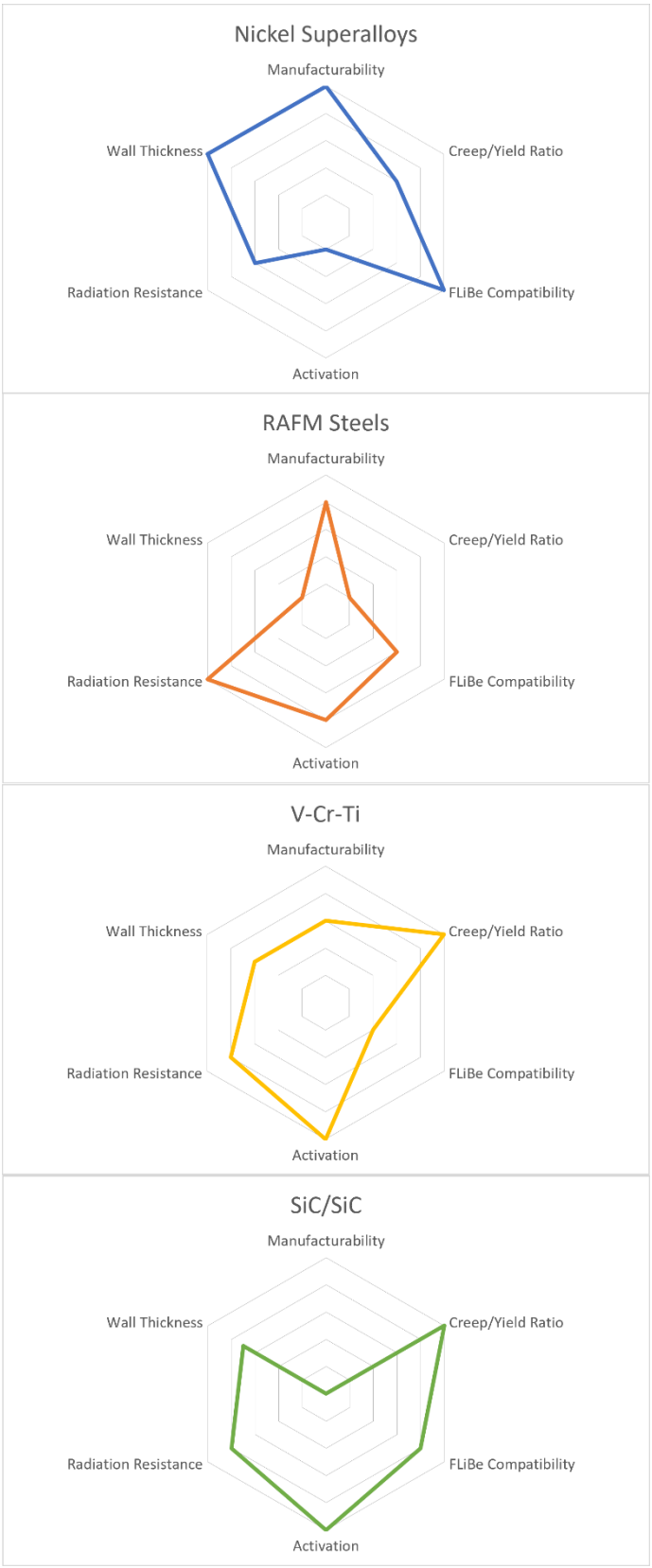

Figure 1: Qualitative comparison of material readiness for ARC

Chapter 3

The Role of Metal Matrix Composites

In breaking down the merits and failings of various material systems for high-temperature operation in a manner such as presented in the previous chapter, a pattern that is already well understood in the materials community becomes apparent. In short, metal alloys tend to offer high strength and good flexibility in implementation but lose utility with rising temperature and are very dense, while ceramic materials offer low density and excellent retention of properties to extreme temperatures but demonstrate low toughness and are difficult to implement. Research into the production of metal-ceramic composites seeks to reach a middle ground, offering increased performance beyond the typical strength/density tradeoff for metals and increasing extreme environment utility. Of particular interest are so-called metal matrix composites (MMCs), in which ceramic particles, fibers, or sheets are interspersed in a primarily metal structure, as represented in Figure 2 [103]. This design is similar conceptually to that described for SiC/SiC, which is commonly referred to as a ceramic matrix composite. In more relatable terms, it could also be compared to commonplace concrete with rebar, though with the roles of the ceramic and metal reversed.

The capability to increase high-temperature performance of existing alloys, especially nickel superalloys, may have significant implications for the near future of energy production at large and fusion energy in particular, especially if improved resistance to irradiation damage or helium embrittlement is also attained. In the following sections of this chapter, I will briefly discuss the widespread applications of metal matrix composites

outside of nuclear science to provide context for the history of the technology, I will detail how established MMCs have demonstrated promise for improved performance in nuclear environments, and I will introduce the potential for expansion of the technology that has been enabled by the adoption of additive manufacturing. This discussion will provide further motivation for the fabrication of new nickel superalloy MMCs, which will be the focus of later chapters.

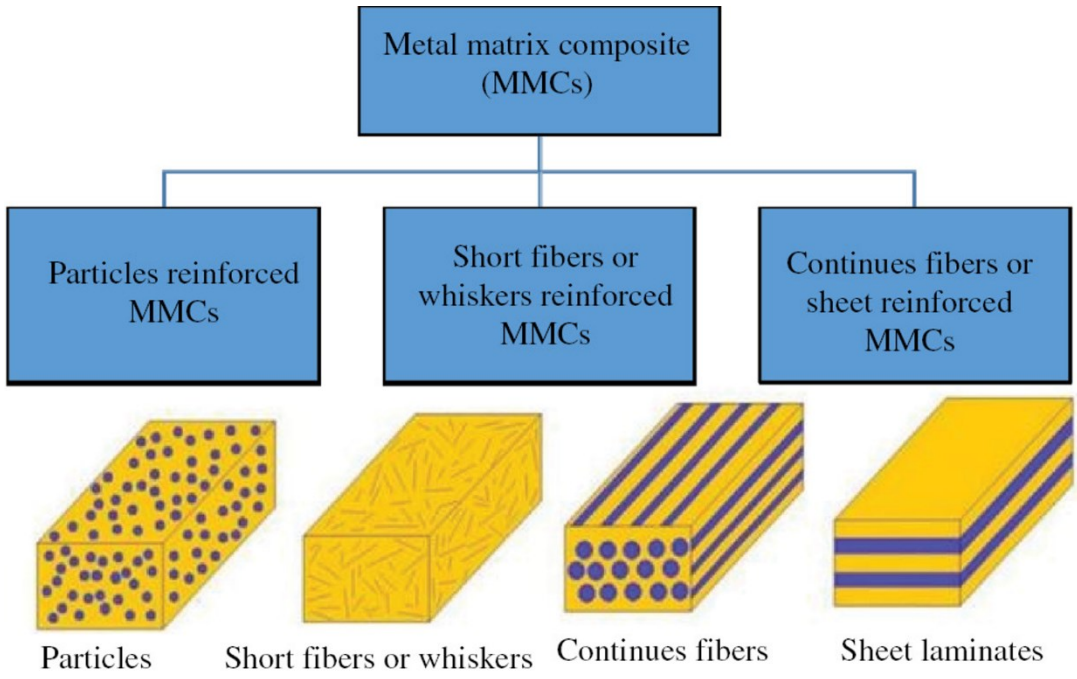

Figure 2: Representation of four common types of metal matrix composites. [103]

3.1 Historical Applications of MMCs

Although modern materials science has seen a sharp rise in interest, development of metal matrix composites is a well-established practice that has been ongoing for decades. Applications can be found dating at least back to the 1960s, at which time the desperate need for increased performance without excessive weights drove the aerospace industry to explore aluminum alloys enhanced by boron- and graphite-filaments [104]. These B/Al materials were eventually utilized as tubular struts in the fuselage and landing gear drag link of the Space Shuttle Orbiter, achieving the necessary mechanical properties with a 45% decrease in weight compared to the baseline aluminum. Meanwhile, the graphite/Al

composites were found to offer an excellent combination of high stiffness, low coefficient of thermal expansion, and high electrical conductivity, making them an ideal candidate for fabrication of the high-gain antenna boom for the Hubble Space Telescope. Although these applications could be considered as great successes of the technology, they were only practically achievable because of the capability of the specific projects to prioritize performance over cost, and the extreme costs and processing times associated with the diffusion-bonding methods utilized to make these MMCs essentially restricted the technology to government-backed projects (esp. aerospace and military) in the early stages of development. As academic research began to provide pathways for improved affordability though, opportunities for improved wear resistance, high structural efficiency, and improved thermal/electrical properties drew the attention of a larger crowd. By the 1990s MMC technology had gained ground in a variety of commercial sectors for applications such as ground transportation, manufacturing, and infrastructure [105].

In the modern day, MMCs could be considered to have evolved from a niche alternative to a commonplace commodity. Discontinuously reinforced aluminums are utilized in a wide variety of automotive parts, including reinforced pistons and cylinder bores for engines, intake and exhaust valves, driveshafts, brake components, and power module components [106]. Materials such as SiC-reinforced aluminums are widely utilized in thermal management applications for satellites and telecommunication systems [107]. Fe, Ni, and Co industrial tools are also widely integrated with assortments of carbides, cermets, and diamonds to improve hardness and wear resistance. Along with these universal applications, noteworthy progress has been made in the development and implementation of steels and other metals with enhanced properties from the dispersion of nano-ceramics specifically for application in nuclear power environments, which will be the topic of the following section.

3.2 MMC Enhancements in Nuclear Applications

Within the materials research field for advanced nuclear applications, a number of MMCs have been under development for several decades with the express purpose of enhancing material survivability. Chief among these has historically been oxide dispersion

strengthened (ODS) steels, a class of ferritic/martensitic steels in which oxide particles, especially Y_2O_3, are introduced by mechanical alloying to pin grain boundaries and act as dislocation barriers to increase mechanical properties at elevated temperatures [108]. This concept has gained much popularity for the purpose of raising the upper limits of the temperature operability window for steel materials and has seen considerable application both for 7-9Cr RAFM steels and 12-20Cr ferritic steels, such as displayed in Figure 3 [109], with the ODS iterations of the latter commonly being referred to as nanostructured ferritic alloys (NFAs). For ODS-EUROFER97 RAFM steel, inclusion of 0.3% Y_2O_3 has been demonstrated to retain yield strength over 200 MPa up to 700℃ with yield stress around 5%, though with the cost of increasing the DBTT from -90℃ up to 100℃ [110]. For NFAs following a similar approach, even more impressive tensile, creep and fatigue strength properties have been achieved up to at least 800℃, with reports suggesting service capabilities of nearly 40,000h at this temperature under stresses around 100 MPa [111]. Creep resistance has also been shown to be further increased with the addition of a small amount of Ti, which will favor the precipitate phase and further decrease the size of the oxide nanoparticles [112]. Of equal or even greater importance, NFAs have demonstrated excellent radiation and helium resistance, which can largely be attributed to the high sink density with the nano-scale precipitates, which helps to augment rates of vacancy-interstitial recombination while also introducing pinning points to restrict helium migration and prevent coalescence [113].

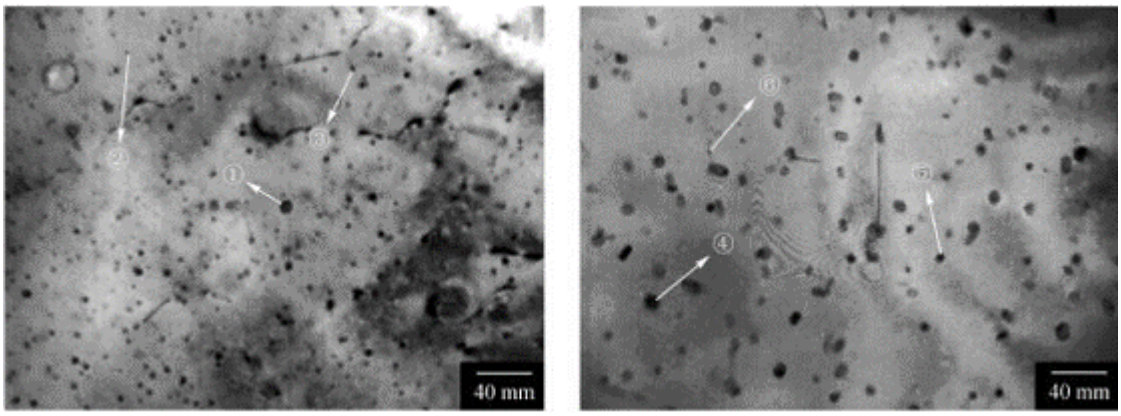

Figure 3: TEM images of ODS 18Cr-steel showing oxide particles.[109]

Although they feature many notable improvements, ODS steels still do not appear to be well-suited for ARC vacuum vessel candidacy yet. The mechanical properties at the target temperature may still be too low, and they are currently produced by costly, inconsistent powder manufacturing methods with poor scalability. However, this concept is not intrinsically limited to steels, and one might expect other combinations of MMCs to offer similar benefits. In fact, previous work out of the Ju Li group at MIT demonstrated a similar sink effect with the dispersion of carbon nanotubes into aluminum materials, reducing radiation damage and controlling the growth of helium bubbles in ion implantation experiments, as shown in Figure 4 [114]. It seems reasonable to infer that increased sink density and an associated improvement in neutron irradiation survivability are inherent byproducts of the introduction of well-dispersed precipitates when producing MMCs using nano-scale reinforcements. In this case, exploration of MMCs for nuclear applications should certainly not be limited to ODS steels. There may be significant merit to pursuing new combinations of nickel superalloy MMCs and selecting ceramic reinforcements with the primary goal of maximizing high-temperature properties.

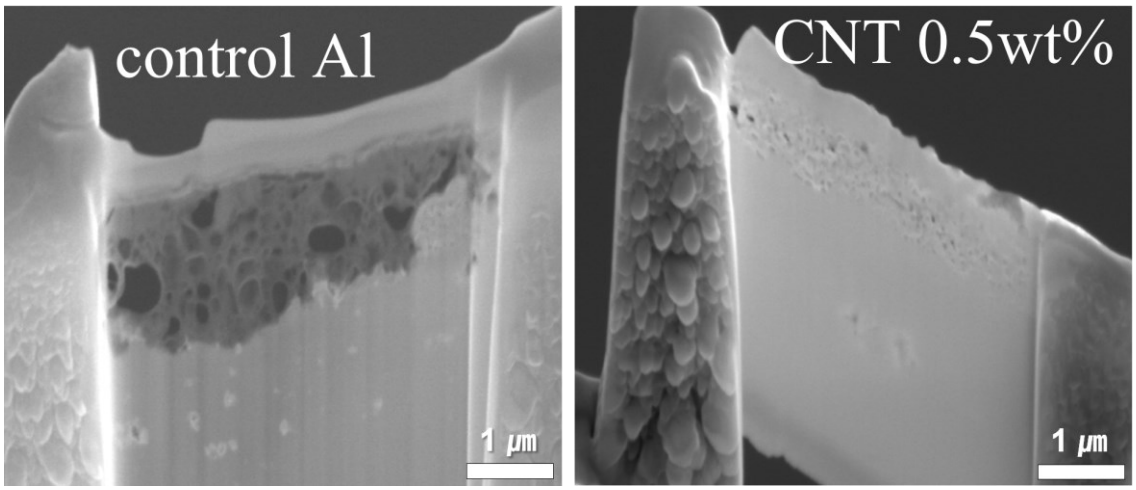

Figure 4: TEM images displaying decreased He bubble growth for Al alloy with CNT reinforcement following ion implantation. [114]

3.3 AM-Enabled Technology Expansion

MMC materials are a well-established technology, and they have been shown to offer remarkable benefits, achieving mechanical properties that surpass the typical strength/density tradeoff for metals, offering tunability of thermal and electrical conductivities, and even promoting improved resistance to neutron-induced degradation in nuclear applications. The simplicity of the concept, requiring only addition of small quantities of ceramics to the metal base alloy, would also appear to be very widely applicable. One might assume that there is potential to achieve improved properties by implementing MMCs in nearly any current applications of metals, especially in cases where strength or hardness are prioritized over toughness. However, through the years commercial growth of the technology has been hindered by the extreme difficulty of fabrication, which has been limited to powder metallurgy methods (typically sintering or hot isostatic pressing), infiltration methods, or stir casting techniques [115]. These fabrication strategies are slow, costly, and each present a unique myriad of other difficulties. While casting techniques are the most affordable and scalable, poor wetting of the ceramics results in nonuniform distribution of particles throughout the melt pools. Powder metallurgy allows for good distribution and part quality, but these techniques require expensive dies and are limited to small-scale production with simple geometries. As a result of these challenges, applications have been historically restricted to components that are small, high-value, geometrically simple, and which can be produced with a limited number of well-understood and highly processable base metals, namely Fe, Cu, Mg, and especially Al. Nickel superalloys, which are notoriously difficult to produce and machine, are considered essentially incompatible with these traditional MMC production techniques.

In recent years however, the rise in technological maturity and commercial availability of additive manufacturing[1] (AM) techniques has introduced new potential for MMC production that is expected to greatly expand the current catalogs of usable materials and geometries. Powder bed fusion (PBF) 3D-printing in particular offers unique advantages for this field of study by combining the benefits of previous powder metallurgy methods

[1] Note: The terms additive manufacturing and 3D printing are considered equivalent and will be used interchangeably in this thesis.

with much needed improvements in process flow, scalability, and geometric complexity [116]. This strategy, presented schematically in Figure 5 [117], follows a recurrent two-step approach in which powder from a reservoir or hopper is spread across the build area at a specified layer thickness, then selectively melted by a laser or electron beam following a CAD diagram sliced at the same thickness to progressively build a solidified part in the desired shape [118]. Fabrication in this way is inherently localized due to the extreme speed of melting and solidification involved from laser and electron beam processing, which enables isotropic distribution of reinforcing ceramics to be maintained at any size-scale. If heat distribution through the part can be adequately accounted for, scaling PBF part fabrication to large sizes essentially only requires proportional scaling of time and accessible build volume [119]. This technique has also been thoroughly researched and has achieved remarkable success in near net-shape fabrication for several especially difficult to machine metals, such as titanium [120], and, importantly, nickel superalloys such as Inconel 718 [121].

With AM as an enabling technology, academic research into the production and testing of new MMC combinations, including those based on nickel superalloys, has gained great ground in the late 2010s and early 2020s. During this time, Ti-carbides and -borides have especially received considerable attention as early-stage nickel-based MMC reinforcements. For example, in 2019 Gu et al [122] produced an Inconel 718 reinforced with 10 wt% TiC by laser powder bed fusion (LPBF) and achieved an 18% increase in hardness. Similarly, in 2022 Mandal et al [123] produced Inconel 718 composites with varying concentrations of TiC (0, 10, 20, and 30 wt%) and found capability to tune the hardness up to an increase of 78% over the unreinforced metal. Yao et al [124] also observed notable increases in Inconel 718 yield (σ_y, 774 versus 647 MPa) and tensile (σ_{UTS}, 1029 versus 940 MPa) strengths after printing, though properties were found to worsen after the standard heat treatment to produce γ’ and γ” precipitates. With regards to borides, in 2021 Zhang et al produced 2 wt% TiB_2 reinforced Hastelloy X superalloy and reported increases of 43% in hardness, 51% in high-temperature hardness, and 28% in yield strength [125]. In 2022, the same team then applied the 2 wt% TiB_2 reinforcement to a Haynes 230 alloy (a much lower strength nickel superalloy designed for higher temperature operation) and demonstrated a remarkable increase in ductility at 850˚C [126].

These studies suggest some of the excellent enhancements that may be achieved through incorporation of ceramic reinforcements in nickel superalloys through AM, but the results are still relatively new and limited in scope, and they may only begin to scratch the surface. In order to maximize the potential of superalloy MMCs and achieve the best possible operation lifetime for a near-term ARC vacuum vessel, part of the goal of this thesis is to explore the capabilities of new ceramic reinforcements with the goal of obtaining the best combination of strength and ductility for high-temperature performance, especially with the high strength base materials such as Inconel 718. Efforts towards this goal will be addressed in the following chapters.

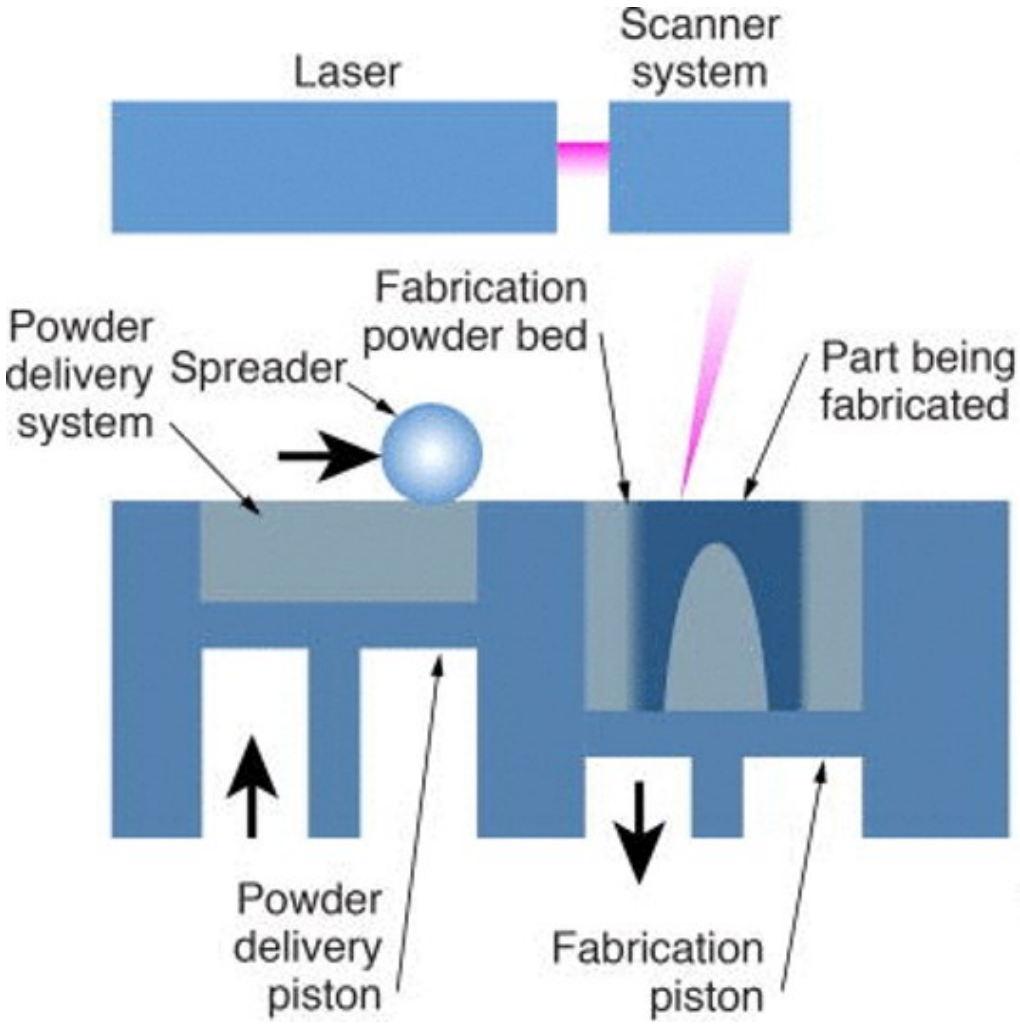

Figure 5: Schematic representation of LPBF system.

Chapter 4

Initial Comparison of Nano-Ceramics in Aluminum

In the preliminary stages of the research discussed in this thesis, the exploration of new FCC composites was determined to have significant merit, though the particular focus on extreme environment applications that would lend focus towards materials such as nickel-superalloys had not yet developed. With the goal of exploring the effects on room temperature mechanical properties of several combinations to identify particularly promising nano-ceramics, AlSi10Mg was selected as the initial base FCC matrix. This aluminum alloy, which features high corrosion resistance, high mechanical strength, and low density, was predicted to offer high value for industrial utilization if significant property improvements could be achieved. More importantly, AlSi10Mg is characterized by high processability and low melting temperature and has been well studied for additive manufacturing applications [127]. This combination allowed for a two-sided approach in which lab-scale stir casting could enable rapid production of miniature tensile samples at MIT while collaborators could perform simple single layer laser test prints to compare hardness effects. In this way, testing could be performed with minimal powder production, a major time-consuming step for each MMC of interest, and requirements for 3D printing time could be minimized, which was necessary due to limited printer access at the time of these experiments. This chapter will include a description of the experimental methods

utilized in this phase of work, followed by a discussion of key results and conclusions which prompted further studies.

4.1 Production and Testing Methods for Al-Composites

To provide an adequate comparison over a range of options, seven materials were prepared, including an AlSi10Mg control sample and separate composites of AlSi10Mg with carbon nanotubes (CNT), SiC, Al_2O_3, TiO_2, TiCN, and boron nitride nanotubes (BNNT) as nano-reinforcements. These nanomaterials, tend to agglomerate into clusters in storage due to the electrostatic interactions, such as Van Der Waals forces, which can prevent good dispersion during the alloying process, especially for those featuring tube or wire geometries with high-aspect ratios that are prone to entanglement. Therefore, the initial phase of powder production was a declustering process. Selected nano-fillers were individually combined with AlSi10Mg powder at a concentration of 10 vol% and placed into a high-speed, multi-blade blender. The unmixed material was then subjected to high power blending at a blade rotation rate of 15,000-30,000 rpm for two minutes. This process was repeated ten times for each sample, allowing eight minutes of inactivity between each step of blending for the dispersion of accumulated heat. Upon completion, the added nanomaterials, including tubes and wires, were observed to have well disentangled and achieved good dispersion throughout the matrix powder.

Following declustering, the disentangled 10 vol% powders were transferred to a planetary ball mill and combined with additional AlSi10Mg powder, bringing the total ceramic concentration to 2 vol%. Using zirconia balls as milling media, powders were subjected to 30 minutes of total milling time, distributed over multiple shorter runs with breaks for dissipation of heat buildup. This milling process enables a mechanical alloying effect between the ceramics and AlSi10Mg powder through consistent impact and shear force, promoting intergranular encapsulation of the nanomaterials to maintain dispersion as well as possible during casting and printing processes and prevent anisotropy. This is a well-established and commonly utilized method of preparing MMCs for powder-based fabrication methods [128]. Both the declustering and the milling phases were performed under inert argon gas to minimize accumulation of contaminant oxides and nitrides.

Once milled, powders were divided into two batches for separate casting and printing processes. For the casting batch, additional un-milled AlSi10Mg was added to help promote melting in case of unmitigated oxide formation during the milling process, bringing the total concentration of ceramics down to 1 vol%. Mixtures were added to a graphite crucible and heated up to 800°C in a furnace under argon, and a mechanical stirrer was utilized at 1300rpm, which helped to break down milled particle surfaces to enable melting while also ensuring that any separated ceramics remained well-distributed. Once fully liquid, the mixtures were quickly poured out of the crucible onto a room-temperature steel plate and were observed to solidify in the span of seconds, forming small, amorphous billets. This procedure, portrayed in Figure 6, proved successful for the majority of the nanocomposites. However, the sample prepared using the TiO2 nano-filler was observed to leave behind a significant amount of fine, unmelted particles, likely indicating separation of the TiO2 from the metal matrix due to poor wettability during melting.

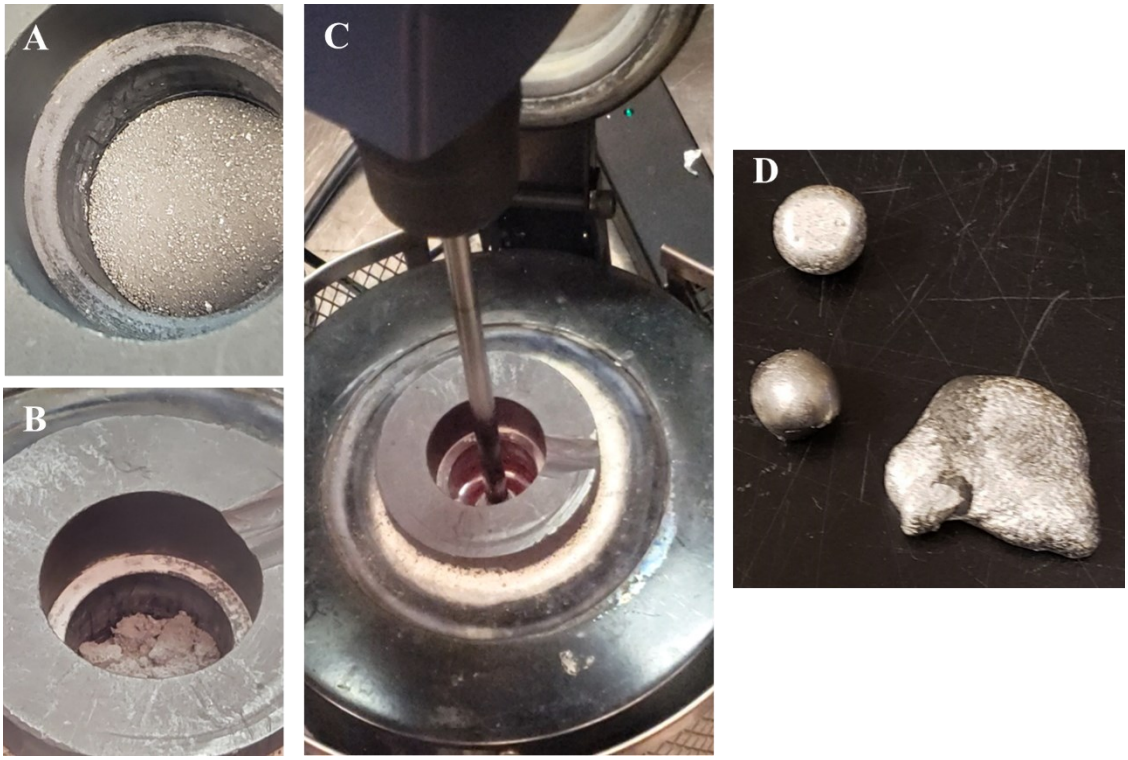

Figure 6: A) Post-milling mixture of CNT in AlSi10Mg. B) Partially melted powder at 800C. C) Mechanical stirring to achieve uniform melt pool. D) Cast pieces of AlSi10Mg-CNT composite.

Next, pieces of the cast composite material were gradually raised to 400°C and extruded through a 2 mm diameter nozzle to form rods. These rods were subjected to several rounds

of cold rolling to produce nanocomposite foils approximately 100 µm thick. Finally, these foils were stamped into dogbone shapes to form miniature tensile specimens, annealed at 400°C for seven hours, and tested to failure at elongation rates of 1 mm/min. The final stages of this specimen preparation process are displayed in Figure 7 below.

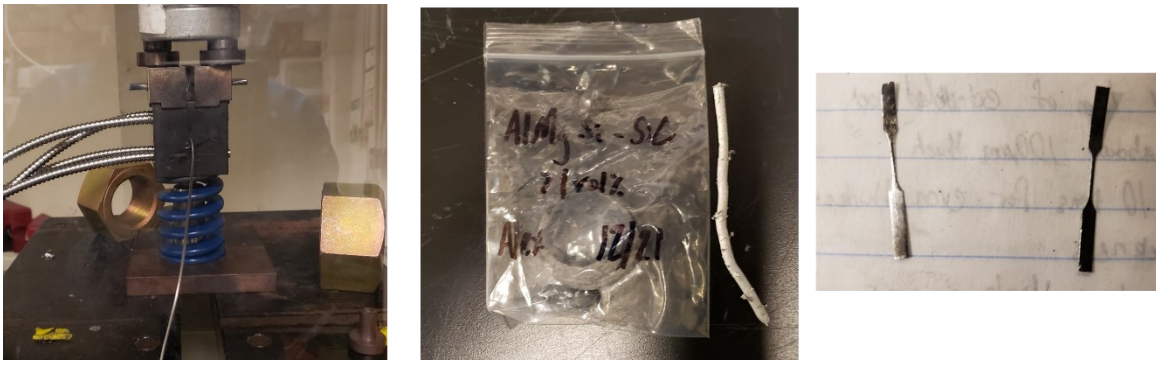

Figure 7: Extrusion process, extruded composite rod, and cold rolled and stamped tensile specimens for Al-based MMCs.

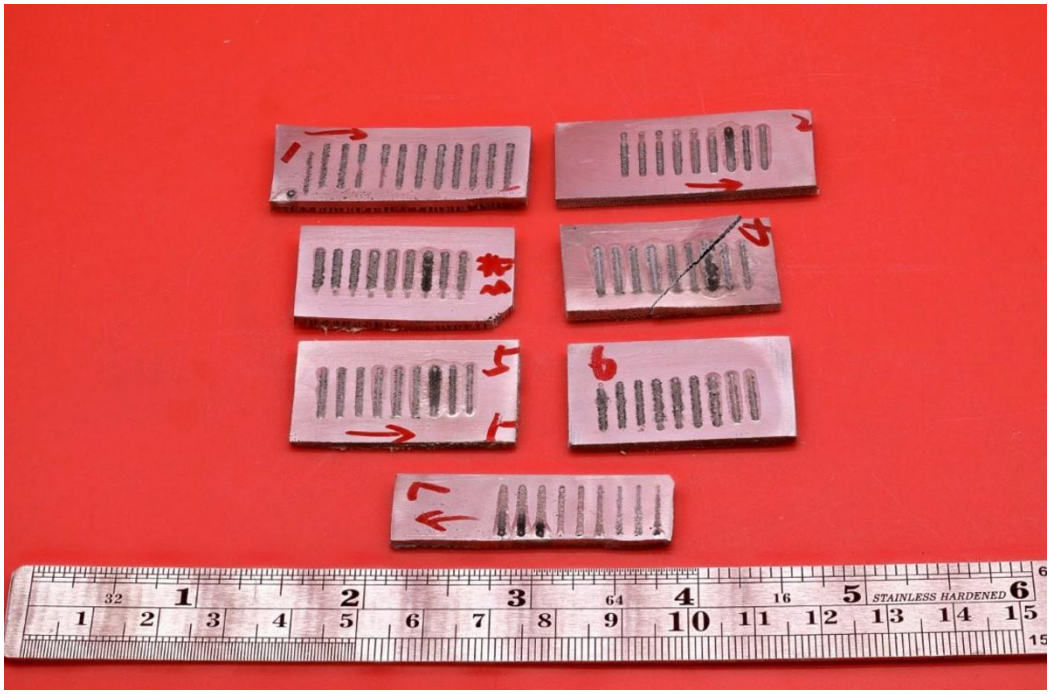

Figure 8: Single layer tricks of composite AlSi10Mg materials printed by DED

For the milled powder batches set aside for printing, sieving was first performed at 100 µm to remove large and irregularly shaped particles that formed during the mechanical alloying process. This step serves to ensure spreadability and blowability of the composite

powder. Powder was then delivered to collaborators from the Wen Chen group at UMass Amherst. Using pure AlSi10Mg, they prepared small substrate rods. An OPTOMEC directed energy deposition laser printer was then utilized to add single layers of composite materials to the surface of the substrates, as shown in Figure 8. Hardness testing could then be performed to analyze the contributions of the various ceramics.

4.2 Results of Mechanical Testing for Al-Composites

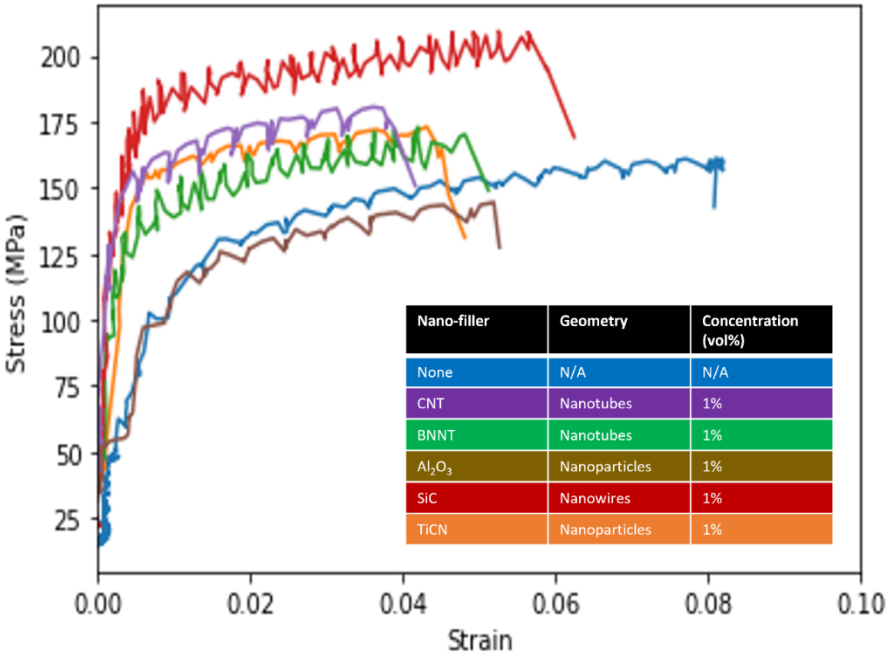

Figure 9: Average tensile results for AlSi10Mg-MMC foils

Table 1: Microhardness of DED single layer AlSi10Mg MMCs

Materials	*Microhardness, Hv*
AlSi10Mg (pure)	75.44 ± 3.6
AlSi10Mg (ball-milled)	73.36 ± 2.0
AlSi10Mg+BNNT	73.64 ± 3.2
AlSi10Mg +SiC	101.26 ± 2.7
AlSi10Mg +TiC	79.37 ± 2.3
AlSi10Mg +Al2O3	75.1 ± 4.6
AlSi10Mg +TiO2	83.76 ± 6.2

Tensile results for stir-cast AlSi10Mg nanocomposite foils are presented in Figure 9 as the average of three repetitions for each composite, except TiO_2, which could not be properly cast. Small fluctuations in stress were observed with strain development in each test, similar to results that may be observed with the onset of dynamic strain aging. This effect was attributed to the use of especially small foil samples, which likely experienced evolution of plastic deformation too quickly for high precision measurements in a test frame and 2D digital image correlation system originally intended for larger samples. Regardless, overall trends in the stress/strain evolution were apparent from the data and generally consistent across repetitions. Addition of nanoceramics was found to result in loss of ductility in all cases. This result was expected, as the introduction of precipitate impurities likely restricted grain growth during casting and recrystallization processes and restricted dislocation motion in plastic deformation. This process also resulted in an increased Young's modulus and improvements in both yield and ultimate tensile strength for almost all reinforced composites over the control alloy. CNT-reinforced samples were found to be the exception, achieving no increase in stiffness or strength but still experiencing a similar loss in ductility to the other samples. This was a surprising finding and not in line with the positive results achieved with CNT-reinforced aluminum alloys reported in past studies [129]. It may have been indicative of poor distribution of CNTs during the casting process, resulting in anisotropic components that did not receive the benefits of ceramic implantation but remained more prone to crack initiation and premature failure. Of the composite materials that were observed to increase in strength, the SiC reinforced materials were consistently found to achieve both the highest increase in strength and the lowest loss of ductility, maintaining toughness on par with or exceeding that of the unreinforced AlSi10Mg.

Microhardness examination of the single layer composites prepared via DED, as displayed in

Table 1, demonstrated similar superiority of the SiC reinforcement. While most ceramics achieved little change in measured hardness, AlSi10Mg materials with small addition of SiC (2 vol% for the single-track DED samples) achieved an increase of over 30% on average. It is also worth noting that, despite poor wetting resulting in a removal of the TiO_2 MMC materials from testing during the stir-cast sample exploration, the 3D

printing process flow enabled inclusion of these materials, which were found to achieve the second highest microhardness results with an increase of approximately 10% over the pure metal. This example demonstrates part of the power of AM as an enabling technology to produce new MMC combinations that might have been impossible to achieve in the past.

4.3 Conclusions from Rapid Exploration of Al-MMCs

Overall, SiC nanowires stood out from results of both testing processes as a ceramic of special interest that should be investigated further. While increases in strength may offer high value to certain material applications, retention of at least some degree of ductility and toughness is essential for load-bearing structural applications, especially when considering high-temperature applications. The AlSi10Mg+SiC was found to offer both the highest increases in strength and hardness as well as the best retention of ductility, making it the ideal choice.

At this time, it is noted that the reliability of these testing methods, which were selected with a primary focus on rapid ceramic down-selection, is unclear. Though the results for SiC were extremely promising, the remaining composites which did not perform as well as SiC, especially the CNT materials, certainly merit further study and may be expected to offer improved property enhancement with further optimization in fabrication methods and testing at larger scale. However, continuation of this work was disrupted by the onset of the global pandemic, following which I gained reliable access to LPBF technology and elected to shift focus to two major studies: 1) the production of nickel superalloy MMCs at the bulk scale for more in-depth testing with individual ceramic reinforcements, and 2) the development of new printing parameters for refractory alloys, both of which will be the focuses of the remainder of this thesis. Although the work and results described in this chapter may offer no definitive conclusions, they have been included in this thesis to provide context for the selection of SiC as a nanoceramic of interest, as well as to offer a starting point for future researchers expanding the FCC MMC library of materials.

Chapter 5

Ceramic Reinforcement of Inconel 718: SiC

As detailed in the thorough investigation presented in Chapter 2, Inconel 718 (In718) is a nickel superalloy that has been widely utilized in high-temperature and nuclear applications. 718 is a Ni-Fe-Cr superalloy which, following an appropriate heat treatment process, is strengthened by a combination of both γ' and γ" precipitates. This alloy is particularly favored among nickel superalloys for its combination of extreme yield strengths, high ductility, and good weldability. Decades of industrial utilization have also led to the development of high technological maturity and a robust supply chain for the material. These aspects make Inconel 718 an ideal candidate for construction of vacuum vessels in early ARC-class tokamaks if a pilot plant is required in the short term. However, low creep resistance at the target temperature and high likelihood of helium embrittlement are expected to limit the working lifetime of a 718 vacuum vessel, possibly leading to replacement being required in the span of months to a year of full power operation. Formation of metal matrix composites has been found to be a promising method for potential enhancement of material lifetime, producing nanoscale precipitates that increase sink number density to enhance resistance to the effects of neutrons, and augmenting mechanical properties with ceramics that are often stable to exceptionally high temperatures [108,130]. MMC production capabilities for nickel superalloys have been

historically limited due to incompatibility of the materials with the highly specialized fabrication methods traditionally required for ceramic incorporation. However, production of In718 and many other nickel superalloys has been well researched for AM, and high-quality components can be reliably fabricated with techniques such as LPBF and DED [131,132]. This opens a door for production of new MMCs using a superalloy base matrix. Importantly, production via AM may already be highly favorable for ARC vacuum vessels. The scalability and geometric flexibility of the process may enable minimization of required welds in the vessel, while the customizability of AM parts offers unique opportunities for design improvements with each vessel replacement.

To this point, exploration of Ni-based MMCs has been primarily limited to Ti-based ceramics [122,126]. To take full advantage of the newfound capabilities provided by AM and to seek to optimize properties to the highest degree possible for fusion and other extreme environment applications, there is currently a significant need to expand testing and explore new and promising superalloy reinforcement options. With excellent hardness and strength at elevated temperatures and good oxidation and thermal resistance [133,134], SiC is a promising candidate for MMC formation. Furthermore, its high temperature capabilities have already been demonstrated in SiC/SiC ceramic matrix composites [86], and the material was found to perform extremely well in the FCC MMC screening studies with aluminum described in Chapter 4. Even so, prior to this work the combination of In718 and SiC had not been explored to the best of my knowledge. In this chapter I present new research conducted as part of my PhD program and recently published in *Additive Manufacturing* [135] on the development and analysis of an In718 MMC reinforced with SiC nanowires through LPBF. The following sections will detail composite powder production techniques, post-printing composition analysis, and mechanical property testing at room and elevated temperatures to demonstrate the capabilities of this new In718+SiC system.

5.1 In718+SiC Composite Powder Production

For this study, gas atomized In718 powder with particle diameters 15-45 μm was purchased from MSE Supplies LLC to serve as the base metal matrix. For the reinforcing ceramics,

SiC nanowires of 99% purity were purchased from Sinet Advanced Materials Co. with wire lengths 50-100 μm and diameters 0.1-0.6 μm. SEM images of the In718 powders and SiC nanowires, which confirmed particle size distributions from suppliers, are displayed in Figure 10.

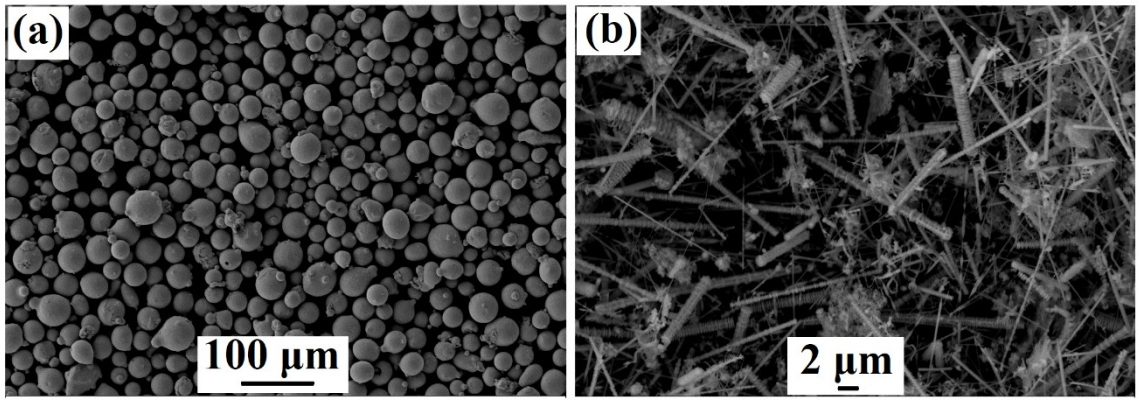

Figure 10: SEM images of as-purchased A) In718 and B) SiC powders utilized in MMC production.

SiC nanowires were combined with In718 powder to reach a concentration of 2 vol% and subjected to high-speed blender declustering for 90 minutes to disentangle and distribute individual nanowires. Blended In718+SiC powders were then ball milled for 30 minutes total milling time at 600 rpm to achieve mechanical alloying of the ceramics and metal bases. Milling was conducted in a Fritsch Pulverisette 7 planetary micro mill using stainless steel vials and 5 mm diameter stainless steel balls with a ball-to-powder weight ratio of 5:1. Ball milling parameters were carefully selected to preserve sphericity of the powder for spreadability under the recoater blade of an LPBF system, and 99.5% stearic acid was added to the milling vials at 2 wt% to act as a process control agent and prevent excessive powder clumping or welding to the vials [136]. Gas-tight milling vials (Fritsch) were used, and loading and unloading was conducted in a glovebox under inert argon atmosphere to minimize oxygen content during the milling process, when accumulation of impurities is most likely to occur. Following milling, composite powders were heated to 420°C under argon for 2 hours to promote removal of the stearic acid content prior to use. Powders were then sieved to remove irregular particles exceeding 100 μm diameters. SEM-EDX mapping on samples of the composite powder confirmed good sphericity, retention of average particle size < 40 μm, and good distribution SiC across the particles, and these

images are provided in Figure 11. TEM-EDX of a cross-section of single In718+SiC particle prepared by focused ion beam (FIB) is displayed in Figure 12 and reveals that the SiC has been continuously coated on the surface of the metal particles with a thickness of about 200-300 nm.

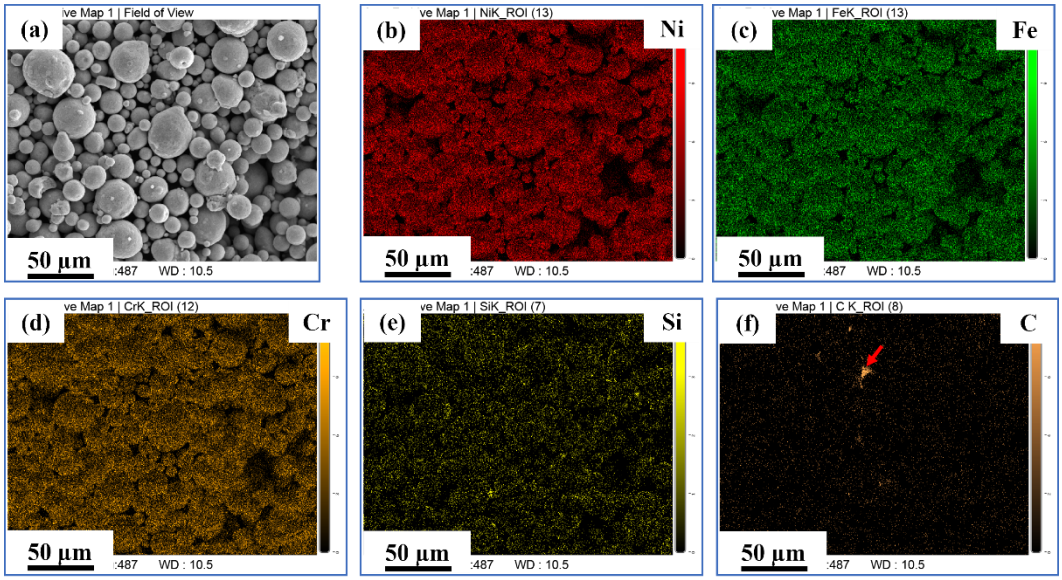

Figure 12: SEM and EDX mappings of ball-milled In718+SiC powders. The arrow in (F) indicates carbon tape used for mounting, not signal from powder.

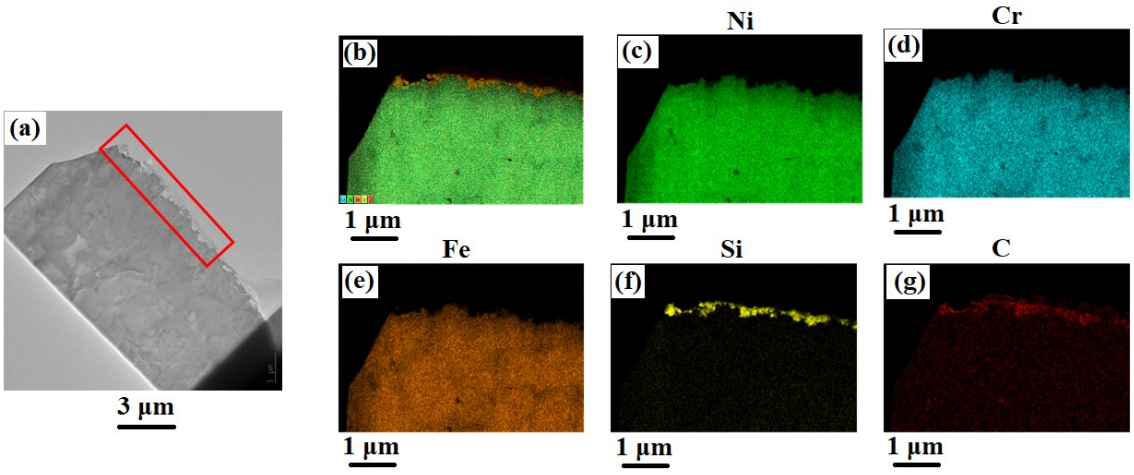

Figure 11: (A) TEM image, (B) composite EDX mapping, (C-G) individual element EDX results from an FIB'ed cross-section of a single ball-milled In718+SiC particle.

5.2 Sample Production by LPBF

Balled-milled In718+SiC powders were printed in an EOS M290 commercial LPBF system, as was unreinforced In718 in the as-purchased state to directly compare the effects of the ceramic reinforcement. Milled powders demonstrated excellent spreadability during printing with no noticeable differences introduced compared to as-received powders. Samples were produced to thicknesses of 2-3 mm, including rectangular geometries with side lengths of about 20 mm to produce tensile specimens and small squares with side lengths of about 4 mm for microstructural analysis. These samples were printed on 4140 steel plates using the EOS standard printing parameters for In718, provided in Table 2, which have been verified to produce high print quality in numerous studies [137–140].

Table 2: Printing Parameters for In718 in EOS M290

Laser Power (W)	285 W
Scanning Speed (mm/s)	960 mm/s
Layer Thickness (µm)	40 µm
Hatch Spacing (µm)	110 µm
Laser Spot Size (µm)	100 µm
Scan Rotation	67°
Volumetric Energy Density	67.47 J/mm^3
Build Plate Preheating Temperature	80°C
Shield Gas	Ar, 99.9%
Build Plate Material	4140 steel

Upon completion of printing, samples were removed from the build plates by wire electrical discharge machining (EDM). Several specimens from each batch, both reinforced In718+SiC and unreinforced In718, were subjected to an industry standard heat treatment for wrought In718 to form the strengthening γ'/γ" precipitates [141]. Selected specimens were heated to 1050°C in a tube furnace for 15 min, water cooled, aged at 720°C for 8 h, allowed to cool in the furnace, and then aged again at 620°C for 8 h and cooled in

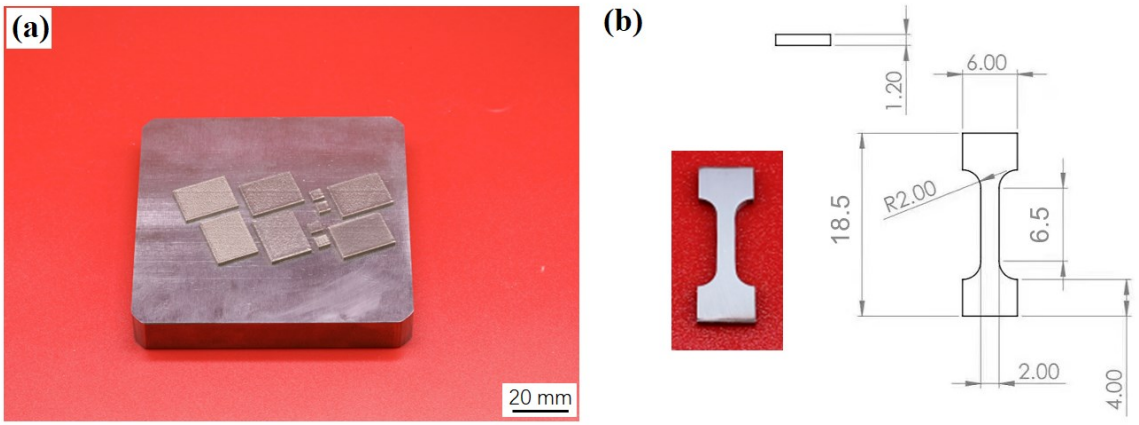

Figure 13: A) Samples fabricated by LPBF in an EOS M290 printer. B) Specimen dimensions (in mm) and example tensile specimen cut from rectangular prints by wire EDM.

air. Hereon, these heat-treated samples will be differentiated from non-treated samples by the inclusion of *HT* in the naming convention. Finally, tensile specimens were cut by EDM from the large rectangular prints perpendicular to the build directions for each of the now four groupings (In718, In718 HT, In718+SiC, In718+SiC HT). Figure 13 provides an example image of printed specimens still attached to the build plate, along with the dimension specifications for the dogbone samples produced for tensile testing.

5.3 Cross-Sectional Analysis of Printed Samples

Following heat-treatment, X-ray diffraction (XRD) patterns were obtained from the four sets of samples at 35 kV and 40 mA using Cu-K_α (λ=1.5406 Å) radiation at a 2θ range of 10-90° at 2°/min in order to evaluate the evolution of phases. These XRD patterns, displayed in Figure 14a, display the typical FCC γ matrix phase in all samples, with and without SiC. Samples with SiC reinforcement also displayed minor signals of Nb- and Ti-carbides, which were not observed in the unreinforced samples. Nb and Ti, included in In718 as minor alloying elements at 4.8 and 0.9 wt% respectively, each have high affinities for bonding with C. These XRD results would appear to suggest the occurrence of an exchange reaction, likely during the high-energetic melting/solidification stages during printing, in which dissolution of the SiC occurred and the free C atoms preferentially formed the observed (Nb, Ti)-carbide phases. Due to overlap with the γ-phase signals,

XRD peaks were insufficient to confirm the formation of γ'/γ" precipitates [137], so these were confirmed via EDX mapping of sample cross-sections, provided in Figure 14b-k. Regions denoted with yellow arrows in these images were rod-like phases with lengths on the order of 10 nm, which were found to contain higher concentrations of Ni, Nb, Ti, and

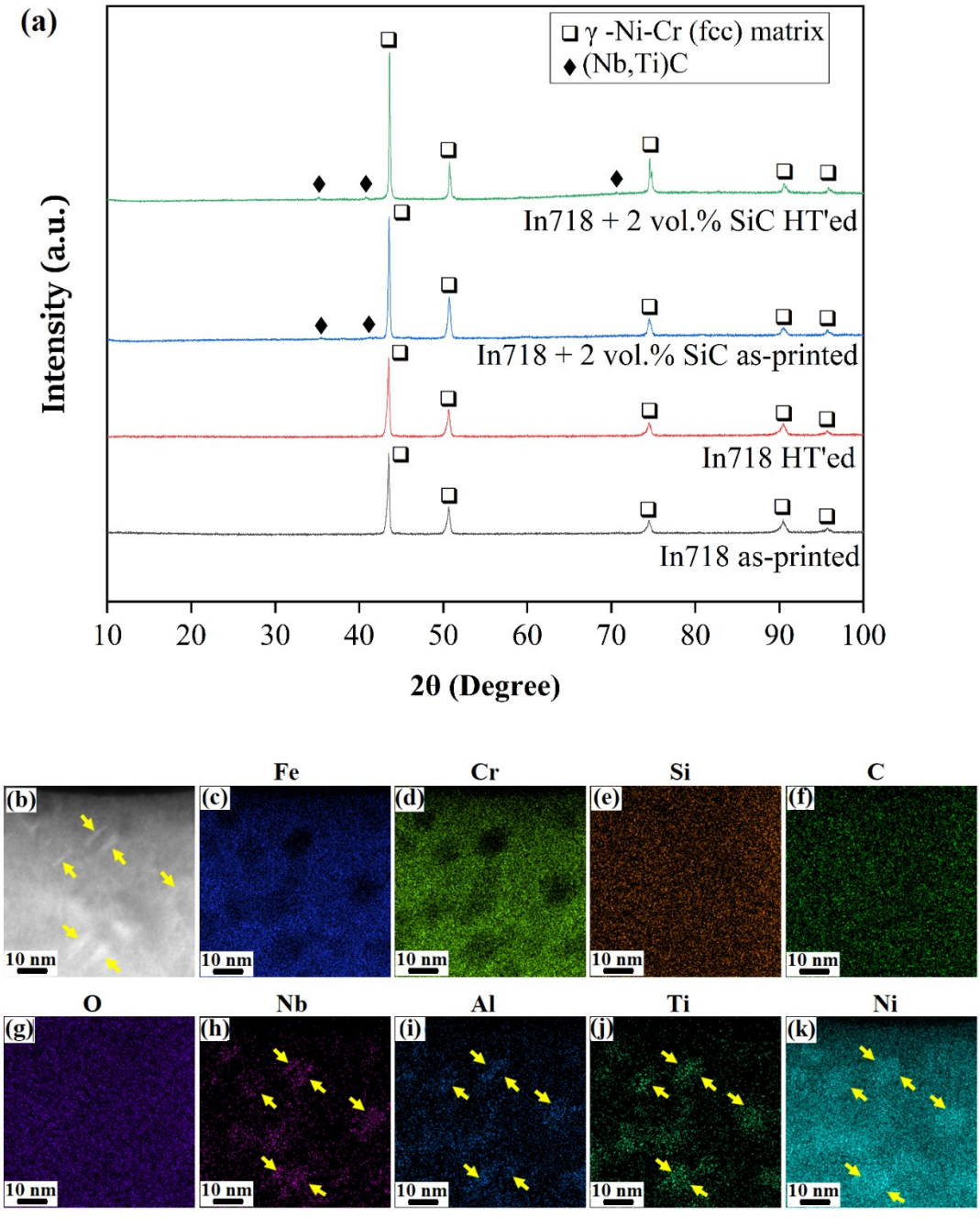

Figure 14: A) XRD analysis of printed samples. B-K) STEM-EDX mappings obtained from In718+SiC HT sample, revealing the formation of precipitates within the matrix.

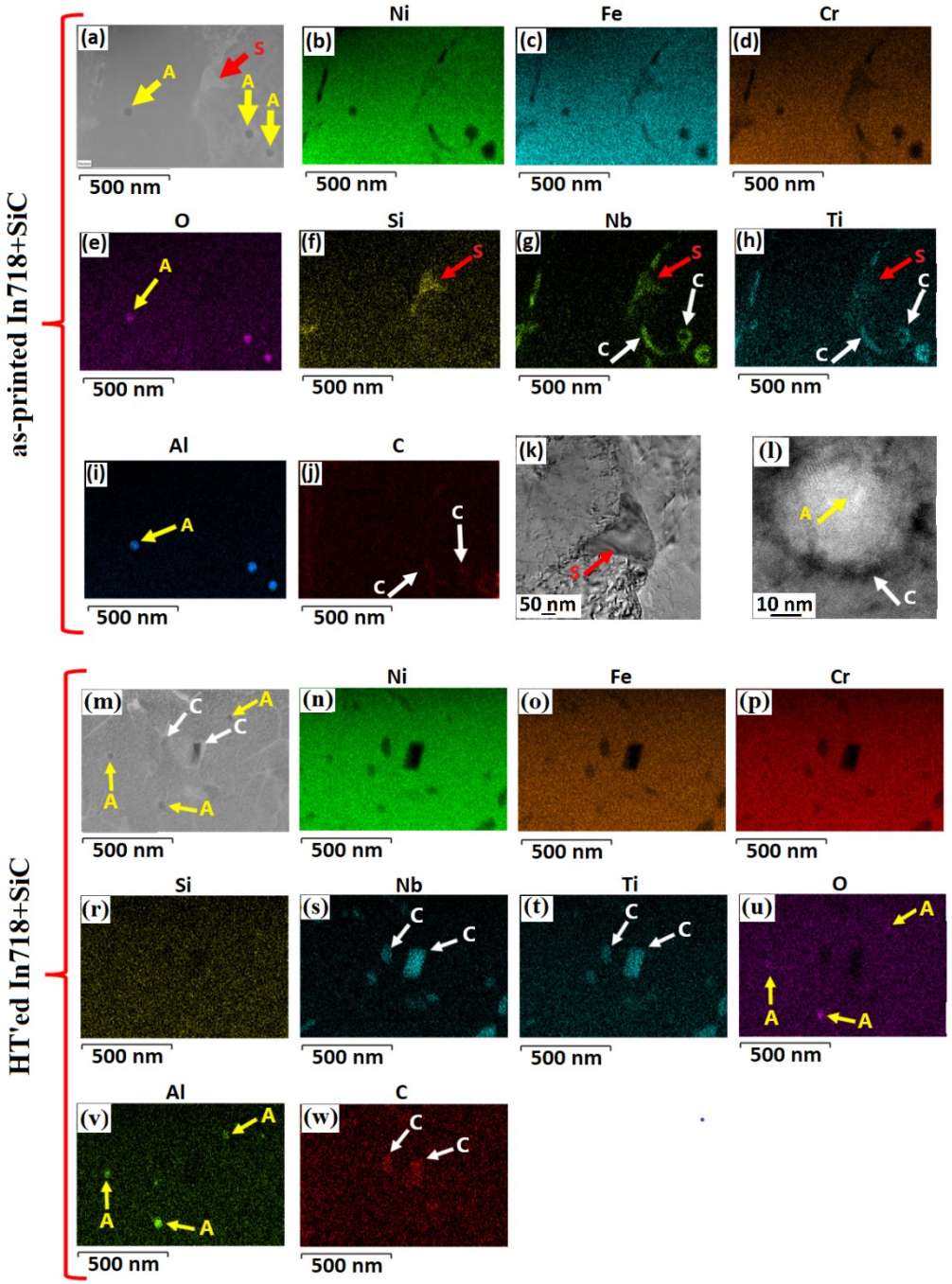

Figure 15: STEM-EDX mappings obtained from In718+SiC and In718+SiC HT.

Al elements and depleted concentrations of Fe and Cr. Both the geometries and elemental make-ups of these regions meet expectations for γ'/γ" precipitates, though it is noted that this method is insufficient to differentiate these phases due to their similar compositions [142].

Further STEM-EDX mapping at a larger scale, presented in Figure 15, provided a clearer picture of the behavior of the nanomaterials during the printing process. First, nanoparticulate Al_2O_3 inclusions about 50 nm in diameter, indicated by the letter A, were identified throughout the microstructure, most likely as a result of Al alloying elements reacting with trace oxygen remaining in the build chamber during printing. Surrounding these Al_2O_3 particles in the as-printed samples were strong overlapping signals of Nb, Ti, and C in a spiral morphology, indexed with the letter C, confirming the presence of the (Nb, Ti)-carbides suggested by XRD. After heat-treatment, these carbides were observed to take on particle-like morphologies instead of the previous spirals, with average lengths of approximately 90 nm. On a comparable size scale, additional phase regions were observed with strong signals for Nb, Ti and Si, indicative of (Nb, Ti)-silicides, which are commonly formed in the presence of free Si particles in the superalloy microstructure [143], and these are indexed with the letter S.

Evidently, the large energy depositions associated with rapid laser melting and solidification resulted in the near complete dissolution of the original SiC nanowires, which were not observed in imaging processes following printing. Instead, the broken down SiC ceramics appeared to have provided the building blocks for formation of new Nb- and Ti- (and some Mo-) silicides and carbides. Though not the original expectation, these in-situ formed silicides and carbides still acted as secondary phase ceramic precipitates and were expected to play a similar role to that predicted of the SiC, e.g., increasing strength and reducing grain growth. These particles might even be expected to perform better than the original geometry due to their further reduced size scale, which potentially allowed for even better precipitate distribution throughout the matrix. EBSD analysis of the printed sample cross-sections, presented in Figure 16, confirmed some effect of these particles on grain size. As-printed samples of both In718 and In718+SiC displayed the long columnar grains typical of laser printing techniques. However, average grain size was found to have slightly decreased with the addition of the SiC. Due to the occurrence of some recrystallization, heat-treated samples have transitioned incompletely from columnar grains to a more equiaxed structure, and once again the average grain size was found to decrease slightly. Grain size distributions were quantitatively measured based on these EBSD results with example cross-sections, which confirmed a slight decrease in size for

SiC-reinforced samples, especially parallel to the build orientation. Grain orientation data collected from these measurements also revealed a slight increase in the fraction of high-angle grain boundaries for composite materials. Low-angle (0-5°) boundaries are the major features of as-printed In718 due to the formation of high dislocation densities from thermal stresses during printing [144,145]. Increased high-angle boundaries might therefore be an indication of some relief in thermal stress, possibly due to an increase in thermal conductivity in the reinforced materials improving heat dissipation. Such an effect has been suggested in previous studies, such as by Gu et al [146], who demonstrated that TiC nanoparticles accelerate heat dissipation of the In718 molten pool during the LPBF process. Grain size and misorientation angle data are presented in Figure 17.

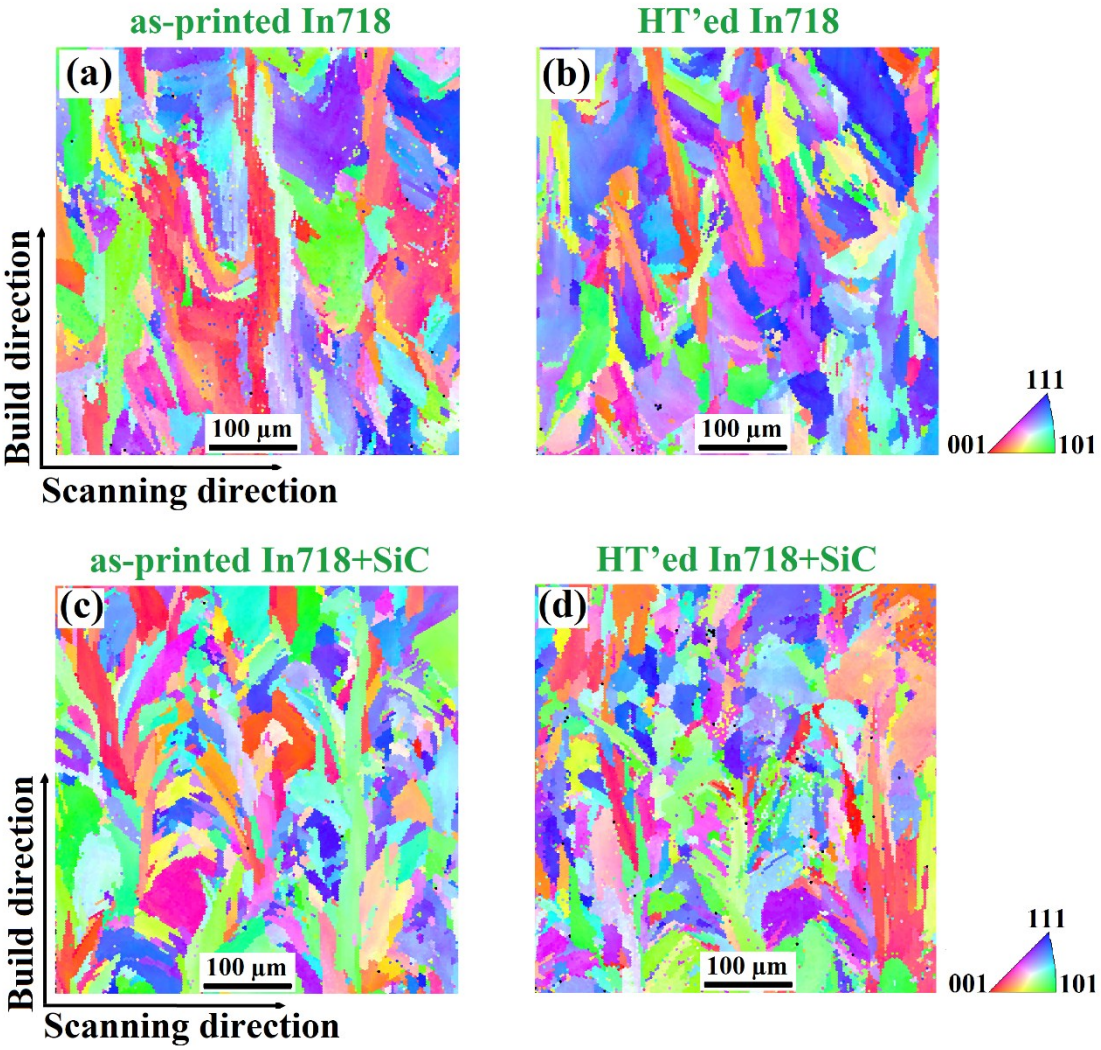

Figure 16: EBSD analysis for printed samples, cut along the build direction.

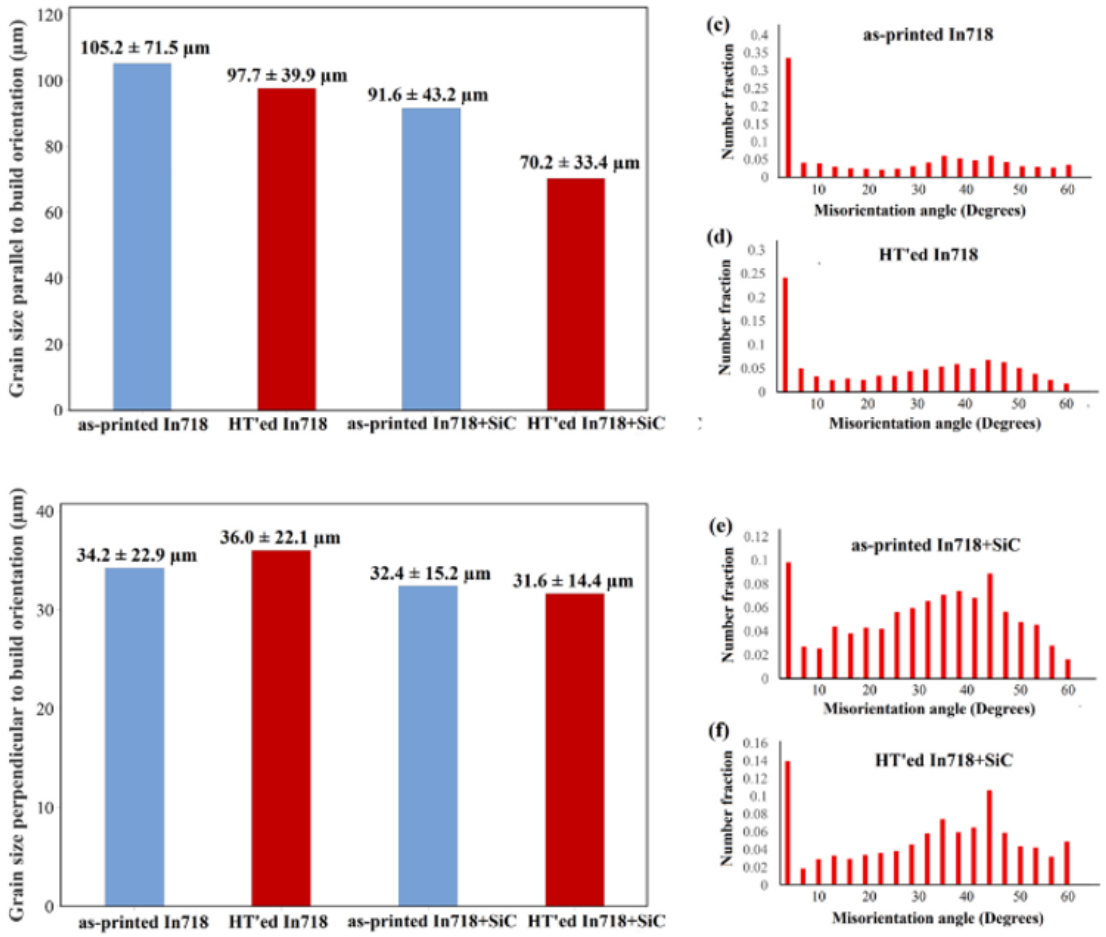

Figure 17: Grain size and misorientation angle distributions for printed samples.

Other effects of ceramic implantation were observed in secondary electron SEM imaging of the cross-section microstructures, shown in Figure 18. Notably, reinforced In718+SiC composites were found to have higher densities, with fewer spherical or irregularly shaped pores and fewer cracks than the unreinforced In718 samples. This observation was confirmed by measurement of densities using the Archimedes method, which provided densities of 8.19 g/cm^3 and 8.12 g/cm^3 for In718 and In718+SiC respectively. Using theoretical densities of 8.22 g/cm^3 for In718 [147,148] and 3.21 g/cm^3 for SiC [149,150] to calculate theoretical densities, this equates to relative densities of 99.6% for In718 and 99.9% for In718+SiC. The formation of cracks and pores is a known issue during 3D printing techniques, and failure to achieve 100% densification is one of the technological shortcomings that has limited the adoption of printed components in the early days of AM technology. In some cases, this has even been shown to be a greater risk

in the production of composites. In an older attempt at the production of Ni-based MMCs from 2013, Cooper et al actually rejected SiC as a viable candidate for In625 reinforcement due to excessive crack formation during printing [151]. Improvement in the feasibility of implementing SiC reinforcement can certainly be linked to improvements in understanding of laser melting processes and precision of AM technology, (e.g., the study by Cooper reported use of an 850 µm laser spot size compared to 100 µm used here). Use of nanomaterials and the activation of the exchange reactions breaking SiC into (Nb, Ti)-carbides as described also likely aided integration into the matrix. Regardless, when considering the excessive cracking of previous studies as the frame of reference, reinforcement without significant increase in cracking would have been considered a success, and the actual decrease in printing defects observed in this study was excellent.

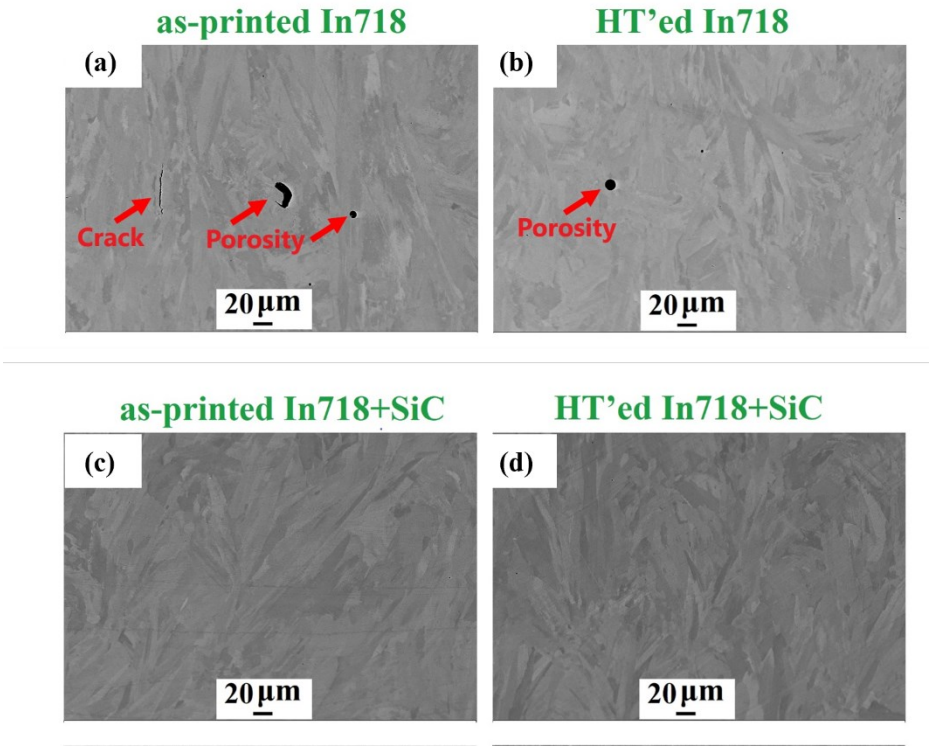

Figure 18: Secondary electron SEM images of cross sections along build direction showing cracks and pores in In718 samples and a nearly defect free microstructure in In718+SiC samples.

It is expected that this effect was also related to the increase in thermal conductivity theorized based upon the increase in high-angle grain boundaries. More effective dissipation of heat would reduce excessive recoil pressure during the melting process, which forms the basis for keyhole and gas porosities such as those observed in the In718.

It is important to note that, although fine tuning of the printing parameters would enable In718 to be produced with relative densities exceeding the 99.6% observed here, the parameters used were specifically developed for unreinforced In718 with no accounting for the SiC. It is therefore considered unlikely that this specific set of parameters just happened to better suit In718+SiC. Instead, I predict that the suppression of defects is a parameter-agnostic effect of the incorporation of ceramics with this methodology. This prediction is supported by the similarity of results seen across small variations in parameters tested with the SiC composites, as well as by the recurrence of this observation with other MMCs, such as the In718+ZrB_2 composite that will be discussed in the next chapter.

5.4 Mechanical Testing of Printed Samples

Micro-hardness testing was performed first as an initial measure of the effects of SiC reinforcement, and these results are provided in Table 3. Formation of γ'/γ" precipitates with heat-treatment resulted in a predictable increase in hardness regardless of precipitate reinforcement. The formation of new silicides and carbides by SiC reinforcement was also found to promote significant increase in hardness both with and without heat-treatment. In the as-printed case, average microhardness was measured approximately 14% higher for In718+SiC compared to In718. The effect was less drastic following the formation of γ'/γ" phases, but In718+SiC HT still achieved microhardness 8% higher than In718 HT.

Table 3: Microhardness, yield strength, and toughness results for In718 and In718+SiC

Material	*Microhardness (Hv)*	*σ_y (MPa)*	*Toughness (MJ/m^3)*
In718	319.1 ± 7.9	826	305
In718+SiC	363 ± 10.2	963	201
In718 HT	436.3 ± 11.3	1264	198
In718+SiC HT	468.9 ± 8.7	1251	195

Small-scale dogbones with 2 mm gauge width and 1.2 mm thickness were prepared as described in the sample preparation discussion in section 5.2 to conduct tensile tests. Room

temperature tensile testing was performed on at least three specimens for each sample group, and the stress-strain curves are shown in Figure 19. Yield strength (σ_y) and ultimate tensile strength (σ_{UTS}) were markedly higher with SiC reinforcement in the as-printed samples increasing by 16% and 12% respectively, nearly 150 MPa in both cases. This increase in strength came with an expected drop in elongation at failure from around 30% to 17%, but this level of ductility still offers good usability of the material for structural applications. In the heat-treated state, which is how the materials are used in an industrial setting, γ'/γ" precipitates create a similar effect to that sought out with ceramic reinforcement, dramatically increasing strength but decreasing elongation at failure to about half. Similar to the as-printed samples, In718+SiC HT achieved notable increase in σ_{UTS}, about 10%, over In718 HT, but with only a minor loss in ductility from 16% to 14% on average. Unlike the as-printed comparison however, heat-treated yield strengths with and without SiC reinforcement were almost equivalent. The in-situ produced silicide and carbide precipitates evidently act as primary barriers to dislocation movement in the as-printed state, thereby having profound effects on both σ_y and σ_{UTS}. However, these results suggest that after heat-treatment the barrier presented by the γ'/γ" precipitates is significantly higher, such that the stresses required to induce plastic deformation against these phases will also readily overcome carbides and silicides. This may also be affected by the change in geometry of the ceramic phases noted from STEM analysis, shifting from spirals to smaller particles that may be more easily surmounted by dislocation glide. Results also suggest, though, that the additional grain pinning effects imparted by the ceramic reinforcement allow for higher strain hardening rate, and the value of the increase in σ_{UTS} with very little loss in ductility should not be discounted.

Table 4 presents a comparison of strengths and elongation between the materials considered in this study and several similar examples of In718 MMCs, along with results for wrought In718. Based on this comparison, In718+SiC HT could be stated to achieve among the best combinations of mechanical properties, reaching the highest value for σ_{UTS} of the compared examples, while also maintaining better ductility than other produced MMCs.

Table 4: Comparison of room temperature tensile results to literature data on previous In718 MMCs

Material	***σ_y (MPa)***	***σ_{UTS} (MPa)***	***Elongation (%)***
In718 as-printed (this study)	826	1095	30.3
In718 HT (this study)	1264	1398	16.1
In718+SiC as-printed (this study)	963	1228	17
In718+SiC HT (this study)	1251	1527	13.8
In718+ 2 wt% TiC as-printed [124]	774	1029	12.3
In718+2 wt% TiC HT [124]	1144	1380	9.1
In718 + 1 wt% Y_2O_3 as-printed [152]	850	1100	17
AMS 5662G specification for wrought In718 [141]	1035–1167	1275–1400	12–21

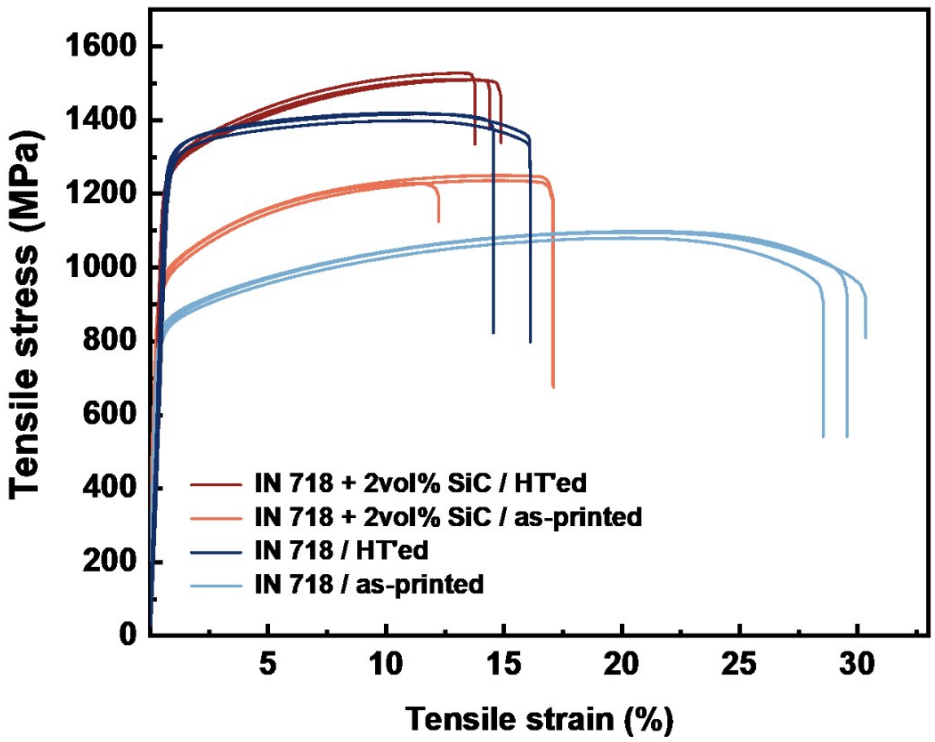

Figure 19: Room temperature tensile results for In718 and In718+SiC samples with and without heat-treatment.

Finally, additional tensile testing was performed with In718 HT and In718+SiC HT at a testing temperature of 800°C in order to determine if this MMC would be expected to offer any improvement in the upper temperature limits and improve survivability in ARC or other advanced energy production designs. In stress-strain curves from these tests, provided in Figure 20, unreinforced In718 HT is found to achieve σ_y near 550 MPa and extreme brittleness, fracturing at less than 1% elongation. Significant property degradation along these lines is expected at this temperature, though it is noted that wrought material has been shown to maintain slightly better ductility and strength [153] than LPBF In718, mostly due to the elongated grain structure and increased porosity level in the latter. In718+SiC HT in this test at 800°C achieved a σ_y of about 450 MPa, decreasing by 100 MPa compared to the unreinforced material, unlike the behavior at room temperature. Nonetheless, ductility is found to improve, reaching an elongation at failure of 3%, which is about triple that of the In718 HT at this temperature. The exact mechanism for this change remains unclear at this point. One possibility is that the elevated temperatures increase stability of the NbC phase, shifting the equilibrium composition towards decreased concentrations of the Ni_3Nb γ" phase. TTT diagrams of typical In718 suggest that formation of a NbC phase is most favored around 800°C, typically requiring around 10 h of aging to form [154]. Increased C content from the introduction of the SiC reinforcement evidently promotes some Nb-carbide formation under the intense laser melting conditions, but if it also shifts the equilibrium to allow for increased formation under shorter time frames at 800°C, then the associated decrease in γ" phase could account for the observed strength/ductility shift. However, verification of this theory or the development of others will require significant in-situ observation of phase behavior for In718+SiC MMCs over a range of temperatures in future studies.

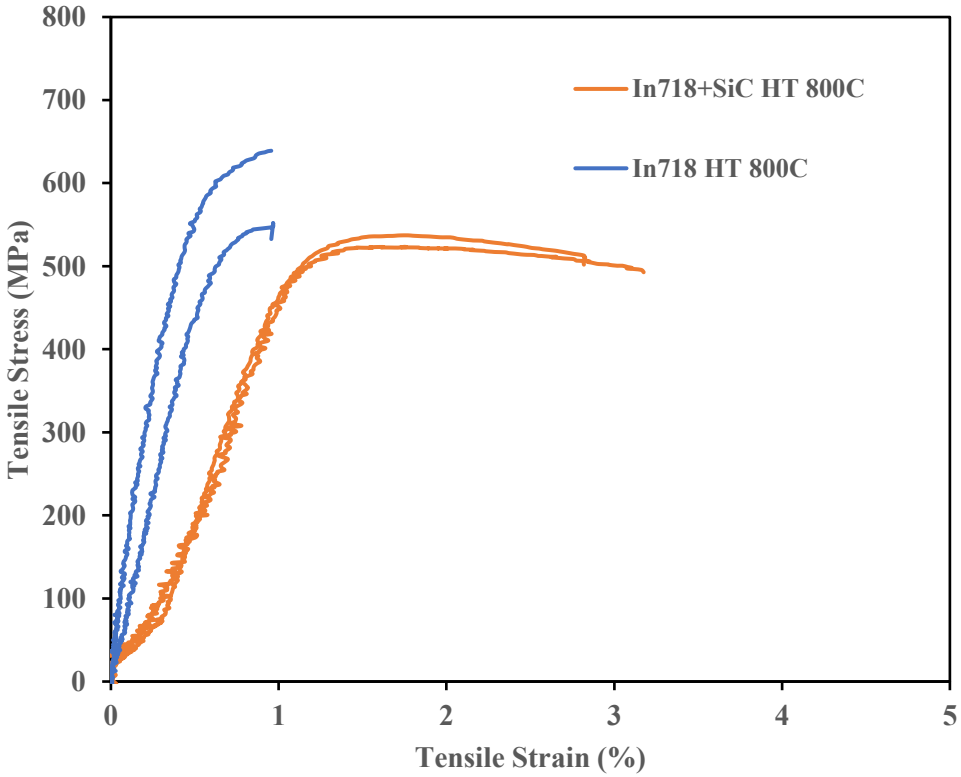

Figure 20: High-temperature tensile results for heat-treated In718 and In718+SiC at 800°C

5.5 Conclusions for In718+SiC MMC

The work performed in this study demonstrated the capability for introduction of a new MMC combination through the in-situ formation of (Nb, Ti)-based silicides and carbides in In718 by addition of SiC nanowires. SiC demonstrated good capability for mechanical alloying with In718 powders via ball milling, and fine tuning of the milling conditions allowed for uniform distribution of the ceramic while maintaining adequate size distributions and sphericity for spreadability. High quality samples were prepared at the cm-scale by LPBF, and SEM analysis revealed that the inclusion of SiC actually improved print quality, decreasing the formation of pores and cracks to achieve higher relative density. This result in itself presents an interesting side effect of ceramic nanomaterial inclusion that may create merit for the future use of MMCs, as incapability to achieve 100% relative density is considered one of the major downfalls of current AM technology.

In addition to improved print quality, newly formed silicide and carbide phases were found to induce pinning of the grain boundaries, resulting in a slight reduction of average grain sizes. Furthermore, In718+SiC samples demonstrated an increased proportion of high-angle grain boundaries, indicative of improved stress relief during solidification that is likely related to enhancements in thermal conductivity.

In room temperature mechanical testing of the produced samples, In718+SiC achieved significant increases in both hardness and strength both with and without the industry standard heat-treatments. In the case of the heat-treated samples, this increase was found to be restricted to the σ_{UTS} and a result of increased strain hardening, and the In718+SiC HT and In718 HT samples achieved nearly identical σ_y. The increase in ultimate strength may offer some benefit for decreasing deformation in load-bearing applications where stresses are expected to approach the plastic deformation regime, and exceptionally low loss in ductility was observed for the In718+SiC HT compared to the In718 HT, so toughness is well maintained. In comparison to other In718 MMCs with similar ceramic concentrations reported in the literature, the results achieved for In718+SiC HT in this study were among the best combinations of strength and ductility, so this metal-ceramic combination is believed to have high merit for further optimization.

In elevated temperature mechanical testing at 800°C, the increases in strength observed at room temperature from SiC inclusion were lost, and strength was actually observed to decrease compared to the unreinforced metal. However, elongation at failure was found to be approximately 3x higher. This increased ductility does provide improved toughness and may be expected to slightly enhance creep lifetime. Therefore, if a 3D printed In718 material were desired for the construction of the ARC vacuum vessel, the In718+SiC MMC may offer improved lifetime, though its use may require a slight increase in vessel wall thickness to account for the 100 MPa loss in $\sigma_{y.}$ If one considers the expected decrease in irradiation effects expected with the higher sink density from additional nano-precipitates, this material might be even more highly recommended. If 3D printing is not deemed necessary for the vacuum vessel, however, improved properties from the MMC formation do not appear to surpass the loss in properties from AM compared to wrought In718 based on the results achieved here.

Further improvements in 3D printing technology and improved control over grain morphology, which were not a focus of this present work, might help to overcome the gap between printed and wrought materials, making MMCs a more attractive alternative for high-temperature operations. Furthermore, the results reported here are for a single promising MMC at a specified ceramic concentration. Variations in ceramic concentration may offer significant property tunability, and further exploration of additional reinforcing ceramics, one of which will be discussed in the next chapter, might reveal In718 MMCs with even better performance. Regardless of potential improvements though, In718 is a workhorse material of modern industry, and many applications outside of ARC exist which may benefit from improvements in strength at operational temperatures lower than 800°C, making In718+SiC an attractive alternative to consider.

Chapter 6

Ceramic Reinforcement of Inconel 718: ZrB_2

Based on results achieved with the In718+SiC described in Chapter 5 of this thesis, Ni-based MMCs appear to hold good potential for improvement of mechanical properties for extreme environment applications. If utilization in an ARC vacuum vessel is considered to be a primary goal however, the increase in ductility offered by In718+SiC at 800˚C may not adequately compensate for the loss in strength compared to unreinforced printed In718, and wrought In718 would be expected to outperform 3D printed In718 with or without SiC until a higher level of control is achieved over grain morphology. Fabrication of 3D printed MMCs with significant enough enhancement of properties to merit use of the materials over wrought In718 will require greater enhancement in high-temperature ductility first and foremost. Considering the Ni-based MMC combinations that have been tested to this point, embrittlement with TiC addition was found to be more severe than SiC [124], but TiB_2 addition has shown some improvement in high-temperature ductility [126]. Further exploration of transition metal diborides, which have so far been largely limited to the TiB_2 ceramics, might therefore present the sought-after high-temperature improvements. Many transition metal diborides fall into the class referred to as ultra-high temperature ceramics (UHTCs), which exhibit melting temperatures above 3000˚C, excellent hardness, oxidation resistance, and chemical inertness at elevated temperatures, making them attractive

candidates for implementation in new MMCs [155–157]. ZrB_2 is one such UHTC with low density, good mechanical properties, and good corrosion resistance [158], which could be expected to have good compatibility with In718. In this chapter, I present work conducted as part of my PhD research to produce and evaluate In718+ZrB_2 MMCs using a similar process flow to that described in Chapter 5. In the following sections I will detail the fabrication methods, present analysis of the printed microstructures, and discuss the results and implications of mechanical testing at room and elevated temperatures, making comparisons to both unreinforced In718 and the previous In718+SiC.

6.1 Sample Production for In718+ZrB_2

In718 powder in the size range 15-45μm from MSE Supplies LLC was mixed with ZrB_2 powder consisting of nanoparticles less than 100 nm in diameter purchased from US Research Nanomaterials Inc to form a mixture with 2 vol% ZrB_2. Powders were mixed in a high-speed blender for 90 minutes and sieved at 100 μm to remove agglomerated particles. In this case, small batch testing showed good distribution of ZrB_2 across In718 particles that was well maintained over time, so mechanical milling was forgone as a potentially unnecessary source of additional impurities. SEM imaging and EDX mapping of the pre- and post-blending powders, provided in Figure 21, displayed promising results for LPBF. Close observation of single In718 particle surfaces shows observable coating with the ZrB_2 nanoparticles, and wider-scale EDX of the powder sample shows good distribution of the Zr and B elements throughout the sample. Powders were also observed to retain good sphericity, necessary for adequate spreading during the LPBF process.

Fabrication of In718+ZrB_2 samples from the blended powder followed the same procedure as In718+SiC, including printing in an EOS M290 LPBF using the default settings for In718, which can be found in Table 2 in Chapter 5. A subset of the printed samples was also subjected to the same industry standard heat-treatment after removal from the build plates via EDM, involving heating to 1050℃ followed by water cooling, aging at 720℃ for 8 h followed by cooling in the furnace, and aging for an additional 8 h at 620 ℃ followed by cooling in air. These will be indicated with *HT* hereon. Tensile samples for room temperature and high-temperature testing were cut by EDM as shown in Figure 22.

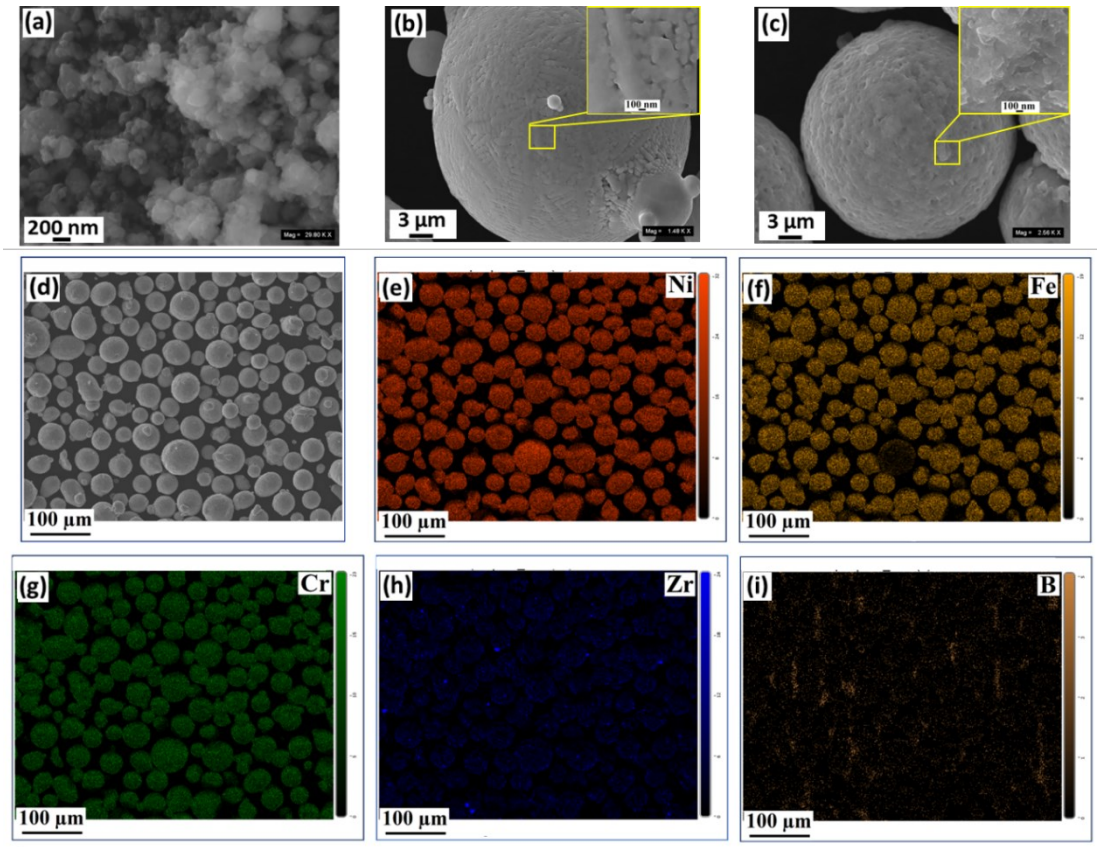

Figure 21: SEM images of (A) commercial ZrB_2 powders, (B) pre-mixing In718 particle surfaces, and (C) ZrB_2 decoration on the In718 particle surface after blending. (D-I) EDX mappings of blended composite powder.

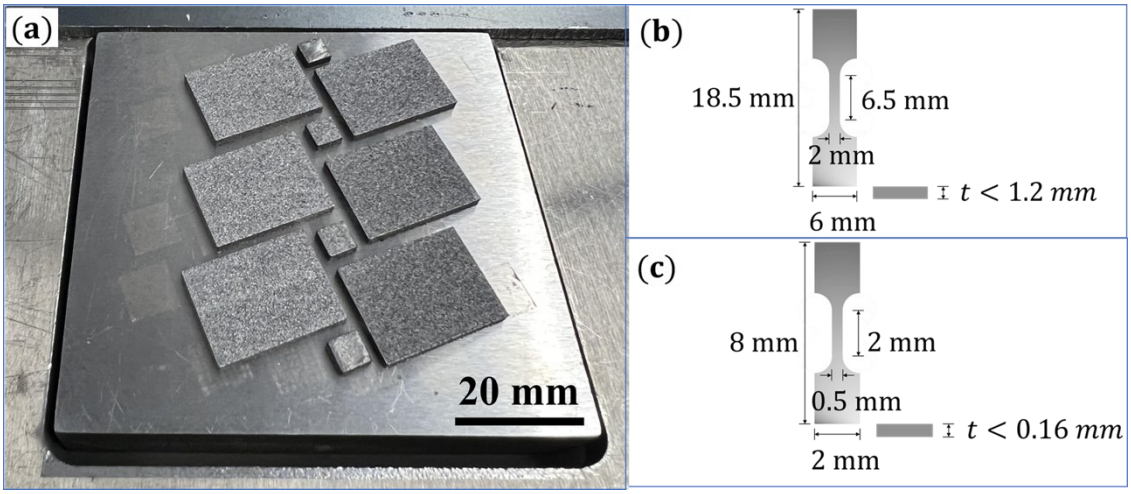

Figure 22: (A) In718+ZrB2 samples printed by LPBF, and diagrams of specimens for (B) room-temperature tensile testing and (C) high-temperature tensile testing.

6.2 Microstructure Analysis of Printed Samples

XRD analysis was carried out using Cu K_{α} (λ=0.154 nm) radiation over the range of scattering angles between 2θ = 10-90° and is presented in Figure 23a. Although signals relating to the FCC γ (Ni-Cr-Fe) phase are easily observed, signals from precipitate phases (both the γ'/γ" and those resulting from ZrB_2 inclusion) were found to be too weak for observation under the testing parameters used. Despite this, such phases were found to be discoverable by STEM/EDX. Figure 23(b-h) display regions enriched in Ni, Ti, Nb, and Al, but depleted in Fe and Cr, which were observed in a sample of In718+ZrB_2 HT. These elemental compositions are indicative of the successful formation of the γ' and γ" phases during heat-treatment, and these phases were observed at the scale of tens of nm. These results for precipitation from heat-treatment fall within expectations, but they are included here for verification that the introduction of ZrB_2 did not disrupt this process for the room temperature samples. Apart from the γ'/γ" phases, Figure 23(i-p) also indicates the formation of new phases directly related to the addition of the ZrB_2. Based on these EDX mappings, it seems clear that ZrB_2 underwent a dissolution process during laser melting similar to that observed for the SiC reinforcement. Strong signals for Zr and for B are observed in several separate locations in the observed cross-sections with various combinations of other elements, suggesting the formation of a variety of intermetallic compounds and complex borides. In these images, yellow arrows indicate regions found to consist primarily of (Zr, Ni)-based intermetallic nanoparticles, generally below 200 nm in diameter. On the other hand, regions indicated by red arrows appeared to be examples of (Nb, Mo, Cr)-rich boride nanoparticles at similar size-scales (100-200 nm). The presence of these phases suggests that the laser melting process promoted the decomposition of ZrB_2, allowing free B diffusion to react with elements with stronger affinities while the free Zr reacted with neighboring Ni elements. This was expected to be a potentially positive result for mechanical performance, as the secondary borides would still provide grain pinning strengthening effects, and (Zr, Ni)-based intermetallics are often considered excellent dispersion-strengthening constituents due to their thermal and mechanical stability [159]. Similar secondary intermetallic and boride phases were observed in STEM analysis of the untreated In718+ZrB_2 as well.

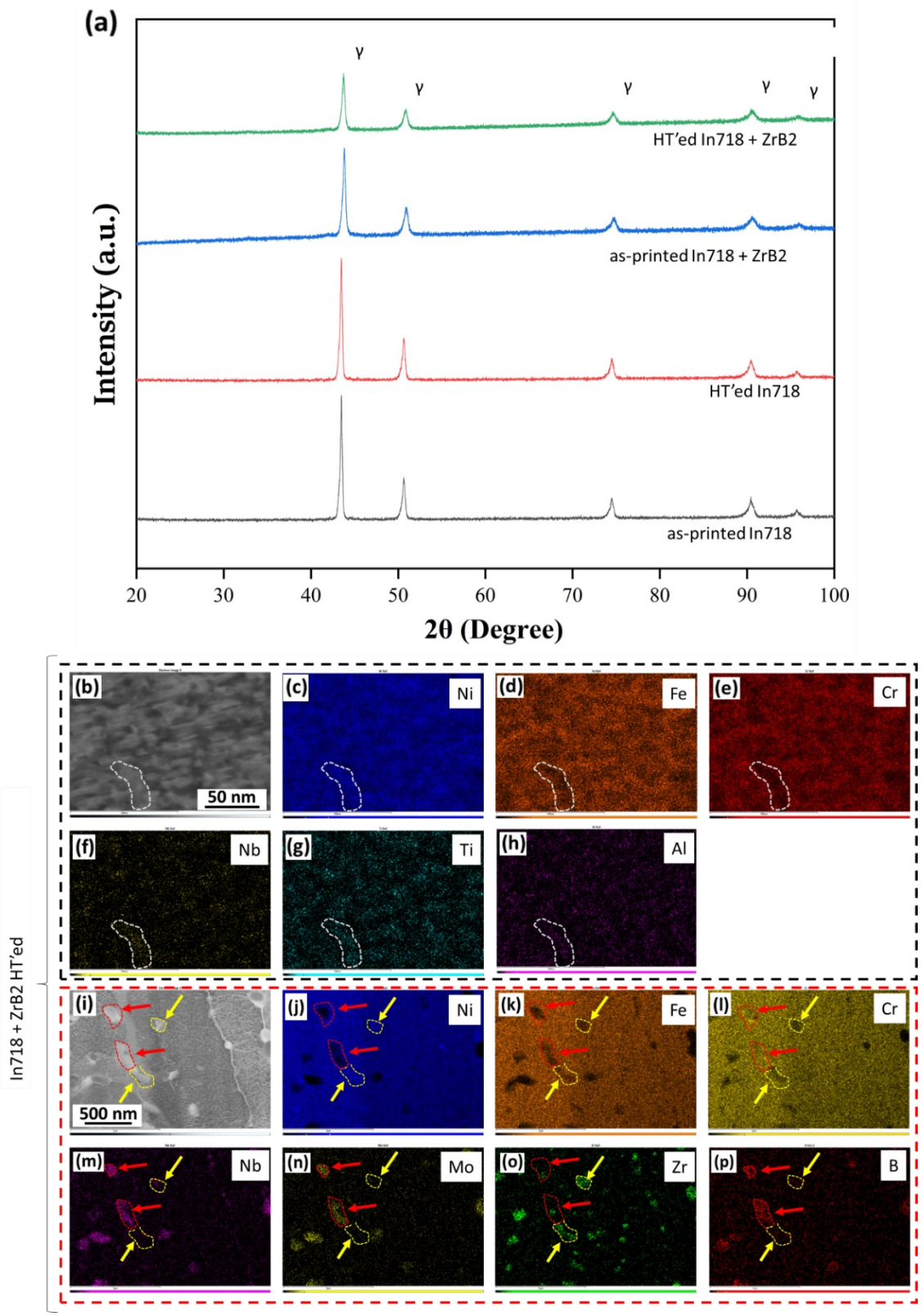

Figure 23: (A) XRD results from printed samples. STEM/EDX mapping of In718+ZrB_2 HT showing (B-H) γ' and γ" precipitates and (I-P) (Nb, Mo, Cr)-borides and (Zr, Ni)-based intermetallic nanoparticles.

Further observations of the microstructural development in the printed samples were also obtained through SEM analysis at lower-magnification, and these images are provided in Figure 24 for the heat-treated and untreated samples of both the In718+ZrB_2 and the unreinforced In718 printed previously. Small spherical pores at size-scale of tens of μm, which are believed to be gas-entrapment porosity from the LPBF process, are visible in the cross-sections of the In718 and In718 HT samples. These are labelled with white arrows. As with the findings of the previous study on SiC reinforcement however, almost no pores or cracks are observable in ZrB_2-doped samples. This would appear to be further validation of the positive effects of nano-ceramics on the quality of solidification during LPBF, and a more in-depth discussion of this phenomenon will follow later in this section. Observable grains in these SEM images were also noted to be significantly smaller in the ZrB_2 MMC samples, which will be more extensively studied with EBSD imaging later in this section as well.

In addition to information about porosity and grain development, Figure 24 also provides further evidence of secondary phase formation. In the higher magnification ZrB_2 images (f and h), specific regions are found to be visibly brighter under SEM and to shift from long and thin geometries in In718+ZrB_2 to smaller and more granular geometries in In718+ZrB_2 HT, labelled as points 1 and 3 with blue arrows. High concentrations of Nb and Mo from EDX observation confirm these to be Laves phases. Such Laves phases are typical of laser melted nickel superalloys and their geometries are controlled by heat-treatment to maintain favorable effects on mechanical properties, (e.g., granular Laves phases retain ductility better than long-striped phases) [160]. Laves phases in these specimens were found to be similar to those in both In718 and In718+SiC samples as far as can be reasonably observed. This is specially noted here because Zr formation of intermetallics with Ni could feasibly have affected the formation of the Laves phases and created a need for adjusted heat-treatment steps to optimize performance. Though some change in heat-treatment might still be found to be more appropriate for MMC In718, the need for this is not apparent here from observation of the Laves phases. Fine, dark spots (notated by red arrows) with diameters less than 100 nm were also identified scattered throughout the matrix in the In718+ZrB_2 and In718+ZrB_2 HT samples, but not in the unreinforced In718 samples. EDX analysis on points 2 and 4 suggest these to be the

previously mentioned (Zr, Ni)-based intermetallics, and observation from these images suggests good distribution of these throughout the printed samples. Table 5 presents the EDX elemental compositions from points 1-4 in Figure 24(f and h) for reference.

Next, Figure 25 presents STEM/EDX data at particularly high-magnification and focused specifically on a region where Zr and B secondary phases have been identified in a In718+ZrB_2 HT sample. Three different phase zones are evident in these images apart from the typical structures expected in an In718 HT sample. First, the region encompassed by the blue line in the black and white STEM image was found to contain the highest concentration of B, along with notably higher concentrations of Nb and Mo and lower concentrations of Ni than the surrounding base matrix. This clearly corresponds to the (Nb, Mo, Cr)-based boride phases previously suggested. The region enclosed by the red line was found to have a similar geometry but with particularly strong signals for Ni and Zr, indicating the formation of the (Zr, Ni) intermetallic phases. Finally, a small region containing both Zr and B in concentrations near what would be expected for unreacted ZrB_2 was identified within the (Nb, Mo, Cr)-boride zone and is indicated by the pink lines. These observations appear to confirm the breakdown and separation of the originally added ZrB_2, though it is notable that some retention of the original ZrB_2 was observed, whereas SiC was found to be completely decomposed to the extent that could be observed. EDX elemental compositions for each zone are provided in Table 6 for reference.

EBSD was performed on In718+ZrB_2 and In718+ZrB_2 HT samples in order to further explore the decrease in grain sizes observed through secondary electron SEM, and this data is presented compared to data from the unreinforced samples in Figure 26. Grain size reduction for ZrB_2-reinforced samples was found to be more drastic than for the SiC-reinforced samples. Maximum feret diameters of individual grains were found to reach up to almost 400 μm in the untreated In718 but were reduced to less than 240 μm following heat-treatment. This value for the In718 HT is still approximately twice as large as the maximum feret diameter observed for either In718+ZrB_2 or In718+ZrB_2 HT, both of which were less than 120 μm, indicative of the hindrance to grain growth from the ceramic particles. The proportion of high-angle grain boundaries was also found to increase for the ZrB_2 samples, once again suggesting a reduction of thermal stress during printing, similar to the SiC. However, this effect was found to be less pronounced after heat-treatment.

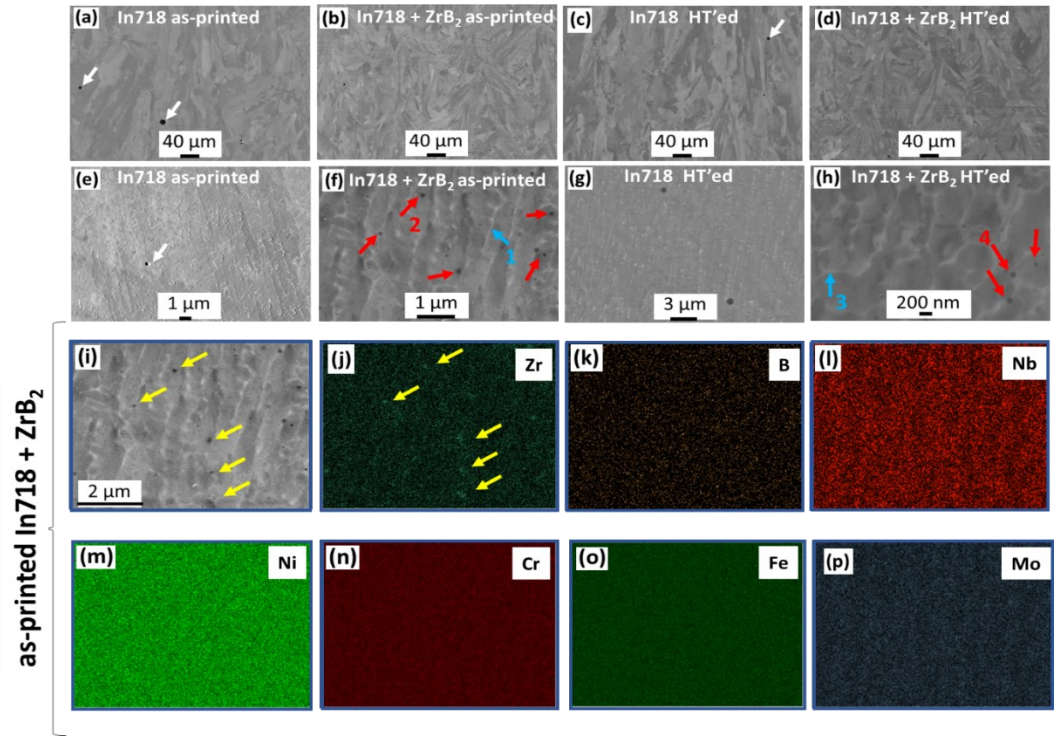

Figure 24: (A-H) Secondary electron SEM images from printed In718 and In718+ZrB2 samples, and (I-O) EDX mappings from In718+ZrB2 HT.

Table 5: EDX elemental composition results by wt% for points from Figure 24

Element	*Point 1*	*Point 2*	*Point 3*	*Point 4*	*Average*
Ni	53.85	37.46	52.37	37.63	51.68
Fe	19.82	9.87	18.23	7.98	18.15
Cr	18.12	1.94	19.75	1.12	18.44
Nb	10.39	-	10.13	-	4.58
Ti	0.93	-	0.72	-	0.7
Al	0.7	-	0.48	-	0.89
Mn	0.05	-	0.13	-	0.08
Si	0.36	-	0.35	-	0.37
Mo	7.51	-	8.55	-	2.73
Zr	0.19	52.88	0.21	51.11	1.84
B	0.08	0.11	0.08	0.16	0.54

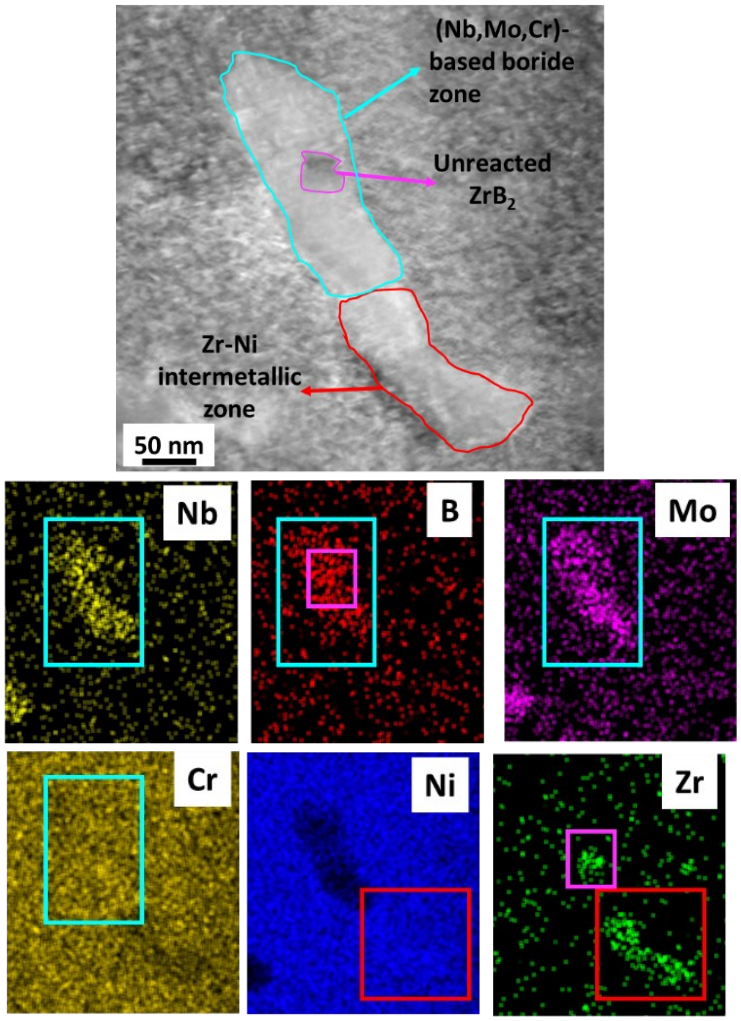

Figure 25: High magnification STEM/EDX mappings of In718+ZrB2 HT focusing on exchange reaction zone for dissolution of ZrB2.

Table 6: EDX elemental compositions in wt% for phases observed in Figure 25

Element	***(Nb,Mo,Cr)-based boride zone***	***Unreacted ZrB_2 zone***	***Zr-Ni intermetallic zone***
Ni	-	0.39	46.18
Fe	-	0.12	1.26
Cr	20.60	0.17	1.49
Nb	27.54	-	-
Mo	22.83	-	-
Zr	-	86.40	51.07
B	29.03	12.92	-

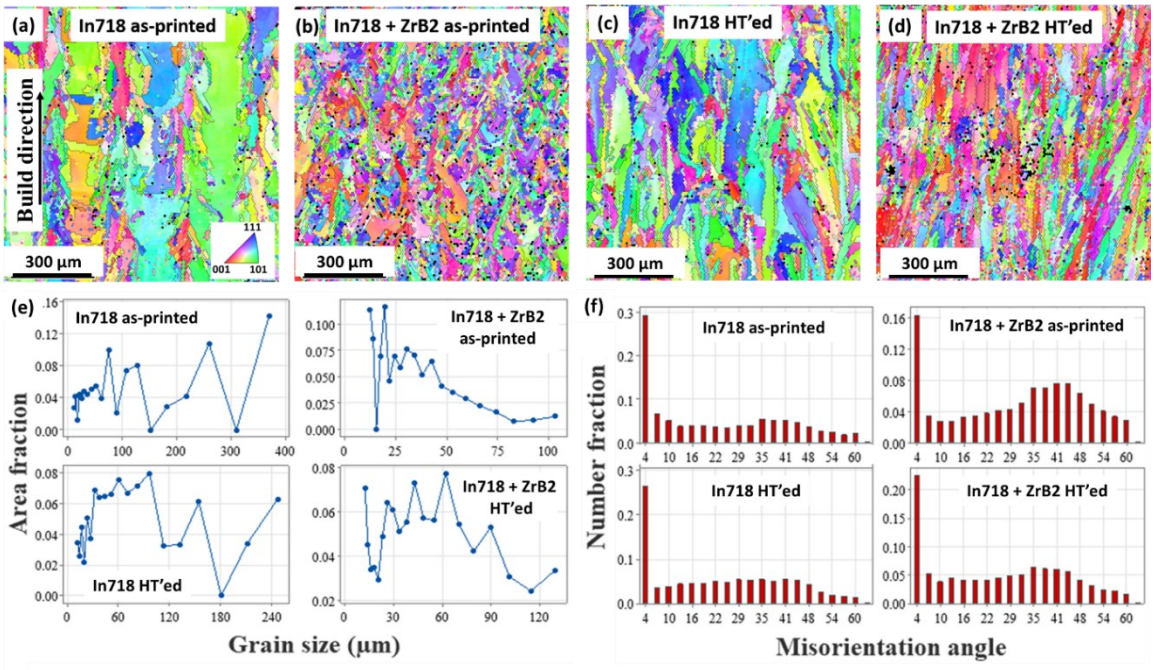

Figure 26: (A-D) EBSD orientation maps from LPBF printed samples, and corresponding (E) grain size distributions and (F) misorientation angle distributions.

Following cross-sectional imaging of the printed samples, X-ray CT was performed on 4 mm x 4 mm x 2 mm samples of untreated In718 and In718+ZrB_2 in a Zeiss Xradia 620 Versa X-ray microscope to create 3D renderings of the printed samples that would allow for a more complete analysis of porosity formation during printing. These renderings are provided in Figure 27, along with histograms of the pore count organized by maximum feret diameter. The reconstructions shown highlight pores with feret diameters exceeding 10 µm in the interior of the printed samples. Regions of interest were selected more than 200 µm away from each sample face to best approximate results expected in larger scale printing, avoiding edge effects and the heat-affected zone of the EDM used to separate samples from the plate. The difference in porosity appears visibly drastic. The In718 sample displayed more than 1200 relevant pores and the diameter of the largest pores reached nearly 180 µm, with 95% of pores falling under 90 µm. Meanwhile, the In718+ZrB_2 displays less than 200 pores with diameters that all fall below 50 µm. Volumetric analysis of these regions of interest found that the In718 sample reached 99.90% density, which would certainly be considered a high-quality print and meet the

expectations for utilizing settings designed specifically for In718 by EOS. By comparison, the addition of the 2 vol% ZrB_2 was found to increase the density to >99.99%. The benefits of this difference in porosity might not be immediately apparent in simple tensile testing, as the strength- and ductility-changing effects of the new intermetallics and boride phases would be expected to play a much more significant role when considering the high quality of both prints. However, decrease in porosity, and especially a decrease in the maximum pore size, might play a significant effect in the fatigue lifetime of the material. In a 2018 study by Prithivirajan et al [161], researchers analyzed the fatigue response of In718 materials prepared by LPBF and identified a lifetime-limiting critical pore size of 20 μm for printed samples with average grain size of 48 μm (similar to the average grain size observed here for ZrB_2 samples). At this critical size, fatigue crack nucleation was found to shift from initiation in the crystallographic features to initiation in the pore vicinity. While both the reinforced and unreinforced samples do exhibit pores that exceed this critical size, the much lower quantity and size of the ZrB_2-doped sample would be expected to significantly reduce the effects and resist crack initiation for longer, adding merit to the use of MMCs in structural applications where 3D printed materials are desired.

At this point, the exact reasoning for the observed decrease in porosity with the addition of the ceramic nanomaterials remains unclear. As previously discussed, analysis of the microstructure indicates improved thermal conductivity of the reinforced materials, a commonly sought after benefit of MMCs. This may result in reduction of defect-promoting stresses during the solidification process, but the effects of this on gas entrapment, which seems to be the most common form of porosity observed, are not fully apparent. Alternatively, coating the metal particles with ceramics prior to melting might be expected to decrease refractivity and promote better energy absorption from the laser. Absorbance of the powder was measured via UV-vis spectrophotometry as $\log_{10}(1/R)$ using a Universal Reflectance Accessory to test this theory, as presented in Figure 28. Absorbance was measured to be higher for In718+ZrB_2 at the relevant wavelength for the EOS M290 laser, but the difference was minimal (53.4% vs 52.8%). As such, this is not expected to be the root cause of the improved solidification. It is noted that the absorbance of the liquid melt pool would be expected to behave differently than the unmelted powder and might be found in future studies to play a larger role in the

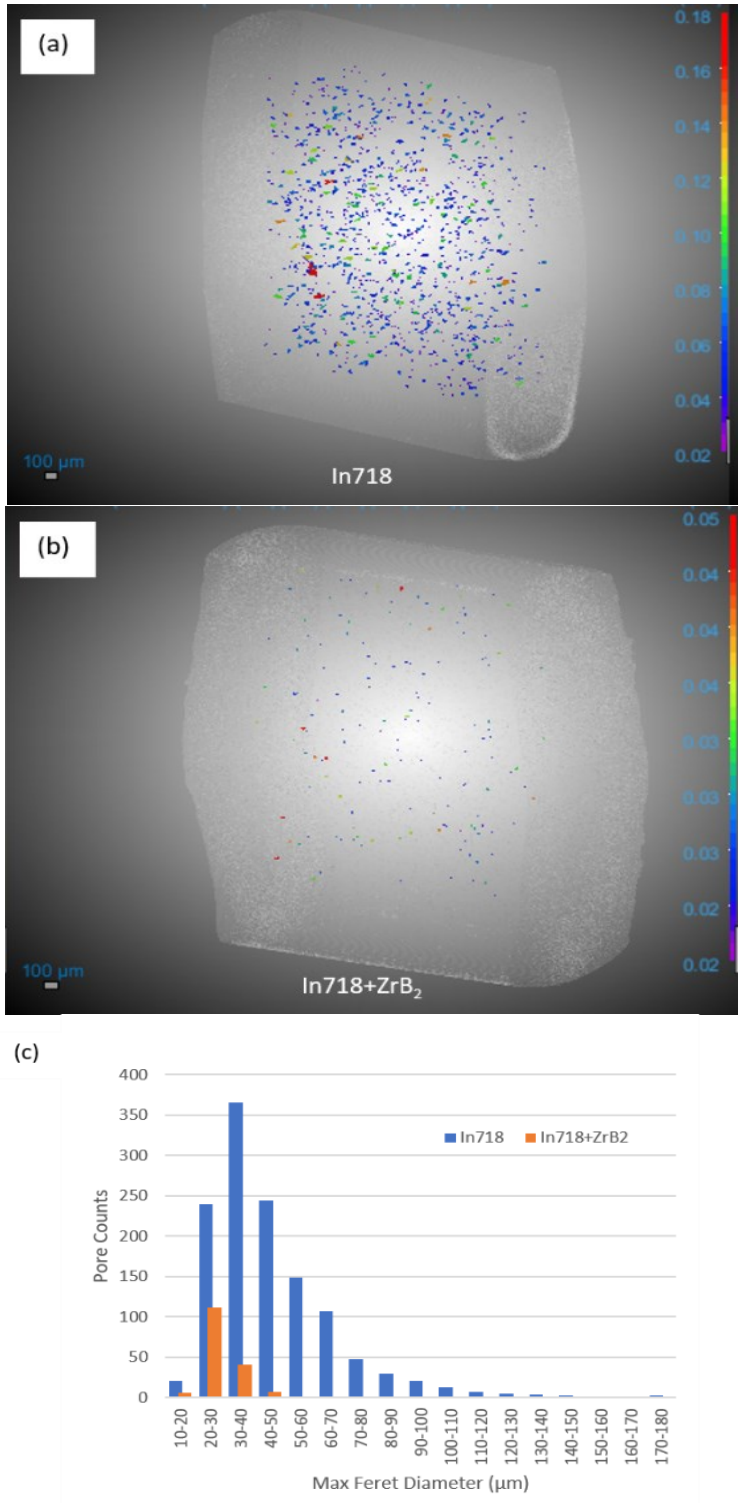

Figure 27: X-ray CT analysis of pores greater than 10µm diameter for printed samples of (A) In718 and (B) In718+ZrB_2. Color bars indicate max feret diameter of pores in µm. (C) Histogram of pore counts by max feret diameter.

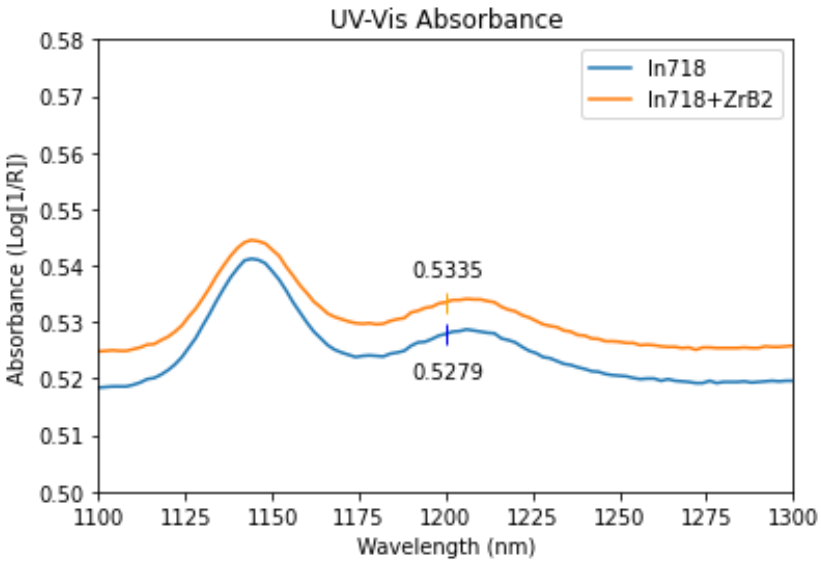

Figure 28: UV-Vis absorbance measurements for In718 powder with and without ZrB_2.

solidification behavior, but the in-situ measurements required to verify this were outside of the realm of capabilities due to the use of a commercial printer in the present studies. Finally, I expect that there is a strong likelihood that the addition of ceramic particles may have a positive effect on both the viscosity and surface tension of the melt pool, as well as the wettability of near-molten particles with each other, which may support the observed reduction in porosity. In a 2022 study by Qu et al [162], researchers reported enhanced control over spatter in the LPBF fabrication of Al6061 with the addition of about 4 vol% of TiC. They attributed this change to two mechanisms: 1) elimination of spattering by liquid breakup by decreasing capability of vapor pressure to overcome the capillary pressure from surface tension, and 2) suppression of spatter droplet coalescence due to a nanoparticle surface barrier on ejected droplets. Simply put, ceramic nanoparticles were found to both decrease the quantity of liquid droplets ejected during melting and decrease the likelihood of the remaining ejected particles combining into larger droplets. Spatter is a known issue during the printing process that can result in partially unmelted particles disrupting the solidification process and leaving gaps in the structure, so minimization of this effect as suggested could certainly play a role in the observed suppression of defects. It seems reasonable to expect that such behavior would result from other ceramic nanoparticles similarly to the observations with TiC. Once again though, further studies involving in-situ observation would be required to verify this effect in the present materials.

6.3 Mechanical Testing of Printed Samples

Upon completion of microstructural analysis, mechanical testing was performed for the In718+ZrB_2 materials to measure any enhancements in performance compared to the undecorated or SiC-doped samples. First, microhardness results are provided in Table 7. ZrB_2-doped samples were found to have the highest microhardness values both with and without heat-treatment. In the as-printed condition, hardness was found to increase by 49% over the unreinforced materials, while in the heat-treated condition hardness increased by 32%. These findings match expectations based on previous results with TiB_2, such as a report by Zheng et al, who found a 100% increase in hardness of as-printed In718 with the addition of 5 vol% TiB_2 [163].

Table 7: Microhardness results for In718+ZrB_2 compared to In718 and In718+SiC.

Material	***Microhardness (Hv)***
In718 as-printed	319.1 ± 7.9
In718 HT	436.3 ± 11.3
In718+SiC as-printed	363 ± 10.2
In718+SiC HT	468.9 ± 8.7
In718+ ZrB_2 as-printed (this study)	475.7 ± 13.0
In718+ ZrB_2 HT (this study)	576.2 ± 10.6

Average room temperature tensile stress-strain curves are displayed in Figure 29. In718+ZrB_2 samples achieve considerable increases in both σ_y and σ_{UTS}, with In718+ZrB_2 HT reaching the highest values of the compared materials with σ_y of approximately 1350 MPa and σ_{UTS} of nearly 1600 MPa. This is a considerable increase in strength, though it comes at the price of a much more severe loss in ductility and toughness than that observed with the SiC-reinforced materials. Elongation at failure drops to less than 8% for the as-printed ZrB_2 material, while the heat-treated elongation drops slightly further to 5%.

When tested at elevated temperatures, as shown in Figure 30, especially interesting behavior is observed. At 650°C, generally accepted as the upper temperature limit for structural usage of In718 due to embrittlement and loss of creep resistance, tensile behavior

follows the same general trend as at room temperature. In718 HT exhibits a drop in strength to a σ_y of approximately 900 MPa and a drop in elongation to about 2%, while In718+ZrB_2 HT achieves slightly higher σ_y and lower elongation, at close to 1000 MPa and 1.5% respectively. When raised to 800°C, In718 HT continues to degrade in all aspects, and the difference in strength between the reinforced and unreinforced samples becomes minimal, but the In718+ZrB_2 HT samples suddenly exhibit a drastic increase in ductility. Each of the samples tested were found to reach elongation at failure of 8% or more, surpassing even the untreated room temperature elongation of the In718+ZrB_2. As presented in Figure 31, this is also a reversal of the toughness to strength relationships established in the In718 and In718+SiC materials.

Once again, the exact mechanisms behind the observed changes in behavior around 800°C are not immediately apparent. For In718+SiC materials, I suggested in Chapter 5 that a shift in phase equilibrium at the elevated temperatures might favor the formation of additional NbC phases in place of γ", leading to an associated shift in strength versus ductility. While a similar effect is also certainly possible in the ZrB_2 system, comparison of the untreated In718+ZrB_2 to the In718 HT system in room temperature tensile results suggests that the borides and intermetallics formed in the ZrB_2 have a more significant embrittling effect than the γ'/γ" phases, so an increase in borides seems unlikely to result in the observed effect. However, another possibility might be an increase in the equilibrium concentration of free B particles. In a 2005 study comparing the effects of boron and carbon additives on the fracture behavior of In718 [164], it was found that small quantities of B particles selectively segregate to grain boundaries instead of forming borides. While the typical intergranular and intragranular boride and carbide precipitate phases are shown to enhance grain boundary pinning, the beneficial effects of these are mostly lost by 650°C when the primary deformation mechanism shifts from grain boundary sliding to intergranular cracking. Segregated B particles, on the other hand, demonstrate improvements in grain boundary cohesion and promote deformation by transgranular cracking rather than intergranular, increasing fracture toughness. The described study found that a plateau for B particle concentration at the grain boundaries is reached at 60 appm of B in the In718 as a whole for a temperature of at 650°C. If the equilibrium concentration for B at the grain boundaries were to increase significantly at higher

temperatures however, then a shift from embrittling borides to grain boundary strengthening boron might feasibly achieve the observed increase in ductility at 800°C. Finally, another possibility might be an increased strain-rate sensitivity in the ZrB_2 materials at high-temperatures. Strain-rate sensitivity, $m \equiv d\ln\sigma/d\ln\dot{\varepsilon}$, has been demonstrated to have a large numerical effect on necking instability in materials under uniaxial tension in the nonlinear regime [165]. Results would suggest that both In718 and In718+ZrB_2 should have larger m at 800°C than at 650°C or room temperature. However, the restricted length scales associated with smaller grains and increased presence of nanophases may well increase this dependence in In718+ZrB_2 [166]. These theories will be assessed for validity through further high-temperature experiments to observe phase changes and effects of strain rate on the In718+ZrB_2 materials in future experiments.

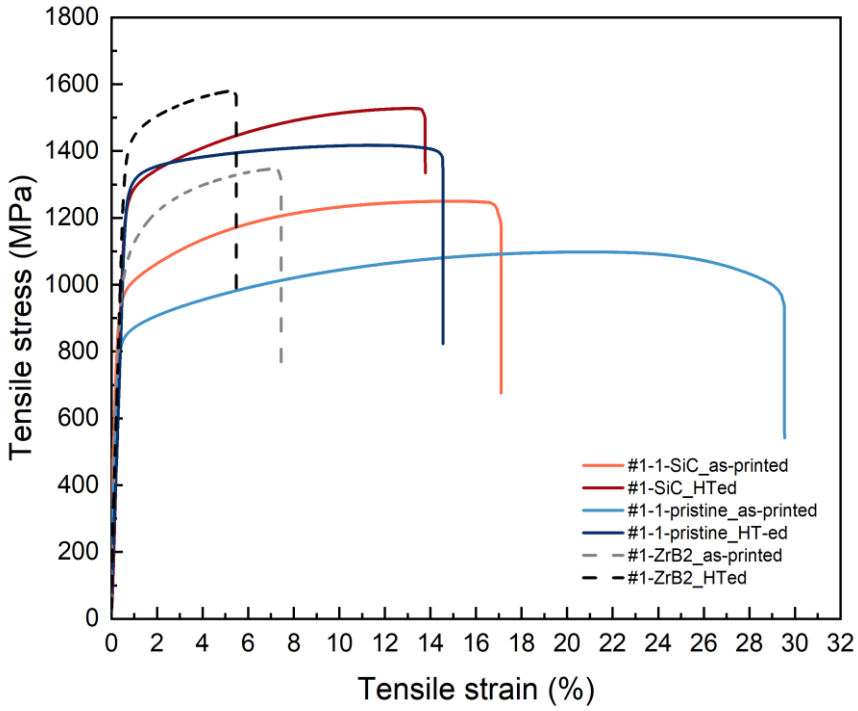

Figure 29: Room temperature tensile results for In718, In718+SiC, and In718+ZrB_2 samples

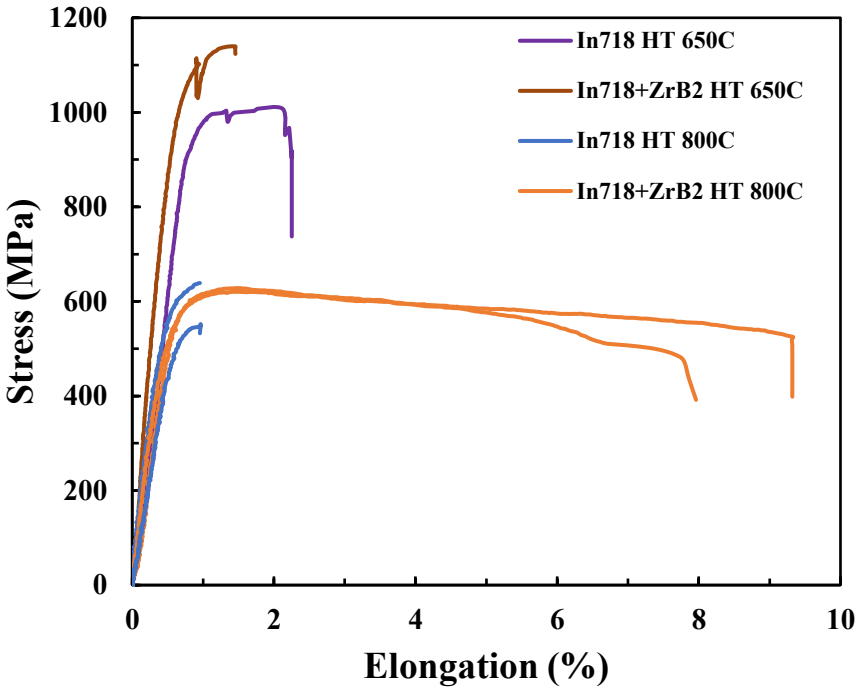

Figure 30: High-temperature tensile results for In718 HT and In718+ZrB_2 HT samples

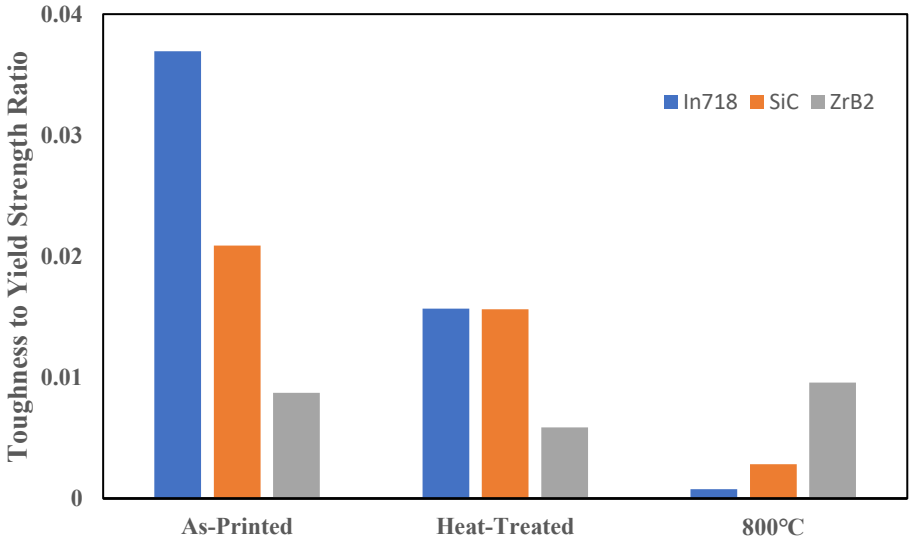

Figure 31: Ratio between toughness and yield strength for In718 and its composites

6.4 Conclusions for In718+ZrB_2 MMC

A new Ni-based MMC, In718+ZrB_2, was fabricated by LPBF of In718 powders mixed with 2 vol% ZrB_2 nanoparticles. Blending of the powders was found to achieve good dispersion through coating of the In718 particles without the need for a milling step. Composite powders displayed good spreadability and printability in an EOS M290 LPBF system using the default parameters designed for In718. Like the previous In718+SiC composite, microstructural analysis of the printed samples revealed decomposition of the majority of the original ceramics during laser melting, which in this case was found to promote the formation of nanoscale (Zr, Ni)-based intermetallics and (Nb, Mo, Cr)-based boride phases. Also like the In718+SiC, inclusion of the ceramics was found to result in a notable reduction in printing defects during solidification, decreasing both the quantity and size of pores compared to the unreinforced In718. This may promote improved fatigue crack resistance in MMC In718 compared to the base metal, and repeated observation of this behavior with a variety of ceramics suggests the potential to use different compositions and concentrations of ceramics to achieve some tunability of this porosity-suppressing effect, which may prove to be of great benefit to the advancement of metal-AM implementation.

In mechanical testing at room temperature, In718+ZrB_2 displayed expected increases in hardness and strength and decrease in ductility. In718+ZrB_2 HT was found to achieve exceptional σ_y and σ_{UTS} of approximately 1350 MPa and 1600 MPa, respectively. These properties may make the MMC an attractive candidate for 3D printed structural applications in cases where the elongation at failure of 5% is not found to be prohibitive. A similar relationship between In718 HT and In718+ZrB_2 HT was also observed at elevated temperatures to at least 650°C, with the reinforced MMC offering about a 100 MPa increase in strength with a slight decrease in elongation (1.5% vs 2%). However, at 800°C this relationship was found to shift much more drastically than it did with the SiC-doped composite. The ZrB_2 MMC demonstrated similar strength to the unreinforced In718 but with a substantial increase in ductility, reaching above 8% elongation at failure.

In considering application for the ARC reactor vacuum vessel, In718+ZrB_2 appears to demonstrate the best combination of properties of the materials considered in this study at

800°C, near the target temperature for the inner vessel wall. The significant increase in toughness at this temperature range even surpasses some reports on wrought In718 [153] and would almost certainly improve creep rupture lifetime. The practicality of using this material will likely depend upon survivability in regions and start-up/cooldown stages with more intermediate temperature regimes, in which elongation is especially low. However, the results achieved in this study are promising with regards to the improvements that can be achieved through utilizing AM technology to produce new MMC materials, and I expect that future studies continuing exploration of MMC compositions and optimizing concentrations and morphologies will have great benefits for the future of structural materials in the energy industry.

Chapter 7

Development of LPBF Process Parameters for Niobium

To this point, discussion in this thesis has focused primarily on the use of AM technology to fabricate MMCs as a method of addressing increasing needs for material survivability in extreme environments. However, this is only a very narrow view of the types of material advancements that may be conceivable through this rapidly developing method of manufacturing. At its very core, AM centers on extreme localization and precision in fabrication. Part designs are broken down to define actions at the scale of tens of μm or even less, incorporating extreme levels of detail in-situ that would require significant efforts in machining and joining to approximate with traditional manufacturing. Modern researchers are now truly beginning to explore the types of extraordinary design choices that are enabled by this level of control in the manufacturing process. To reach the full capabilities of what this technology can accomplish however, significant research efforts are still required, especially with regards to controlling printed material microstructures and expanding the current catalog of materials compatible with AM.

Focusing on this latter need to expand the materials catalog, niobium (Nb) is a metal of particular interest for extreme environment applications that does not yet have an established processing route for AM. Nb is a refractory metal with exceptional melting temperature exceeding 2400°C, nearly 2x higher than that of In718, but with relatively low

density compared to other refractory metals (8.57 g/cm^3). Because of this combination, Nb has been targeted as a potential replacement for nickel superalloys to expand the upper temperature limits of jet engine turbine blades, but its use is currently restricted by extensive oxidation embrittlement at elevated temperatures. Research to combat this oxidation and improve usability is currently being spearheaded by ARPA-E. As one of the research projects under this umbrella, the Hart/Li team at MIT has begun development on a hybrid inkjet/LPBF printer that will allow for functional grading in the fabrication of a Nb-based component. Conceptually, this printer will allow for the deposition of oxidation resistance enhancing additives such as Al, Ti, and Si into a Nb-based powder bed at concentrations that increase towards the surface of the built component, as represented in Figure 32. In this way, high-temperature strength can be maintained through the Nb-based core, an oxidized surface barrier can be implemented to prevent embrittlement, and a smooth gradient between the two can eliminate the sharp interfaces created by simple coatings that might cause stress build up or crack initiation. Before such a design can be utilized, however, a parameter set must be developed that can allow for reliable printing of Nb in an LPBF system.

In this chapter, I will detail my efforts towards developing a process flow to allow for rapid parameter establishment for pure Nb with minimal powder usage in an LPBF system. Reports on printing Nb-based alloys have been extremely limited to this point, both in availability and in scope, and many of the currently available reports have only emerged since the beginning of my work with Nb in 2021 [167,168]. As such, there remains a high need to further develop printability of these materials over a range of AM systems. In the following sections I will describe the scaling process from rapid single layer analysis to multilayer verification and provide details on process optimization guided by machine learning.

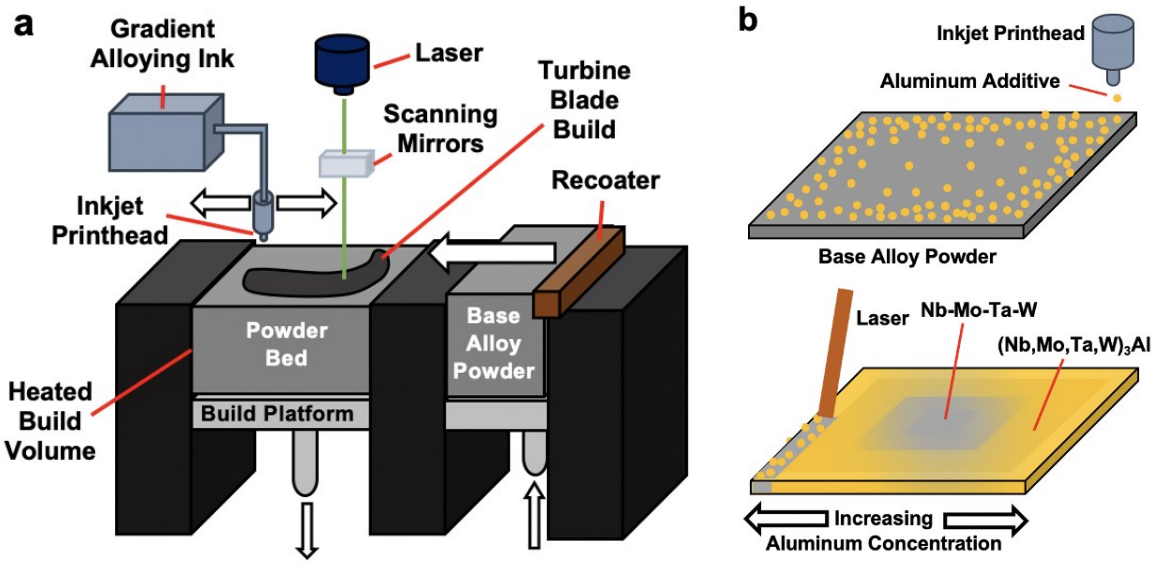

Figure 32: Schematic of the hybrid inkjet/LPBF 3D printer concept under development at MIT

7.1 Rapid Single Layer Parameter Development

In establishing printing parameters for the high-quality production of new materials, simulations and theoretical calculations can often provide a good starting point to minimize cost, materials, and time. However, variations in behavior across different printing systems and minor changes in areas such as material purity can significantly affect the printing process, so there is always some need for experimental validation. In the case of material systems that are not especially well-developed, such as refractory metals, this is especially true, and a wide variety of parameter variations should ideally be explored to narrow down the optimized melting conditions. Due to the limited available knowledge regarding LPBF of Nb-based materials at the onset of this study, such an experimental plan sweeping over a variety of parameters was deemed necessary. Therefore, an approach was chosen that would focus first on parameter exploration using small-scale single-layer rasters, which would allow for quick observation of print surface quality to eliminate obvious cases of under- or over-melting. This approach significantly decreased the amount of time required to prepare a large number of specimens and compare quality. It also dramatically decreased powder requirements, allowing for powder to be spread at the desired thickness only on

the substrate regions where prints are planned, rather than having to fill an entire powder bed with multiple kilograms to attain an even surface for growing layers. This strategy was especially important for Nb, as the current print-quality powder supply chain is limited, leading to particularly high prices and the possibility of long lead times when more powder is required.

To conduct the required single-layer printing, small substrates were prepared with wells machined or chemically etched to the desired layer thicknesses, such as the example shown in Figure 33. By utilizing these wells, powder could be spread across the substrate, and a stiff blade could be scraped across the surface, leaving behind only the powder within the well walls to achieve fixed powder depths. This technique allowed for the preparation of powder layers by hand, enabling the use of laser systems without an automated recoating blade. This was also found to provide a more accurate layer thickness for single layer studies than the traditional use of a flat substrate since most commercial systems require manual measurement and preparation of the initial layer anyway.

Initial single-layer studies were conducted in a custom-made LPBF system at MIT, shown in Figure 34. This system included a controlled-atmosphere build chamber that flooded argon through a gas knife, creating an inert gas environment down to 0.05% O_2 and removing spattered particles from the laser path. A laser with power output up to 500W was equipped for melting processes, and adjustable position of the laser head allowed for tunability of the spot size at the melt surface.

Figure 33: Nb substrate with single-layer prints of Nb powder in machined wells

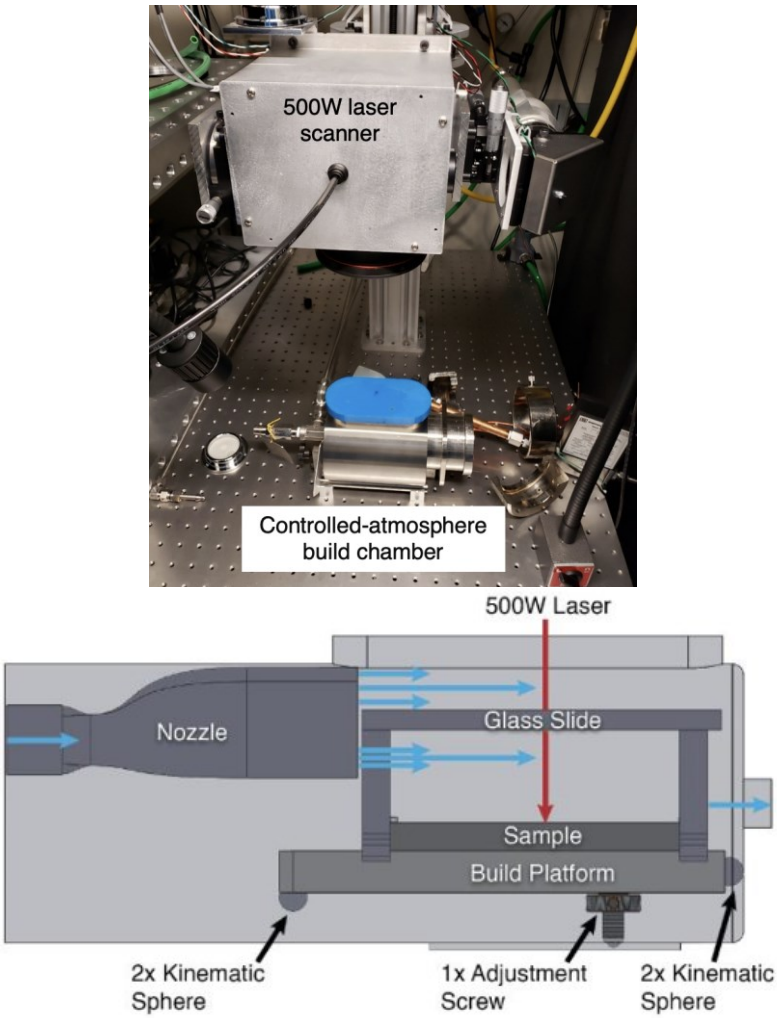

Figure 34: ACAM, a custom LPBF system for single-layer powder or solid material laser melting at MIT

To conduct single-layer print studies, metal substrates were first ground to a flat, even surface and wells were machined to controlled depths using 1/8" end mills in a CNC mill, following which any raised ridges from the milling process were smoothed out. Though initial experiments were conducted with steel plates typical of common LPBF processes, it was quickly determined that mixing of materials played too significant of a role in the structure of the first layer, so Nb plates were purchased from Nexmetal Corp and machined into substrates. 99.9% Nb powder, purchased from American Elements, was spread across the substrates and cleared using a machinist's blade, leaving the powder in the wells behind at the desired layer thickness. This powder-coated substrate was then loaded into the build chamber, moving carefully to avoid disturbing the powder beds. Rasters were generally

performed in 6 mm x 3 mm rectangles, allowing for about 12 sets of parameters to be tested on a single substrate, typically varying laser power and scan speed. Printed samples were then checked under SEM for cracks or unmelted regions that would clearly indicate poor print quality, and high-quality parameter sets were selected for multilayer study. Figure 35 displays 24 SEM images from sample single-layer prints, utilizing the parameters listed in Table 8 in single exposures for the top set of 12 and double exposures for the bottom set. Double exposure was found to promote smoother surface quality in the single-layer samples, but nearly all samples were observed to be covered in globular particles, likely as a result of over-melting promoting melt pool instability and excessive spattering.

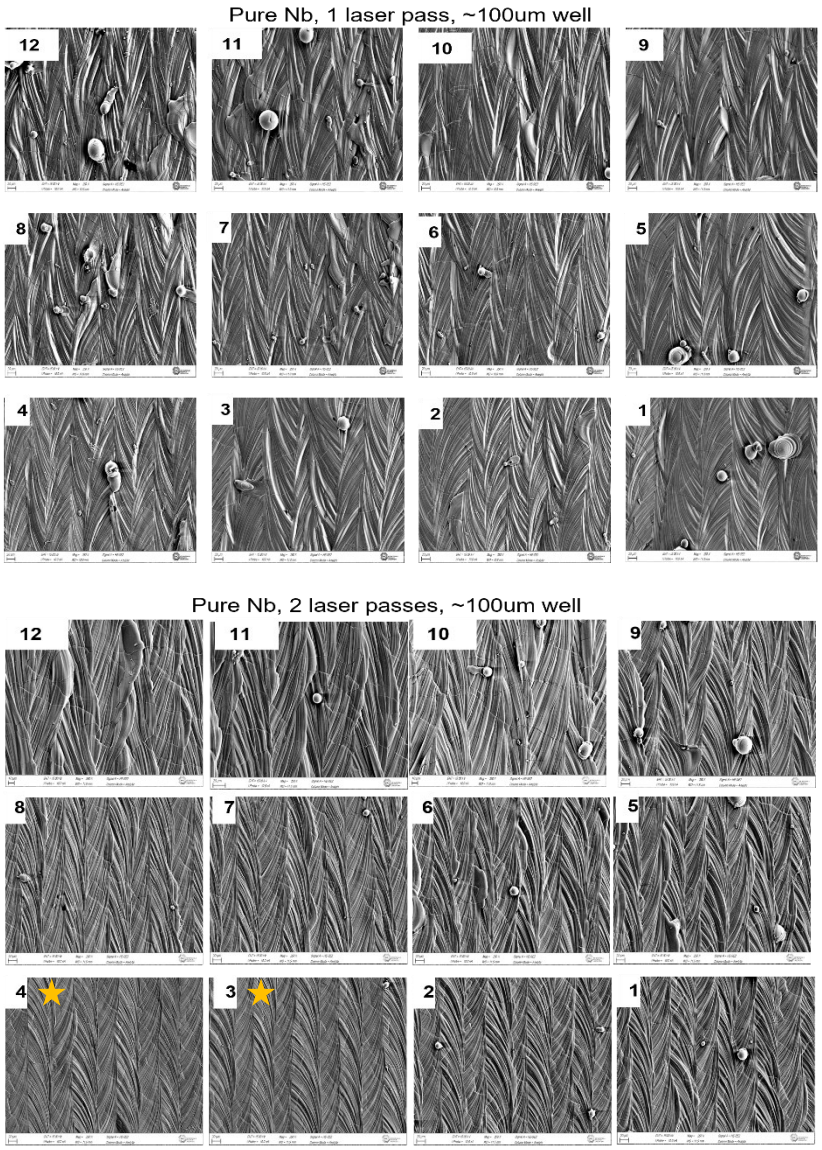

Figure 35: Cross-sectional observation of single layer Nb melting over a range of parameters presented in Table 8

Samples 3 and 4 in the double exposure set, marked with stars, were found to have the most uniform melt tracks and lowest quantity of partially melted particles, so these were selected as the best performing parameter sets from this experiment.

Table 8: Printing parameters for samples in Figure 35

Sample	*1*	*2*	*3*	*4*	*5*	*6*	*7*	*8*	*9*	*10*	*11*	*12*
Power (W)	250	250	250	250	300	300	300	300	350	350	350	350
Scan Speed (mm/s)	100	200	300	400	100	200	300	400	100	200	300	400

7.2 Process Scaling to Multilayer

For multilayer scaling of the pure Nb parameter sets, printing was performed in an EOS M290 commercial LPBF system at UMass Amherst using the same Nb plates for substrates. Initial plans called for use of the most promising parameter sets from single-layer studies for fabrication of 20x20 mm Nb squares with thicknesses of about 2 mm, which was considered adequate to determine if prints would be of high enough quality for further scaling to be reasonable. Based on the single-layer results from Figure 35: Cross-sectional observation of single layer Nb melting over a range of parameters presented in Table 8, two initial parameter sets were selected for testing, which utilized the following parameters: 50 μm layer thickness, 50 μm hatch spacing, 250 W laser power, double exposure per layer, and 1) 300 mm/s or 2) 400 mm/s scan speed. Utilizing the described parameters appeared to result in good quality of melting and solidification for the first few layers, but both sets of samples were experiencing visible surface roughening by 0.5 mm thickness. With continued addition of layers, molten Nb appeared to agglomerate in specific regions of the build rather than spread uniformly across the surface. This resulted in excessive increases in height of the agglomerated regions, which eventually overcame the increases based on designed layer thickness and caused blockage of the recoater blade around 1 mm in thickness (20 layers). Confocal microscope height mapping of the 300 mm/s sample is displayed in Figure 36: (A) Image and (B) Confocal microscope height map of Nb sample prepared at 250W and 300 mm/s, with zoomed in views of the (C) material depleted regions and (D) agglomerated regions. which shows a flat, depleted

region below the expected height of 1 mm and a rough, non-uniform region with columns reaching hundreds of µm above the base surface. SEM images of the sample cross sections revealed large, non-spherical pores within the layers, while mushroom-shaped protrusions appeared at the top. Both defects are typically indicative of lack-of-fusion within the system, suggesting incomplete melting resulted in initial surface defects that disrupted powder and melt pool flow and accumulated over time. This type of behavior is unusually difficult for a 3D printing process, with deviation from optimal printing apparently having drastic effects on the solidification process. This might be related to the combination of high melting temperature and high thermal conductivity resulting in solidification on a faster time scale than would be observed for a material like In718.

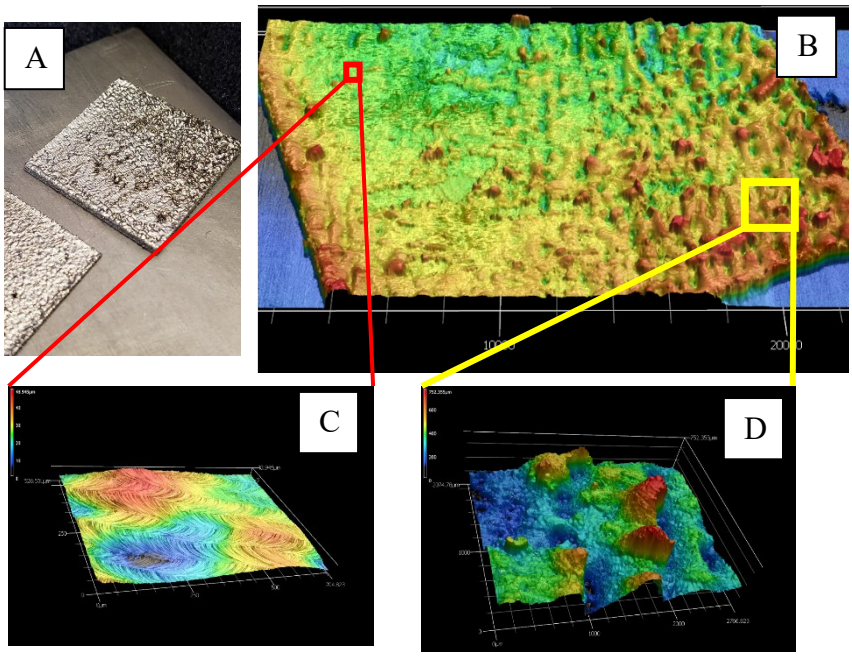

Figure 36: (A) Image and (B) Confocal microscope height map of Nb sample prepared at 250W and 300 mm/s, with zoomed in views of the (C) material depleted regions and (D) agglomerated regions.

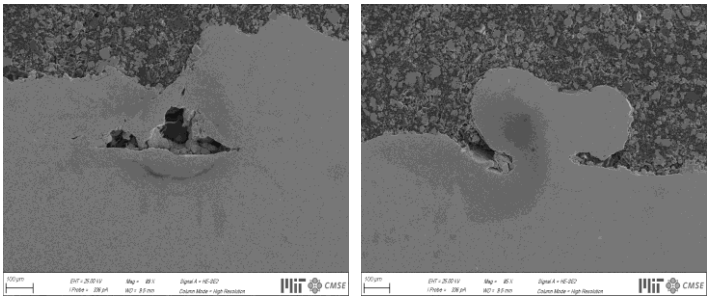

Figure 37: SEM image of 250W, 300 mm/s Nb sample cross-section showing large pores and mushroom-shaped surface defects.

Based on the results of the initial round of multilayer testing, further parameterization iterating around the well-performing single layer conditions was deemed necessary. This parameterization was conducted in three stages: 1) iteration of scan speeds with constant laser power, 2) iteration of power using well performing scan speeds, and 3) measurement of post-solidification height changes for different layer thicknesses. In the first of these, surface roughness measurements for five-layer samples at 250 W revealed improvement in uniformity for scan-speeds of less than 300 mm/s. In the second round, displayed in Figure 38: Parameterization height maps for 5-layer samples of Nb, a 4x4 grid was set up to test scan speeds between 100 and 250 mm/s with laser power between 200W and 350W. In these tests, the combination of 250W and 100 mm/s achieved the best surface roughness. Also of note from these tests was the fact that none of the 200W samples appeared to attain complete melting, regardless of scan speed. The implications of this will be discussed in the next section of this chapter. Finally, in the third round, the use of a 30 µm layer thickness resulted in both the lowest surface roughness and the most consistent change in build height with each layer.

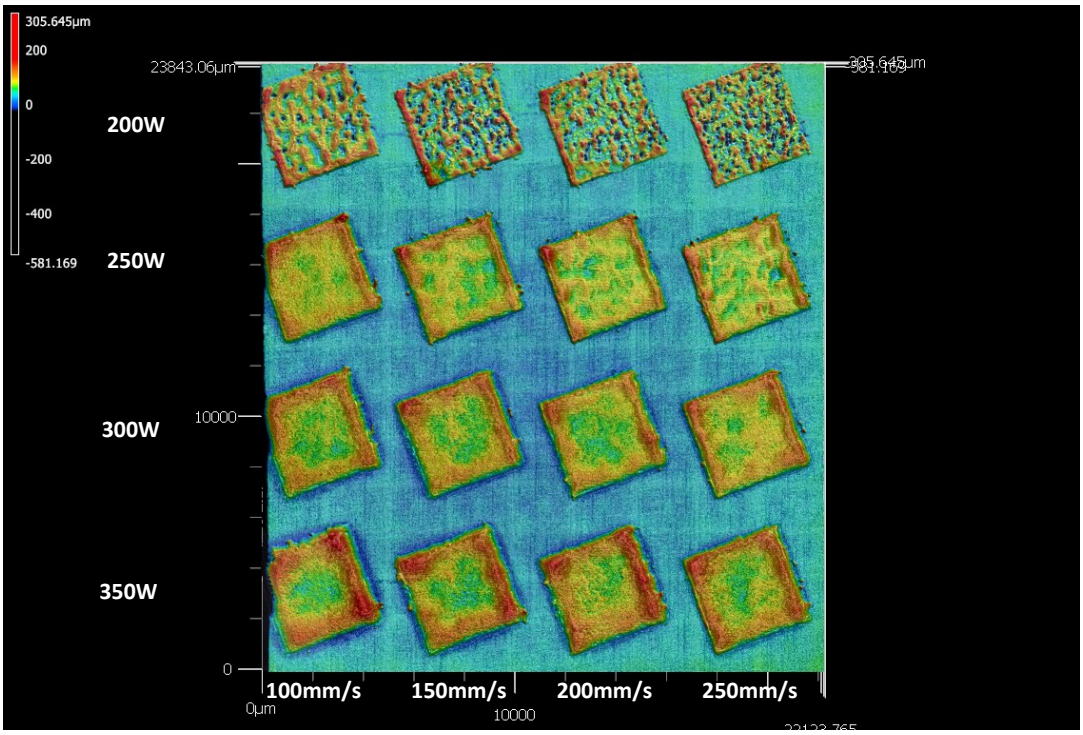

Figure 38: Parameterization height maps for 5-layer samples of Nb

From the parameterization tests described, a new suggested set of parameters was selected: 250 W, 100 mm/s, and 30 µm layer thickness and 50 µm hatch spacing with continued double exposure at each layer. Implementing these parameters in multilayer testing resulted in a dramatic improvement in surface quality, as can be observed in Figure 39. Surface agglomerations that caused recoater blade blockage were nearly entirely suppressed up to 2 mm thickness, with microscopy revealing only a select few surface growths of about 15 µm above the average surface layer whereas the previous prints contained growths reaching up to over 200 µm. Because of this, it was expected that these parameters would have allowed scaling to much greater thicknesses with no severe disruptions, meeting the primary goal of this study to allow for reasonable testing of the gradient printing process. These samples were stopped at 2 mm build height purely for the conservation of powder and time, as it must be noted that the 100 mm/s scan speed, tight hatching distance, and double exposures per layer result in extremely long build times compared to more common materials like the In718. This thickness also allowed for the production of tensile specimens, which reached σ_{UTS} of 300 MPa and an elongation at failure of about 10%, slightly stronger and more brittle than typical wrought niobium, likely due to decreased grain size from the printing process.

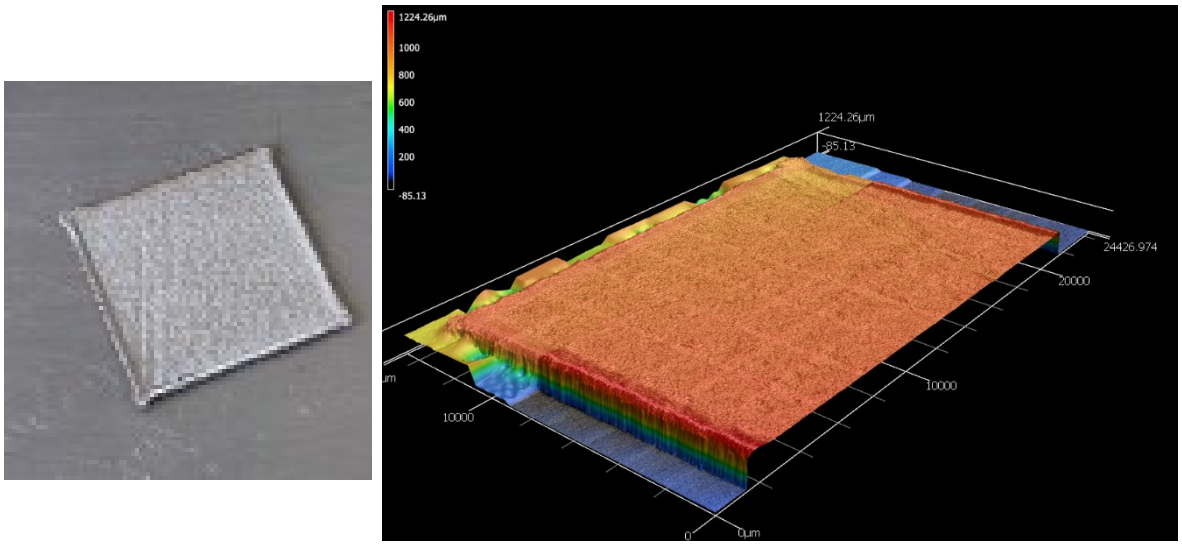

Figure 39: Picture and laser confocal height mapping of Nb printed at 250W and 100 mm/s.

7.3 Process Optimization by Machine Learning

Once I had achieved the first successful print of a multi-mm thick sample of Nb, it was expected that further optimization of the process for even better print quality could be attained. However, I had reached a point of diminishing returns on experimental trial and error, as continued optimization would require smaller step changes over a wider variety of variables. Implementing a machine learning (ML) approach was therefore considered the best option to move forward. While in some cases earlier implementation of this might have been appropriate, approximately 10 layers was deemed to be the minimum requirement to achieve results relevant for further scaling. Considering Nb's observed affinity for surface growth under improper conditions, attempts to accumulate the number of data points necessary for useful ML-based prediction without a prior understanding of adequate printing conditions would certainly have resulted in recoater blade blockages that could impact the results for all the samples in a particular batch.

To create a dataset for initial ML-based prediction of behavior, I performed a new parameter sweep print. I produced 36 initial samples with laser power, scan speed, hatch spacing, and exposure repetition selected as variables to control, making sure to maintain parameter selections within a range of combinations that I was confident could reach at least 10 layers. These samples are shown in Figure 40 along with cross sectional views of representative over-melting and under-melting samples, resulting in keyhole and lack-of-fusion pores, respectively. Print quality could feasibly be evaluated in terms of melt pool geometry, porosity measurement, or surface roughness. However, surface roughness was selected as the evaluation criteria in this round, as the data could A) easily be evaluated for the whole print area rather than a random cross section and B) be collected over a shorter time frame without the need for post-processing of the prints.

Even before measurement of surface roughness and implementation of the dataset for ML-based analysis, it is clear by visual observation that all samples prepared using 200 W laser power have significantly worse surface quality than the remainder, regardless of other variables. In Figure 40 these are the first and fifth rows from the bottom, marked by yellow arrows. Presently, there are several different metrics used to evaluate energy input during

laser melting. The most common of these is the volumetric energy density (VED), calculated as

$$VED = \frac{P}{V * h * t} \left(\frac{J}{mm^3}\right)$$

where P is laser power in W, V is scan speed in mm/s, h is hatch distance in mm, and t is layer thickness in mm. Despite widespread use to describe energy deposition however, VED has been reported to be a poor predictor of melting conditions or track morphology due to its failure to capture melt pool physics [169]. This failure of VED is obvious as it relates to the samples studied here. In Figure 40, the sample marked by the blue arrow was prepared with laser power of 200 W and VED = 666.7 J/mm^3 and has visibly incomplete melting. Meanwhile, the samples enclosed in the blue circle all feature laser powers of 250 W or greater and have VED = 777.8 J/mm^3, 666.7 J/mm^3, and 555.6 J/mm^3 from top to bottom. Despite spanning the range of above, equal to, and below the VED of the incompletely melted sample however, every one of these samples displays successful melting. VED cannot therefore be the cause of this difference.

An alternative measure of energy deposition that has been reported to have more success in prediction of the melting process due to inclusion of thermal and optical properties of the material is called normalized enthalpy [170]. This is defined as

$$\overline{\Delta H} = \frac{\alpha P}{\rho(C\Delta T + L_m)\sqrt{\pi\omega^3 VD}}$$

where α is bulk material absorptivity, P is laser power, ρ is material density, C is specific heat, ΔT is the difference between melting and process temperature, L_m is latent heat of melting, ω is laser spot size, V is scan speed, and D is material thermal diffusivity. Based on this equation, energy deposition should follow a $P/V^{1/2}$ relationship if all other factors are equal for different test conditions on the same material. To evaluate the merit of this relationship, a sample with good melting conditions at 250 W and 200 mm/s was compared to 7 other samples with lower P but equal $P/V^{1/2}$. These samples are shown in Figure 41, and the P and V values utilized are given in Table 9. In this experiment, the same trend was observed where incomplete melting occurred in all samples below 250 W, and the melting can be visually observed to improve from lower laser powers to higher powers approaching 250 W. This behavior rules out a strict reliance on the $P/V^{1/2}$ relationship, but

it does not rule out normalized enthalpy. Rather, I predict that these results indicate a meaningful change in laser absorptivity based on laser power for Nb. In fact, such a phenomenon has been previously reported in stainless steels by Trapp et al [171], who found that laser absorptivity in both powder and plates can exhibit a sharp increase at low laser powers before eventually reaching a plateau. Similar behavior could explain the results found here, and it might be suggested that Nb reaches a critical plateau in laser absorptivity around 250 W for a laser system such as the EOS M290. Such a result can be used to impose a lower practical limit on power for ML-based parameter recommendations, which should help to narrow the possibilities and increase accuracy of the predictions.

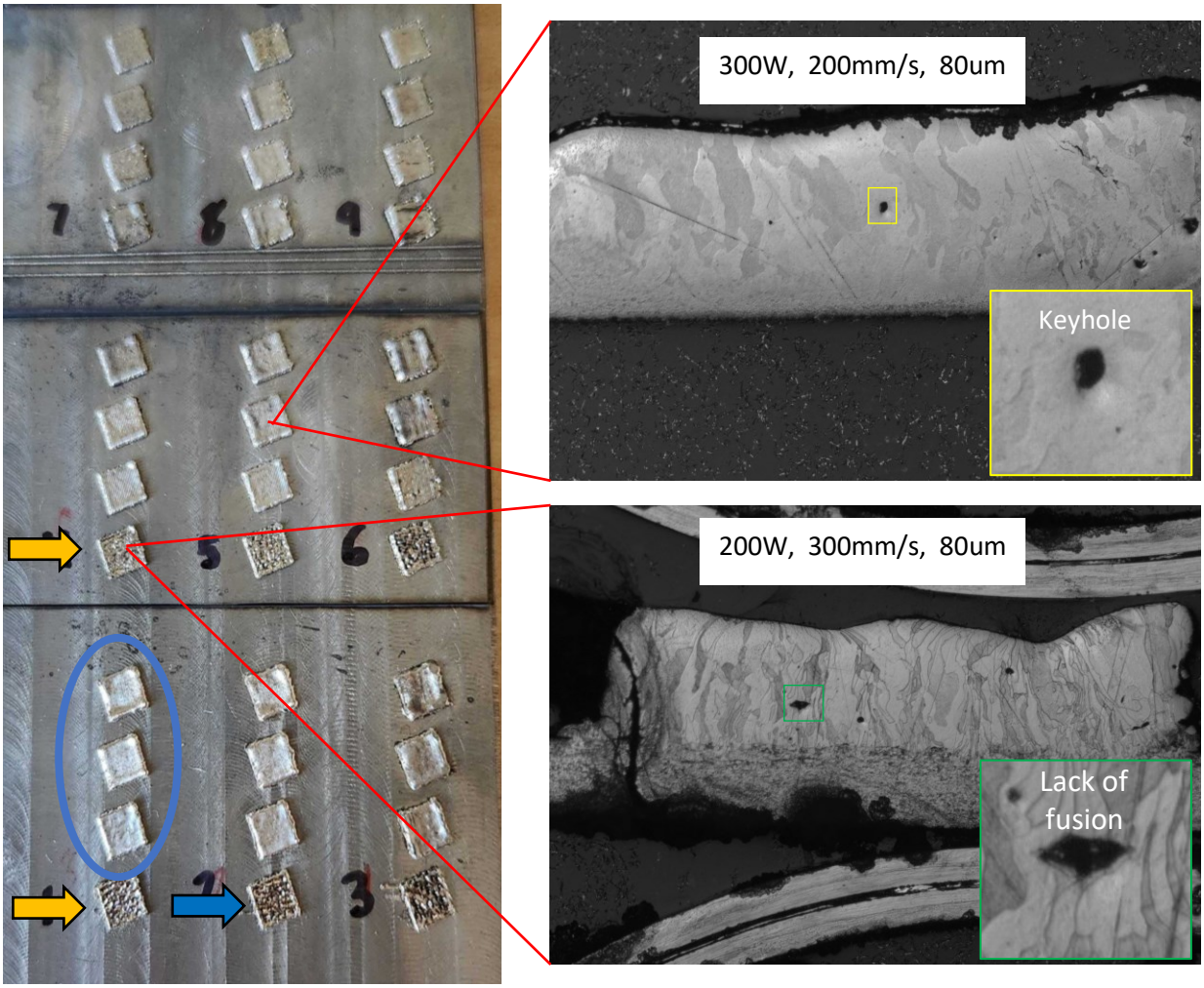

Figure 40: Set of 36 LPBF Nb samples with varying power, scan speed, hatch spacing, and exposure repetition for ML optimization study.

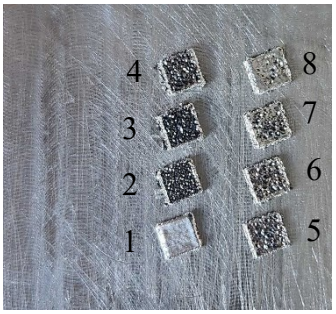

Figure 41: LPBF Nb samples with different power and scan speeds that maintain $P/V^{1/2}$

Table 9: Power and scan speed values for Figure 41

Sample	***1***	***2***	***3***	***4***	***5***	***6***	***7***	***8***
P (W)	250	125	150	175	190	200	210	225
V (mm/s)	200	50	72	98	116	128	141	162

Surface roughness data was gathered for the samples in Figure 40 using a laser confocal microscope, focusing on 2 mm x 2 mm interior sections of the 4 mm x 4 mm samples to avoid edge effects. This data was plugged into a Gaussian regression model previously developed by another member of the Ju Li group at MIT with the specifications of changing power, scan speed, hatch, and exposure repetition recommendations to minimize the surface roughness value. Predicted surface roughness maps based on different combinations of variables are presented in Figure 42, where the whitest regions represent the minimized surface roughness. Overall, laser power was found to have the most significant effect on print quality, followed by hatch distance, scan speed, and then exposure repetition. This seems to be in good agreement with the normalized enthalpy model for melting, though comparison is not obvious since hatch distance and exposure repetition are not variables in the equation. The full recommendations developed by the model to minimize surface roughness were P = 260 W, V = 200 mm/s, and h = 70 μm with no repetition of exposures. While these recommendations might improve with the addition of more data, this approach holds high potential for maximizing printability of both Nb and newly developing Nb-alloys through the parameter translation with normalized enthalpy.

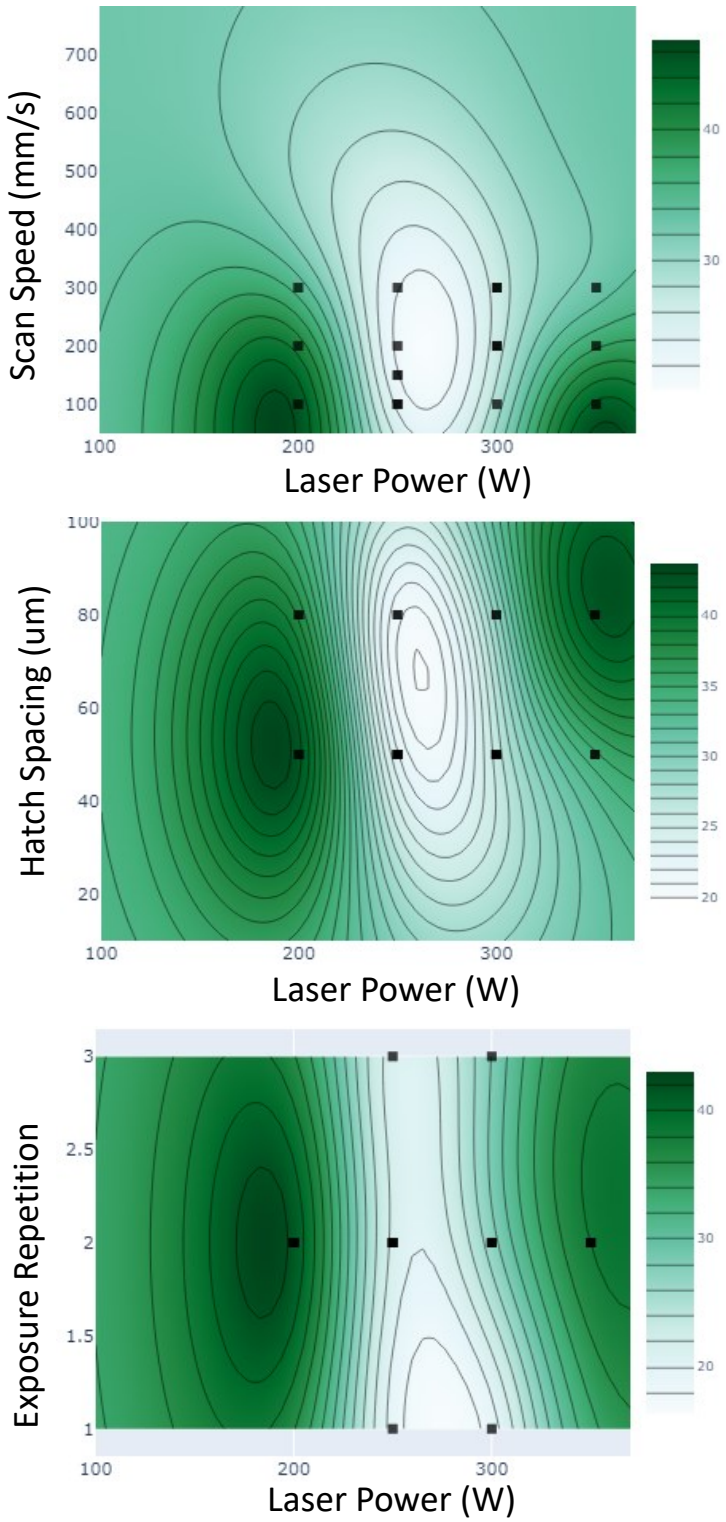

Figure 42: ML-generated predictions for surface roughness based on various laser melting parameters.

Chapter 8

Summary

Paramount among the topics discussed in this thesis is the central idea that the energy industry is presently facing a major turning point. With many suggesting a need for massive decarbonization in the next thirty years, generations worth of high efficiency designs that were deemed infeasible in the past are being dusted off and combined with new advanced concepts to be considered with refreshed enthusiasm. Such designs almost universally come with a need for increased environmental intensity, whether in temperature, stress load, chemical aggression, irradiation, or, in cases like fusion power, all the above. Keeping pace with such needs is presenting modern materials researchers with a level of challenge that has not been seen since at least the space race, if not longer. With this challenge and the ticking clock associated with it in mind, in this thesis I have sought to identify material categories that will be of high value for near-term advancements and to explore methods of addressing the major shortcomings of these materials through the new levels of control enabled by additive manufacturing.

As mentioned, continuously operational fusion technology is expected to present a particularly challenging environment for material survivability, and the designed conditions of such systems become more extreme with each iteration. Plans for the ARC tokamak, based on a collaboration between MIT and Commonwealth Fusion Systems, call for a vacuum vessel that will be able to withstand temperatures reaching almost 800°C while resisting corrosion from FLiBe molten salt and the damage and transmutation effects

of neutron irradiation at 44 dpa per year. Traditionally designed RAFM steels fall short of the temperature goals set for this, while the extremely temperature and radiation resistant SiC/SiC ceramic composites will require huge efforts in joining and manufacturability research to become a practical candidate. V-Cr-Ti alloys were found to be an extremely promising candidate for such applications in the long-term, but immediate implementation of these materials would be prevented by present challenges with high tritium uptake in FLiBe and the lack of a robust supply chain for reliable fabrication at the size-scale required. In the near-term, construction of desperately needed pilot plants to provide the first data truly relevant to full-power continuous fusion will likely require the use of nickel superalloys such as Inconel 718, so I believe that addressing key lifetime limiting effects of these materials, like high-temperature creep resistance, is a critical endeavor.

The formation of metal matrix composites has shown excellent potential to increase the upper temperature limit of materials as is desired, owing to the formation of highly temperature-resistant strengthening ceramic precipitates. Furthermore, increased nano-precipitate dispersion is extremely promising for resistance to the effects of neutrons, as it provides increased sinks for vacancy-interstitial recombination and improved pinning of transmutant He. Development of these materials requires delicate control over ceramic dispersion and matrix solidification. The advancement of additive manufacturing technology is a major breakthrough in this area, as the high-precision process enables endless new metal-ceramic combinations with extraordinary scalability. Through the use of easily processable Al alloys, I have demonstrated the capability for successful inclusion of a variety of ceramics into an FCC-based metal matrix composite. I also displayed the excellent potential of SiC nanowires to serve as reinforcing agents that provide a desirable combination of strength increase and ductility retention.

To directly assess the potential of In718-based composites to enhance properties necessary for extreme environment longevity, I have developed two previously unreported metal-ceramic combinations through laser powder bed fusion that were expected to be highly promising for high-temperature applications: In718+SiC and In718+ZrB_2. Microstructural analysis of these materials revealed that such nano-ceramics could be utilized to promote in-situ formation of new ceramic nanoparticles within the metal matrix at smaller scales than achievable with the original materials. This analysis also displayed

significant suppression of common printing defects with the inclusion of the small quantities of ceramics used, which is expected to improve fatigue lifetime, a major shortcoming of current 3D printed composites. Furthermore, mechanical performance provided key insight into the tunability of properties achievable, with SiC and ZrB_2 reinforcing agents offering tradeoffs in strength increase versus ductility retention. I would especially like to emphasize the results of high-temperature testing with ZrB_2, which demonstrated a drastic increase in ductility and toughness at 800°C, around the target upper limit temperature for ARC. If this material can be practically implemented, these results are expected to raise the upper limit of usability for In718 and significantly improve creep resistance. Further testing and optimization of this and similar MMC combinations is therefore highly recommended.

Lastly, I developed a process flow for the discovery and optimization of LPBF printing parameters for Nb metal, which is expected to be a high-merit material for expanding the upper temperature limits in non-nuclear applications of power generation, such as aviation turbine blades. In addition to the development of MMCs, additive manufacturing enables new complexity in alloy design such as functional grading of composition in space. Such processes will likely enable the production of structures specifically tailored to address issues such as oxidation embrittlement, which currently restricts the high temperature use of Nb. The limited current catalog of materials for which laser melting conditions are well studied is a major bottleneck for the implementation of these techniques to new materials though. As such, rapid exploration of parameters that provide high-quality, scalable use of new metals in printing systems, especially refractory metals like Nb, is an essential undertaking that I have contributed to and that should be expanded in near-term research.

Bibliography

[1] M. Greenwald, Fusion Energy: Research at the Crossroads, Joule. 3 (2019) 1175–1179. https://doi.org/10.1016/j.joule.2019.03.013.

[2] B.N. Sorbom, J. Ball, T.R. Palmer, F.J. Mangiarotti, J.M. Sierchio, P. Bonoli, C. Kasten, D.A. Sutherland, H.S. Barnard, C.B. Haakonsen, J. Goh, C. Sung, D.G. Whyte, ARC: A compact, high-field, fusion nuclear science facility and demonstration power plant with demountable magnets, Fusion Engineering and Design. 100 (2015) 378–405. https://doi.org/10.1016/J.FUSENGDES.2015.07.008.

[3] V. Barabash, A. Peacock, S. Fabritsiev, G. Kalinin, S. Zinkle, A. Rowcliffe, J.W. Rensman, A.A. Tavassoli, P. Marmy, P.J. Karditsas, F. Gillemot, M. Akiba, Materials challenges for ITER - Current status and future activities, Journal of Nuclear Materials. (2007). https://doi.org/10.1016/j.jnucmat.2007.03.017.

[4] J.W. Coenen, S. Antusch, M. Aumann, W. Biel, J. Du, J. Engels, S. Heuer, A. Houben, T. Hoeschen, B. Jasper, F. Koch, J. Linke, A. Litnovsky, Y. Mao, R. Neu, G. Pintsuk, J. Riesch, M. Rasinski, J. Reiser, M. Rieth, A. Terra, B. Unterberg, T. Weber, T. Wegener, J.-H. You, C. Linsmeier, Materials for DEMO and reactor applications—boundary conditions and new concepts, Phys Scr. T167 (2016) 014002. https://doi.org/10.1088/0031-8949/2016/T167/014002.

[5] R.C. Reed, The Superalloys fundamentals and applications, 2006. https://doi.org/10.1017/CBO9780511541285.

[6] C.T. Sims, N.S. Stoloff, W.C. Hagel, Superalloys II, in: Superalloys II, 1987.

[7] J.C. Williams, E.A. Starke, Progress in structural materials for aerospace systems, Acta Mater. (2003). https://doi.org/10.1016/j.actamat.2003.08.023.

[8] G. Smith, L. Shoemaker, Advanced nickle alloys for coal-fired boiler tubing, Advanced Materials and Processes. 162 (2004) 23–26.

[9] J. Irby, D. Gwinn, W. Beck, B. LaBombard, R. Granetz, R. Vieira, Alcator C-Mod design, engineering, and disruption research, Fusion Science and Technology. (2007). https://doi.org/10.13182/FST07-A1433.

[10] G.E. Totten, 23.12.1 Alloy 718, in: ASM Handbook Volume 4E - Heat Treating of Nonferrous Alloys, ASM International, 2016.

[11] G.R. Odette, S.J. Zinkle, 9. Ni-Based Alloys for Reactor Internals and Steam Generator Applications, in: Structural Alloys for Nuclear Energy Applications, Elsevier, 2019.

[12] P. Beardmore, R.G. Davies, T.L. Johnston, On The Temperature Dependence of the Flow Stress of Nickel-Base Alloys, Transactions of The Metallurgical Society of AIME. 245 (1969) 1537–1545.

[13] M. Ugolotti, M. Sharma, Z. Williams, M. Owen, J. Ouwerkerk, S. Balachandar, M.G. Turner, Cooling System for 0.1 kN Thrust Micro-Engines: Concept Design Using Additive Manufacturing, in: 58th AIAA/ASCE/AHS/ASC Structures, Structural Dynamics, and Materials Conference, Grapevine, Texas, 2017: p. 220.4.3. https://doi.org/10.2514/6.2017-1541.

[14] High-temperature high-strength nickel-base alloys: A practical guide to the use of nickel-containing alloys - No 393, 2020.

[15] Pub. No. SMC-045, 2007.

[16] M. Kutz, 8.2.2 Mechanical Behavior, in: Mechanical Engineers' Handbook, Volume 1 - Materials and Engineering Mechanics (4th Edition), John Wiley & Sons, 2015.

[17] F.A. Garner, B.M. Oliver, L.R. Greenwood, The dependence of helium generation rate on nickel content of Fe-Cr-Ni alloys irradiated to high dpa levels in EBR-II, Journal of Nuclear Materials. 258–263 (1998) 1740–1744. https://doi.org/10.1016/S0022-3115(98)00297-9.

[18] H. Ullmaier, The influence of helium on the bulk properties of fusion reactor structural materials, Nuclear Fusion. 24 (1984) 1039. https://doi.org/10.1088/0029-5515/24/8/009.

[19] B.H. Sencer, G.M. Bond, F.A. Garner, M.L. Hamilton, B.M. Oliver, L.E. Thomas, S.A. Maloy, W.F. Sommer, M.R. James, P.D. Ferguson, Microstructural evolution of Alloy 718 at high helium and hydrogen generation rates during irradiation with 600–800 MeV protons, Journal of Nuclear Materials. 283–287 (2000) 324–328. https://doi.org/https://doi.org/10.1016/S0022-3115(00)00308-1.

[20] G.S. Was, Irradiation-Induced Voids and Bubbles, in: Fundamentals of Radiation Materials Science: Metals and Alloys, Springer New York, New York, NY, 2017: pp. 379–484. https://doi.org/10.1007/978-1-4939-3438-6_8.

[21] F. Carsughi, H. Derz, P. Ferguson, G. Pott, W. Sommer, H. Ullmaier, Investigations on Inconel 718 irradiated with 800 MeV protons, Journal of Nuclear Materials. 264 (1999) 78–88. https://doi.org/https://doi.org/10.1016/S0022-3115(98)00475-9.

[22] H.K. Zhang, Z. Yao, M.R. Daymond, M.A. Kirk, Elevated temperature irradiation damage in CANDU spacer material Inconel X-750, Journal of Nuclear Materials. 445 (2014) 227–234. https://doi.org/https://doi.org/10.1016/j.jnucmat.2013.11.008.

[23] J.R. Keiser, Compatibility Studies of Potential Molten-Salt Breeder Reactor Materials in Molten Fluoride Salts, 1977.

[24] M. Kondo, T. Nagasaka, T. Muroga, A. Sagara, N. Noda, Q. Xu, D. Ninomiya, N. Masaru, A. Suzuki, T. Terai, High performance corrosion resistance of nickel-based alloys in molten salt flibe, Fusion Science and Technology. (2009). https://doi.org/10.13182/FST09-A8900.

[25] B. Bocci, ARC reactor: Activation analysis of the liquid blanket and structural materials for the vacuum vessel, 2018.

[26] B. Bocci, Z. Hartwig, S. Segantin, R. Testoni, D. Whyte, M. Zucchetti, ARC reactor materials: Activation analysis and optimization, Fusion Engineering and Design. 154 (2020) 111539. https://doi.org/10.1016/j.fusengdes.2020.111539.

[27] H. Qi, Review of INCONEL 718 Alloy: Its History, Properties, Processing and Developing Substitutes, Journal of Materials Engineering. 2 (2012) 92–100.

[28] A. Lingenfelter, Welding of Inconel Alloy 718: A Historical Overview, 1989.

[29] P. Kumar, P. Chakravarthy, S.K. Manwatkar, S.V.S.N. Murty, Effect of Scan Speed and Laser Power on the Nature of Defects, Microstructures and Microhardness of 3D-Printed Inconel 718 Alloy, J Mater Eng Perform. 30 (2021) 7057–7070. https://doi.org/10.1007/s11665-021-06163-8.

[30] G. Bertali, Y. Wang, J.J.H. Lim, F. Scenini, C.J. Long, P.D. Freyer, M.G. Burke, Microstructural Analysis of 3D-Printed Alloy 718, Microscopy and Microanalysis. 21 (2015) 463–464. https://doi.org/10.1017/S1431927615003116.

[31] E. Tekoğlu, A.D. O'Brien, J. Liu, B. Wang, S. Kavak, Y. Zhang, S.Y. Kim, S. Wang, D. Ağaoğulları, W. Chen, A.J. Hart, J. Li, Strengthening additively manufactured Inconel 718 through in-situ formation of nanocarbides and silicides, Addit Manuf. 67 (2023) 103478. https://doi.org/10.1016/j.addma.2023.103478.

[32] S.J. Zinkle, G.S. Was, Materials challenges in nuclear energy, Acta Mater. 61 (2013) 735–758. https://doi.org/10.1016/j.actamat.2012.11.004.

[33] Assessment and management of ageing of major nuclear power plant components important to safety: PWR pressure vessels, 1999.

[34] G.S. Was, S. Ukai, G.R. Odette, S.J. Zinkle, 8. Austenitic Stainless Steels, Structural Alloys for Nuclear Energy Applications. (2019). https://app.knovel.com/hotlink/khtml/id:kt012213K1/structural-alloys-nuclear/structural-austenitic.

[35] J. Irby, D. Gwinn, W. Beck, B. LaBombard, R. Granetz, R. Vieira, Alcator C-Mod design, engineering, and disruption research, Fusion Science and Technology. (2007). https://doi.org/10.13182/FST07-A1433.

[36] R.L. Klueh, D.R. Harries, High-Chromium Ferritic and Martensitic Steels for Nuclear Applications, ASTM International, 100 Barr Harbor Drive, PO Box C700, West Conshohocken, PA 19428-2959, 2001. https://doi.org/10.1520/MONO3-EB.

[37] P. Spatig, J.-C. Chen, G.R. Odette, S.J. Zinkle, 11.2 Applications of the Ferritic/Martensitic Steels in Generation IV Nuclear Systems and Fusion Reactors, Structural Alloys for Nuclear Energy Applications. (2019). https://app.knovel.com/hotlink/khtml/id:kt012215Z2/structural-alloys-nuclear/applications-ferritic.

[38] D.S. Gelles, Development of Martensitic Steels for High Neutron Damage Applications, Journal of Nuclear Materials. 239 (1996) 99–106.

[39] Y. Shan, P. Hu, W. Yan, W. Wang, W. Sha, K. Yang, Nitride-Strengthened Reduced Activation Ferritic/Martensitic Steels, in: Supplemental Proceedings: Volume 1: Materials Processing and Energy Materials 5.3.1, The Minerals, Metals & Materials Society, 2011: pp. 42–50.

[40] S. Jitsukawa, M. Tamura, B. van der Schaaf, R.L. Klueh, A. Alamo, C. Petersen, M. Schirra, P. Spaetig, G.R. Odette, A.A. Tavassoli, K. Shiba, A. Kohyama, A. Kimura,

Development of an extensive database of mechanical and physical properties for reduced-activation martensitic steel F82H, Journal of Nuclear Materials. 307–311 (2002) 179–186. https://doi.org/https://doi.org/10.1016/S0022-3115(02)01075-9.

[41] M. Rieth, M. Schirra, A. Falkenstein, P. Graf, S. Heger, H. Kempe, R. Lindau, H. Zimmerman, EUROFER 97 Tensile, charpy, creep and structural tests (FZKA--6911), 2003.

[42] K. Shiba, H. Tanigawa, T. Hirose, H. Sakasegawa, S. Jitsukawa, Long-term properties of reduced activation ferritic/martensitic steels for fusion reactor blanket system, Fusion Engineering and Design. 86 (2011) 2895–2899. https://doi.org/10.1016/j.fusengdes.2011.06.005.

[43] E. Daum, K. Ehrlich, M. Schirra, Proceedings of the second milestone meeting of European laboratories on the development of ferritic/martensitic steels for fusion technology, in: 1997.

[44] H. Tanigawa, E. Gaganidze, T. Hirose, M. Ando, S.J. Zinkle, R. Lindau, E. Diegele, Development of benchmark reduced activation ferritic/martensitic steels for fusion energy applications, Nuclear Fusion. 57 (2017) 092004.

[45] E. Gaganidze, H.-C. Schneider, B. Dafferner, J. Aktaa, High-dose neutron irradiation embrittlement of RAFM steels, Journal of Nuclear Materials. 355 (2006) 83–88. https://doi.org/https://doi.org/10.1016/j.jnucmat.2006.04.014.

[46] E. Gaganidze, B. Dafferner, H. Ries, R. Rolli, H.-C. Schneider, J. Aktaa, Irradiation Programme HFR Phase IIb (SPICE), Impact Testing on up to 16.3 dpa Irradiated RAFM Steels, 2008.

[47] E. Materna-Morris, A. Möslang, H.-C. Schneider, Tensile and low cycle fatigue properties of EUROFER97-steel after 16.3dpa neutron irradiation at 523, 623 and 723K, Journal of Nuclear Materials. 442 (2013) S62–S66. https://doi.org/https://doi.org/10.1016/j.jnucmat.2013.03.038.

[48] E. Gaganidze, J. Aktaa, Assessment of neutron irradiation effects on RAFM steels, Fusion Engineering and Design. 88 (2013) 118–128. https://doi.org/https://doi.org/10.1016/j.fusengdes.2012.11.020.

[49] K. Baral, S. San, R. Sakidja, A. Couet, K. Sridharan, W.-Y. Ching, Temperature-Dependent Properties of Molten Li2BeF4 Salt Using Ab Initio Molecular

Dynamics., ACS Omega. 6 (2021) 19822–19835. https://doi.org/10.1021/acsomega.1c02528.

[50] T. Muroga, T. Nagasaka, M. Kondo, A. Sagara, N. Noda, A. Suzuki, T. Terai, Compatibility of Reduced Activation Ferritic/Martensitic Steels with Liquid Breeders, in: 22nd IAEA Fusion Energy Conference, 2008.

[51] H. Nishimura, T. Terai, M. Yamawaki, S. Tanaka, A. Sagara, O. Motojima, Compatibility of ferritic steels with Li2BeF4 molten salt breeder, Journal of Nuclear Materials. 307–311 (2002) 1355–1359. https://doi.org/https://doi.org/10.1016/S0022-3115(02)01123-6.

[52] B. Bocci, Z. Hartwig, S. Segantin, R. Testoni, D. Whyte, M. Zucchetti, ARC reactor materials: Activation analysis and optimization, Fusion Engineering and Design. 154 (2020) 111539. https://doi.org/10.1016/j.fusengdes.2020.111539.

[53] B. Bocci, ARC reactor: Activation analysis of the liquid blanket and structural materials for the vacuum vessel, 2018.

[54] R.J. Kurtz, G.R. Odette, Zinkle Steven J, 3. Overview of Reactor Systems and Operational Environments for Structural Materials in Fusion Reactors, in: Structural Alloys for Nuclear Energy Applications, Elsevier, 2019. https://app.knovel.com/hotlink/khtml/id:kt01220Z73/structural-alloys-nuclear/structural-overview-reactor.

[55] R.J. Pearson, On the Availability, Supply & Use of Critical Natural Resource for the Realisation of the Fusion Industry, 2022.

[56] Z.S.J. Odette G. Robert, 3.5.3 Vanadium Alloys, Structural Alloys for Nuclear Energy Applications. (2019). https://app.knovel.com/hotlink/khtml/id:kt01220ZJ1/structural-alloys-nuclear/vanadium-alloys.

[57] S.J. Zinkle, Advanced materials for fusion technology, Fusion Engineering and Design. 74 (2005) 31–40.

[58] T. Muroga, J.M. Chen, V.M. Chernov, R.J. Kurtz, M. Le Flem, Present status of vanadium alloys for fusion applications, Journal of Nuclear Materials. 455 (2014) 263–268. https://doi.org/10.1016/j.jnucmat.2014.06.025.

[59] B.A. Loomis, H.M. Chung, L.J. Nowicki, D.L. Smith, Effects of neutron irradiation and hydrogen on ductile-brittle transition temperatures of V-Cr-Ti alloys, Journal of Nuclear Materials. 212–215 (1994) 799–803.

[60] J.M. Chen, V.M. Chernov, R.J. Kurtz, T. Muroga, Overview of the vanadium alloy researches for fusion reactors, Journal of Nuclear Materials. 417 (2011) 289–294. https://doi.org/10.1016/j.jnucmat.2011.02.015.

[61] I.R. Kirillov, G.E. Shatalov, YU.S. Strebkov, RF TBMs for ITER tests, Fusion Engineering and Design. 81 (2006) 425–432. https://doi.org/10.1016/j.fusengdes.2005.05.004.

[62] T.S. Bray, H. Tsai, L.J. Nowicki, M.C. Billone, D.L. Smith, W.R. Johnson, P.W. Trester, Tensile and impact properties of V–4Cr–4Ti alloy heats 832665 and 832864, Journal of Nuclear Materials. 283–287 (2000) 633–636. https://doi.org/10.1016/S0022-3115(00)00229-4.

[63] A.F. Rowcliffe, S.J. Zinkle, D.T. Hoelzer, Effect of strain rate on the tensile properties of unirradiated and irradiated V–4Cr–4Ti, Journal of Nuclear Materials. 283–287 (2000) 508–512. https://doi.org/10.1016/S0022-3115(00)00311-1.

[64] H.M. Chung, A. Loomis, D.L. Smith, Properties of V-4Cr-4Ti for Application as Fusion Reactor Structural Components, in: Third International Symposium on Fusion Nuclear Technology, Los Angeles, 1994.

[65] Properties and Selection: Nonferrous Alloys and Special-Purpose Materials, in: Metals Handbook, 9th ed., ASM International, 1990. https://doi.org/10.31399/asm.hb.v02.9781627081627.

[66] M. Li, S.J. Zinkle, Deformation Mechanism Maps of Unirradiated and Irradiated V-4Cr-4Ti, J ASTM Int. 2 (2005).

[67] M. Li, T. Nagasaka, D.T. Hoelzer, M.L. Grossbeck, S.J. Zinkle, T. Muroga, K. Fukumoto, H. Matsui, M. Narui, Biaxial thermal creep of two heats of V4Cr4Ti at 700 and 800°C in a liquid lithium environment, Journal of Nuclear Materials. 367–370 (2007) 788–793. https://doi.org/10.1016/j.jnucmat.2007.03.081.

[68] H.M. Chung, B.A. Loomis, D.L. Smith, Creep properties of vanadium-base alloys, Journal of Nuclear Materials. 212–215 (1994) 772–777. https://doi.org/10.1016/0022-3115(94)90161-9.

[69] K. Fukumoto, M. Sugiyama, H. Matsui, Features of dislocation channeling in neutron-irradiated V–(Fe, Cr)–Ti alloy, Journal of Nuclear Materials. 367–370 (2007) 829–833. https://doi.org/10.1016/j.jnucmat.2007.03.075.

[70] M.L. Hamilton, M.B. Toloczko, Effect of low temperature irradiation on the mechanical properties of ternary V–Cr–Ti alloys as determined by tensile tests and shear punch tests, Journal of Nuclear Materials. 283–287 (2000) 488–491. https://doi.org/10.1016/S0022-3115(00)00227-0.

[71] T. Muroga, Vanadium Alloys for Fusion Blanket Applications, Mater Trans. 46 (2005) 405–411.

[72] S.-N. Jiang, F.-J. Zhou, G.-W. Zhang, X.-O. Yi, C.-W. Yu, X.-J. Wang, W.-F. Rao, Recent progress of vanadium-based alloys for fusion application, Tungsten. 3 (2021) 382–392. https://doi.org/10.1007/s42864-021-00107-4.

[73] M. Satou, T. Chuto, K. Abe, Improvement in post-irradiation ductility of neutron irradiated V–Ti–Cr–Si–Al–Y alloy and the role of interstitial impurities, Journal of Nuclear Materials. 283–287 (2000) 367–371. https://doi.org/10.1016/S0022-3115(00)00077-5.

[74] R.J. Kurtz, K. Abe, V.M. Chernov, D.T. Hoelzer, H. Matsui, T. Muroga, G.R. Odette, Recent progress on development of vanadium alloys for fusion, Journal of Nuclear Materials. 329–333 (2004) 47–55. https://doi.org/10.1016/j.jnucmat.2004.04.299.

[75] M. Fujiwara, K. Takanashi, M. Satou, A. Hasegawa, K. Abe, K. Kakiuchi, T. Furuya, Influence of Cr, Ti concentrations on oxidation and corrosion resistance of V–Cr–Ti type alloys, Journal of Nuclear Materials. 329–333 (2004) 452–456. https://doi.org/10.1016/j.jnucmat.2004.04.090.

[76] A.C. Klein, D.K. Sze, FLiBe-Vanadium Alloy System Corrosion Product Radiation Hazards Analysis, Fusion Technology. 10 (1986).

[77] O.K. Chopra, D.L. Smith, P.F. Tortorelli, J.H. DeVan, D.K. Sze, Liquid-Metal Corrosion, Fusion Technology. 8 (1985).

[78] J. Chen, T. Muroga, S. Qiu, Y. Xu, Y. Den, Z. Xu, Hydrogen embrittlement of a V4Cr4Ti alloy evaluated by different test methods, Journal of Nuclear Materials. 325 (2004) 79–86. https://doi.org/10.1016/j.jnucmat.2003.10.014.

[79] D.K. Sze, IPFR, Integrated Pool Fusion Reactor Concept, Fusion Technology. 10 (1986).

[80] W.R. Johnson, J.P. Smith, Fabrication of a 1200 kg ingot of V–4Cr–4Ti alloy for the DIII–D radiative divertor program, Journal of Nuclear Materials. 258–263 (1998) 1425–1430. https://doi.org/10.1016/S0022-3115(98)00209-8.

[81] T. Nagasaka, T. Muroga, W. Yican, X. Zengyu, M. Imamura, Low activation characteristics of several heats of V-4Cr-4Ti ingot, Japan Society of Plasma Science and Nuclear Fusion Research, Japan, 2003. http://inis.iaea.org/search/search.aspx?orig_q=RN:34082166.

[82] M. Le Flem, J.-M. Gentzbittel, P. Wident, Assessment of a European V–4Cr–4Ti alloy – CEA-J57, Journal of Nuclear Materials. 442 (2013) S325–S329. https://doi.org/10.1016/j.jnucmat.2013.02.072.

[83] H.Y. Fu, J.M. Chen, P.F. Zheng, T. Nagasaka, T. Muroga, Z.D. Li, S. Cui, Z.Y. Xu, Fabrication using electron beam melting of a V–4Cr–4Ti alloy and its thermo-mechanical strengthening study, Journal of Nuclear Materials. 442 (2013) S336–S340. https://doi.org/10.1016/j.jnucmat.2013.01.337.

[84] Z.S.J. Odette G. Robert, 3.5.4 SiCF/SiC Composites, in: Structural Alloys for Nuclear Energy Applications, Elsevier, 2019. https://app.knovel.com/hotlink/khtml/id:kt01220ZK1/structural-alloys-nuclear/sicf-sic-composites.

[85] T. Koyanagi, Y. Katoh, T. Nozawa, L.L. Snead, S. Kondo, C.H. Henager, M. Ferraris, T. Hinoki, Q. Huang, Recent progress in the development of SiC composites for nuclear fusion applications, Journal of Nuclear Materials. 511 (2018) 544–555. https://doi.org/10.1016/j.jnucmat.2018.06.017.

[86] T. Noda, Advanced SiC-SiC Composites for Nuclear Application, in: Handbook of Advanced Ceramics and Composites, Springer International Publishing, Cham, 2020: pp. 641–666. https://doi.org/10.1007/978-3-030-16347-1_20.

[87] S. Somiya, 3.1.6 Extreme Environment Application, Handbook of Advanced Ceramics - Materials, Applications, Processing, and Properties (2nd Edition). (2013). https://app.knovel.com/hotlink/khtml/id:kt00BWTPZ2/handbook-advanced-ceramics/extreme-environment-application.

[88] K. Yoshida, T. Yano, Room and high-temperature mechanical and thermal properties of SiC fiber-reinforced SiC composite sintered under pressure, Journal of Nuclear Materials. 283–287 (2000) 560–564. https://doi.org/10.1016/S0022-3115(00)00212-9.

[89] A.S. Almansour, G.N. Morscher, Tensile creep behavior of SiCf/SiC ceramic matrix minicomposites, J Eur Ceram Soc. 40 (2020) 5132–5146. https://doi.org/10.1016/j.jeurceramsoc.2020.07.012.

[90] L.L. Snead, R.H. Jones, A. Kohyama, P. Fenici, Status of silicon carbide composites for fusion, Journal of Nuclear Materials. 233–237 (1996) 26–36. https://doi.org/10.1016/S0022-3115(96)00318-2.

[91] T. Hinoki, L.L. Snead, Y. Katoh, A. Hasegawa, T. Nozawa, A. Kohyama, The effect of high dose/high temperature irradiation on high purity fibers and their silicon carbide composites, Journal of Nuclear Materials. 307–311 (2002) 1157–1162. https://doi.org/10.1016/S0022-3115(02)01054-1.

[92] Y. Katoh, L.L. Snead, C.H. Henager, T. Nozawa, T. Hinoki, A. Iveković, S. Novak, S.M. Gonzalez de Vicente, Current status and recent research achievements in SiC/SiC composites, Journal of Nuclear Materials. 455 (2014) 387–397. https://doi.org/10.1016/j.jnucmat.2014.06.003.

[93] T. Nozawa, Y. Katoh, L.L. Snead, The effect of neutron irradiation on the fiber/matrix interphase of silicon carbide composites, Journal of Nuclear Materials. 384 (2009) 195–211. https://doi.org/10.1016/j.jnucmat.2008.11.015.

[94] I.M. Low, 24.2.4 Radiation Effects in SiC/SiC Ceramic Matrix Composite, Advances in Ceramic Matrix Composites (2nd Edition). (2018). https://app.knovel.com/hotlink/khtml/id:kt011Q2XH2/advances-in-ceramic-matrix/advances-i-radiation-effects.

[95] M.E. Sawan, Y. Katoh, L.L. Snead, Transmutation of silicon carbide in fusion nuclear environment, Journal of Nuclear Materials. 442 (2013) S370–S375. https://doi.org/10.1016/j.jnucmat.2012.11.018.

[96] R.M. Van Ginhoven, A. Chartier, C. Meis, W.J. Weber, L. René Corrales, Theoretical study of helium insertion and diffusion in 3C-SiC, Journal of Nuclear Materials. 348 (2006) 51–59. https://doi.org/10.1016/j.jnucmat.2005.09.006.

[97] J.J. Lee, S.S. Raiman, Y. Katoh, T. Koyanagi, C.I. Contescu, X. Hu, Y. Yang, Chemical compatibility of silicon carbide in molten fluoride salts for the fluoride salt-cooled high temperature reactor, Journal of Nuclear Materials. 524 (2019) 119–134. https://doi.org/10.1016/j.jnucmat.2019.07.001.

[98] W. Xue, X. Yang, J. Qiu, H. Liu, B. Zhao, H. Xia, X. Zhou, P. Huai, H. Liu, J. Wang, Effects of Cr3+ on the corrosion of SiC in LiF–NaF–KF molten salt, Corros Sci. 114 (2017) 96–101. https://doi.org/10.1016/j.corsci.2016.10.026.

[99] R.A. Causey, W.R. Wampler, The use of silicon carbide as a tritium permeation barrier, Journal of Nuclear Materials. 220–222 (1995) 823–826. https://doi.org/10.1016/0022-3115(94)00623-7.

[100] Y. Nobuta, Y. Hatano, M. Matsuyama, S. Abe, S. Akamaru, Y. Yamauchi, T. Hino, S. Suzuki, M. Akiba, Tritium retention properties of tungsten, graphite and co-deposited carbon film, Fusion Engineering and Design. 89 (2014) 1516–1519. https://doi.org/10.1016/j.fusengdes.2014.04.004.

[101] T. Muroga, Vanadium for Nuclear Systems, in: Comprehensive Nuclear Materials, Elsevier, 2012: pp. 391–406. https://doi.org/10.1016/B978-0-08-056033-5.00094-X.

[102] Y. Katoh, L.L. Snead, T. Cheng, C. Shih, W.D. Lewis, T. Koyanagi, T. Hinoki, C.H. Henager, M. Ferraris, Radiation-tolerant joining technologies for silicon carbide ceramics and composites, Journal of Nuclear Materials. 448 (2014) 497–511. https://doi.org/10.1016/j.jnucmat.2013.10.002.

[103] J.M. Mistry, P.P. Gohil, Research review of diversified reinforcement on aluminum metal matrix composites: fabrication processes and mechanical characterization, Science and Engineering of Composite Materials. 25 (2018) 633–647. https://doi.org/10.1515/secm-2016-0278.

[104] S.P. Rawal, Metal-matrix composites for space applications, JOM. 53 (2001) 14–17. https://doi.org/10.1007/s11837-001-0139-z.

[105] D.B. Miracle, Metal matrix composites – From science to technological significance, Compos Sci Technol. 65 (2005) 2526–2540. https://doi.org/10.1016/j.compscitech.2005.05.027.

[106] W.H. Hunt, D.B. Miracle, Automotive Applications of Metal-Matrix Composites, in: Composites, ASM International, 2001: pp. 1029–1032. https://doi.org/10.31399/asm.hb.v21.a0003484.

[107] D.B. Miracle, Metal Matrix Composites for Space Systems: Current Uses and Future Opportunities, in: Affordable Metal-Matrix Composites for High Performance Applications II, John Wiley & Sons, Inc., Hoboken, NJ, USA, 2013: pp. 1–22. https://doi.org/10.1002/9781118787120.ch1.

[108] D.T. Hoelzer, History and Outlook of ODS/NFA Ferritic Alloys for Nuclear Applications, Trans Am Nucl Soc. 118 (2018).

[109] J.H. Lee, Development of oxide dispersion strengthened ferritic steels with and without aluminum, Frontiers in Energy. 6 (2012) 29–34. https://doi.org/10.1007/s11708-012-0178-x.

[110] N. Baluc, R. Schäublin, P. Spätig, M. Victoria, On the potentiality of using ferritic/martensitic steels as structural materials for fusion reactors, Nuclear Fusion. 44 (2004) 56–61. https://doi.org/10.1088/0029-5515/44/1/006.

[111] G.R. Odette, On the status and prospects for nanostructured ferritic alloys for nuclear fission and fusion application with emphasis on the underlying science, Scr Mater. 143 (2018) 142–148. https://doi.org/https://doi.org/10.1016/j.scriptamat.2017.06.021.

[112] S. Ukai, M. Fujiwara, Perspective of ODS alloys application in nuclear environments, Journal of Nuclear Materials. 307–311 (2002) 749–757. https://doi.org/10.1016/S0022-3115(02)01043-7.

[113] N. Yamamoto, Y. Murase, J. Nagakawa, An evaluation of helium embrittlement resistance of reduced activation martensitic steels, Fusion Engineering and Design. 81 (2006) 1085–1090.

[114] K.P. So, D. Chen, A. Kushima, M. Li, S. Kim, Y. Yang, Z. Wang, J.G. Park, Y.H. Lee, R.I. Gonzalez, M. Kiwi, E.M. Bringa, L. Shao, J. Li, Dispersion of carbon nanotubes in aluminum improves radiation resistance, Nano Energy. 22 (2016) 319–327. https://doi.org/10.1016/j.nanoen.2016.01.019.

[115] A. Ramanathan, P.K. Krishnan, R. Muraliraja, A review on the production of metal matrix composites through stir casting – Furnace design, properties, challenges, and

research opportunities, J Manuf Process. 42 (2019) 213–245. https://doi.org/10.1016/j.jmapro.2019.04.017.

[116] M.P. Behera, T. Dougherty, S. Singamneni, Conventional and Additive Manufacturing with Metal Matrix Composites: A Perspective, Procedia Manuf. 30 (2019) 159–166. https://doi.org/10.1016/j.promfg.2019.02.023.

[117] W.E. King, A.T. Anderson, R.M. Ferencz, N.E. Hodge, C. Kamath, S.A. Khairallah, A.M. Rubenchik, Laser powder bed fusion additive manufacturing of metals; physics, computational, and materials challenges, Appl Phys Rev. 2 (2015) 041304. https://doi.org/10.1063/1.4937809.

[118] D. Herzog, V. Seyda, E. Wycisk, C. Emmelmann, Additive manufacturing of metals, Acta Mater. 117 (2016) 371–392. https://doi.org/10.1016/j.actamat.2016.07.019.

[119] S. Shoemaker, First-ever 3D printed excavator project advances large-scale additive manufacturing R&D, Oak Ridge National Laboratory. (2016). https://www.ornl.gov/blog/first-ever-3d-printed-excavator-project-advances-large-scale-additive-manufacturing-rd.

[120] S. Liu, Y.C. Shin, Additive manufacturing of Ti6Al4V alloy: A review, Mater Des. 164 (2019) 107552. https://doi.org/10.1016/j.matdes.2018.107552.

[121] B. Graybill, M. Li, D. Malawey, C. Ma, J.-M. Alvarado-Orozco, E. Martinez-Franco, Additive Manufacturing of Nickel-Based Superalloys, in: Volume 1: Additive Manufacturing; Bio and Sustainable Manufacturing, American Society of Mechanical Engineers, 2018. https://doi.org/10.1115/MSEC2018-6666.

[122] D. Gu, H. Zhang, D. Dai, M. Xia, C. Hong, R. Poprawe, Laser additive manufacturing of nano-TiC reinforced Ni-based nanocomposites with tailored microstructure and performance, Compos B Eng. 163 (2019) 585–597. https://doi.org/10.1016/j.compositesb.2018.12.146.

[123] V. Mandal, P. Tripathi, A. Kumar, S.S. Singh, J. Ramkumar, A study on selective laser melting (SLM) of TiC and B4C reinforced IN718 metal matrix composites (MMCs), J Alloys Compd. 901 (2022) 163527. https://doi.org/10.1016/j.jallcom.2021.163527.

[124] X. Yao, S.K. Moon, B.Y. Lee, G. Bi, Effects of heat treatment on microstructures and tensile properties of IN718/TiC nanocomposite fabricated by selective laser melting, International Journal of Precision Engineering and Manufacturing. 18 (2017) 1693–1701. https://doi.org/10.1007/s12541-017-0197-y.

[125] Z. Zhang, Q. Han, S. Yang, Y. Yin, J. Gao, R. Setchi, Laser powder bed fusion of advanced submicrometer TiB2 reinforced high-performance Ni-based composite, Materials Science and Engineering: A. 817 (2021) 141416. https://doi.org/10.1016/j.msea.2021.141416.

[126] Z. Zhang, Q. Han, Z. Liu, X. Wang, L. Wang, X. Yang, T. Ma, Z. Gao, Influence of the TiB2 content on the processability, microstructure and high-temperature tensile performance of a Ni-based superalloy by laser powder bed fusion, J Alloys Compd. 908 (2022) 164656. https://doi.org/10.1016/j.jallcom.2022.164656.

[127] N. Read, W. Wang, K. Essa, M.M. Attallah, Selective laser melting of AlSi10Mg alloy: Process optimisation and mechanical properties development, Materials & Design (1980-2015). 65 (2015) 417–424. https://doi.org/10.1016/j.matdes.2014.09.044.

[128] G. Manohar, A. Dey, K.M. Pandey, S.R. Maity, Fabrication of metal matrix composites by powder metallurgy: A review, in: 2018: p. 020041. https://doi.org/10.1063/1.5032003.

[129] A.M.K. Esawi, K. Morsi, A. Sayed, M. Taher, S. Lanka, Effect of carbon nanotube (CNT) content on the mechanical properties of CNT-reinforced aluminium composites, Compos Sci Technol. 70 (2010) 2237–2241. https://doi.org/10.1016/j.compscitech.2010.05.004.

[130] B. Zhang, G. Bi, P. Wang, J. Bai, Y. Chew, M.S. Nai, Microstructure and mechanical properties of Inconel 625/nano-TiB2 composite fabricated by LAAM, Mater Des. 111 (2016) 70–79. https://doi.org/10.1016/j.matdes.2016.08.078.

[131] E. Hosseini, V.A. Popovich, A review of mechanical properties of additively manufactured Inconel 718, Addit Manuf. 30 (2019) 100877. https://doi.org/10.1016/j.addma.2019.100877.

[132] X. Wang, X. Gong, K. Chou, Review on powder-bed laser additive manufacturing of Inconel 718 parts, Proc Inst Mech Eng B J Eng Manuf. 231 (2017) 1890–1903. https://doi.org/10.1177/0954405415619883.

[133] C. Qiu, Y. Su, B. Chen, J. Yang, Z. Li, Q. Ouyang, Q. Guo, D. Xiong, D. Zhang, First-principles investigation of interfacial stability, mechanical behavior and failure mechanism of β-SiC(1 1 1)/Al(1 1 1) interfaces, Comput Mater Sci. 175 (2020) 109608. https://doi.org/10.1016/j.commatsci.2020.109608.

[134] M. Yamamoto, Y. Nishimura, M. Hayashida, Influence of Al particles as infiltration promoters on the interfacial reaction and mechanical property of a continuous SiC fiber/AZ91 composite fabricated by a low-pressure infiltration method, J Alloys Compd. 887 (2021) 161461. https://doi.org/10.1016/j.jallcom.2021.161461.

[135] E. Tekoğlu, A.D. O'Brien, J. Liu, B. Wang, S. Kavak, Y. Zhang, S.Y. Kim, S. Wang, D. Ağaoğulları, W. Chen, A.J. Hart, J. Li, Strengthening additively manufactured Inconel 718 through in-situ formation of nanocarbides and silicides, Addit Manuf. 67 (2023) 103478. https://doi.org/10.1016/j.addma.2023.103478.

[136] Q. Han, R. Setchi, S.L. Evans, Characterisation and milling time optimisation of nanocrystalline aluminium powder for selective laser melting, The International Journal of Advanced Manufacturing Technology. 88 (2017) 1429–1438. https://doi.org/10.1007/s00170-016-8866-z.

[137] Y. Gao, D. Zhang, M. Cao, R. Chen, Z. Feng, R. Poprawe, J.H. Schleifenbaum, S. Ziegler, Effect of δ phase on high temperature mechanical performances of Inconel 718 fabricated with SLM process, Materials Science and Engineering: A. 767 (2019) 138327. https://doi.org/10.1016/j.msea.2019.138327.

[138] S. Sui, H. Tan, J. Chen, C. Zhong, Z. Li, W. Fan, A. Gasser, W. Huang, The influence of Laves phases on the room temperature tensile properties of Inconel 718 fabricated by powder feeding laser additive manufacturing, Acta Mater. 164 (2019) 413–427. https://doi.org/10.1016/j.actamat.2018.10.032.

[139] C. Kantzos, J. Pauza, R. Cunningham, S.P. Narra, J. Beuth, A. Rollett, An Investigation of Process Parameter Modifications on Additively Manufactured Inconel 718 Parts, J Mater Eng Perform. 28 (2019) 620–626. https://doi.org/10.1007/s11665-018-3612-3.

[140] D. Zhang, W. Niu, X. Cao, Z. Liu, Effect of standard heat treatment on the microstructure and mechanical properties of selective laser melting manufactured Inconel 718 superalloy, Materials Science and Engineering: A. 644 (2015) 32–40. https://doi.org/10.1016/j.msea.2015.06.021.

[141] G.A. Rao, M. Kumar, M. Srinivas, D.S. Sarma, Effect of standard heat treatment on the microstructure and mechanical properties of hot isostatically pressed superalloy inconel 718, Materials Science and Engineering: A. 355 (2003) 114–125. https://doi.org/10.1016/S0921-5093(03)00079-0.

[142] K. Kulawik, P.A. Buffat, A. Kruk, A.M. Wusatowska-Sarnek, A. Czyrska-Filemonowicz, Imaging and characterization of γ′ and γ″ nanoparticles in Inconel 718 by EDX elemental mapping and FIB–SEM tomography, Mater Charact. 100 (2015) 74–80. https://doi.org/10.1016/j.matchar.2014.12.012.

[143] L.Y. Sheng, Y.X. Tian, J.T. Guo, Microstructural Characteristics and Mechanical Properties of a Nb/Nb $_5$ Si $_3$ based Composite with and without Directional Solidification, Advanced Composites Letters. 27 (2018) 096369351802700. https://doi.org/10.1177/096369351802700405.

[144] X.Y. Fang, H.Q. Li, M. Wang, C. Li, Y.B. Guo, Characterization of texture and grain boundary character distributions of selective laser melted Inconel 625 alloy, Mater Charact. 143 (2018) 182–190. https://doi.org/10.1016/j.matchar.2018.02.008.

[145] Z. Song, W. Gao, D. Wang, Z. Wu, M. Yan, L. Huang, X. Zhang, Very-High-Cycle Fatigue Behavior of Inconel 718 Alloy Fabricated by Selective Laser Melting at Elevated Temperature, Materials. 14 (2021) 1001. https://doi.org/10.3390/ma14041001.

[146] D. Gu, H. Zhang, D. Dai, M. Xia, C. Hong, R. Poprawe, Laser additive manufacturing of nano-TiC reinforced Ni-based nanocomposites with tailored microstructure and performance, Compos B Eng. 163 (2019) 585–597. https://doi.org/10.1016/j.compositesb.2018.12.146.

[147] A.S. Hakeem, F. Patel, N. Minhas, A. Malkawi, Z. Aleid, M.A. Ehsan, H. Sharrofna, A. Al Ghanim, Comparative evaluation of thermal and mechanical properties of nickel alloy 718 prepared using selective laser melting, spark plasma sintering, and

casting methods, Journal of Materials Research and Technology. 12 (2021) 870–881. https://doi.org/10.1016/j.jmrt.2021.03.043.

[148] M. Tanjilul, A. Ahmed, A.S. Kumar, M. Rahman, A study on EDM debris particle size and flushing mechanism for efficient debris removal in EDM-drilling of Inconel 718, J Mater Process Technol. 255 (2018) 263–274. https://doi.org/10.1016/j.jmatprotec.2017.12.016.

[149] E. Zapata-Solvas, S. Bonilla, P.R. Wilshaw, R.I. Todd, Preliminary investigation of flash sintering of SiC, J Eur Ceram Soc. 33 (2013) 2811–2816. https://doi.org/10.1016/j.jeurceramsoc.2013.04.023.

[150] A. Maity, D. Kalita, T.K. Kayal, T. Goswami, O. Chakrabarti, H.S. Maiti, P.G. Rao, Synthesis of SiC ceramics from processed cellulosic bio-precursor, Ceram Int. 36 (2010) 323–331. https://doi.org/10.1016/j.ceramint.2009.09.006.

[151] D.E. Cooper, N. Blundell, S. Maggs, G.J. Gibbons, Additive layer manufacture of Inconel 625 metal matrix composites, reinforcement material evaluation, J Mater Process Technol. 213 (2013) 2191–2200. https://doi.org/10.1016/j.jmatprotec.2013.06.021.

[152] Q. Song, Y. Zhang, Y. Wei, X. Zhou, Y. Shen, Y. Zhou, X. Feng, Microstructure and mechanical performance of ODS superalloys manufactured by selective laser melting, Opt Laser Technol. 144 (2021) 107423. https://doi.org/10.1016/j.optlastec.2021.107423.

[153] N/A, Atlas of Stress-Strain Curves (2nd Edition), (n.d.). https://app.knovel.com/hotlink/toc/id:kpASSCE002/atlas-stress-strain-curves/atlas-stress-strain-curves.

[154] A.K. Sahu, S. Bag, Design of a double aging treatment for the improvement of mechanical and microstructural properties of pulse micro-plasma arc welded alloy 718, J Mater Sci. 56 (2021) 13400–13415. https://doi.org/10.1007/s10853-021-06121-8.

[155] W.G. Fahrenholtz, G.E. Hilmas, Ultra-high temperature ceramics: Materials for extreme environments, Scr Mater. 129 (2017) 94–99. https://doi.org/10.1016/j.scriptamat.2016.10.018.

[156] E. Wuchina, E. Opila, W. Fahrenholtz, I. Talmy, UHTCs: Ultra-High Temperature Ceramic Materials for Extreme Environment Applications, Electrochem Soc Interface. (2007) 30–36.

[157] W.G. Fahrenholtz, G.E. Hilmas, Oxidation of ultra-high temperature transition metal diboride ceramics, International Materials Reviews. 57 (2012) 61–72. https://doi.org/10.1179/1743280411Y.0000000012.

[158] E.W. Neuman, G.E. Hilmas, W.G. Fahrenholtz, Elevated Temperature Strength Enhancement of ZrB 2 –30 vol% SiC Ceramics by Postsintering Thermal Annealing, Journal of the American Ceramic Society. 99 (2016) 962–970. https://doi.org/10.1111/jace.14029.

[159] J. Du, B. Wen, R. Melnik, Y. Kawazoe, First-principles studies on structural, mechanical, thermodynamic and electronic properties of Ni–Zr intermetallic compounds, Intermetallics (Barking). 54 (2014) 110–119. https://doi.org/10.1016/j.intermet.2014.05.021.

[160] S. Sui, H. Tan, J. Chen, C. Zhong, Z. Li, W. Fan, A. Gasser, W. Huang, The influence of Laves phases on the room temperature tensile properties of Inconel 718 fabricated by powder feeding laser additive manufacturing, Acta Mater. 164 (2019) 413–427. https://doi.org/10.1016/j.actamat.2018.10.032.

[161] V. Prithivirajan, M.D. Sangid, The role of defects and critical pore size analysis in the fatigue response of additively manufactured IN718 via crystal plasticity, Mater Des. 150 (2018) 139–153. https://doi.org/10.1016/j.matdes.2018.04.022.

[162] M. Qu, Q. Guo, L.I. Escano, A. Nabaa, S.M.H. Hojjatzadeh, Z.A. Young, L. Chen, Controlling process instability for defect lean metal additive manufacturing, Nat Commun. 13 (2022) 1079. https://doi.org/10.1038/s41467-022-28649-2.

[163] Y. Zheng, F. Liu, W. Zhang, F. Liu, C. Huang, J. Gao, Q. Li, The microstructure evolution and precipitation behavior of TiB2/Inconel 718 composites manufactured by selective laser melting, J Manuf Process. 79 (2022) 510–519. https://doi.org/10.1016/j.jmapro.2022.04.070.

[164] L. Xiao, D. Chen, M.C. Chaturvedi, Effect of Boron and Carbon on the Fracture Toughness of IN 718 Superalloy at Room Temperature and 650 °C, J Mater Eng Perform. 14 (2005) 528–538. https://doi.org/10.1361/105994905X56106.

[165] J.W. Hutchinson, K.W. Neale, Influence of strain-rate sensitivity on necking under uniaxial tension, Acta Metallurgica. 25 (1977) 839–846.

[166] Y. Wang, J. Li, A. V. Hamza, T.W. Barbee, Ductile crystalline–amorphous nanolaminates, Proceedings of the National Academy of Sciences. 104 (2007) 11155–11160. https://doi.org/10.1073/pnas.0702344104.

[167] M. Liu, J. Zhang, C. Chen, Z. Geng, Y. Wu, D. Li, T. Zhang, Y. Guo, Additive manufacturing of pure niobium by laser powder bed fusion: Microstructure, mechanical behavior and oxygen assisted embrittlement, Materials Science and Engineering: A. 866 (2023) 144691. https://doi.org/10.1016/j.msea.2023.144691.

[168] T. Griemsmann, A. Abel, C. Hoff, J. Hermsdorf, M. Weinmann, S. Kaierle, Laser-based powder bed fusion of niobium with different build-up rates, The International Journal of Advanced Manufacturing Technology. 114 (2021) 305–317. https://doi.org/10.1007/s00170-021-06645-y.

[169] U. Scipioni Bertoli, A.J. Wolfer, M.J. Matthews, J.-P.R. Delplanque, J.M. Schoenung, On the limitations of Volumetric Energy Density as a design parameter for Selective Laser Melting, Mater Des. 113 (2017) 331–340. https://doi.org/10.1016/j.matdes.2016.10.037.

[170] H. Ghasemi-Tabasi, J. Jhabvala, E. Boillat, T. Ivas, R. Drissi-Daoudi, R.E. Logé, An effective rule for translating optimal selective laser melting processing parameters from one material to another, Addit Manuf. 36 (2020) 101496. https://doi.org/10.1016/j.addma.2020.101496.

[171] J. Trapp, A.M. Rubenchik, G. Guss, M.J. Matthews, In situ absorptivity measurements of metallic powders during laser powder-bed fusion additive manufacturing, Appl Mater Today. 9 (2017) 341–349. https://doi.org/10.1016/j.apmt.2017.08.006.